Mechanical Engineering Advances

https://ojs.acad-pub.com/index.php/mea

2025 VOLUME 3 ISSUE 1
ISSN: 3029-1232 (Online)

1

Editorial Board

Editor-in-Chief

Associate Editor

Editorial Board Members

Volume 3 Issue 1 • 2025

Mechanical Engineering Advances

ACADEMIC
ACADEMIC PUBLISHING PTE LTD

2025 | Volume 3 | Issue 1

Mechanical Engineering Advances

https://ojs.acad-pub.com/index.php/MEA

Contents

Articles

Review

Perspective

Mechanical Engineering Advances 2025, 3(1), 1405.
https://doi.org/10.59400/mea1405

Article

Finite element structural analysis of simply supported solid and stiffened plates: A comparative study

K. Shabla[1,*], Chitaranjan Pany[2]

[1] Department of Civil Engineering, NSS College of Engineering Palakkad, Kerala 678008, India
[2] STR, VSSC, Trivandrum, Kerala 695022, India
*** Corresponding author:** K. Shabla, shabla1999@gmail.com

CITATION

Shabla K, Pany C. Finite element structural analysis of simply supported solid and stiffened plates: A comparative study. Mechanical Engineering Advances. 2025; 3(1): 1405.
https://doi.org/10.59400/mea1405

ARTICLE INFO

Received: 28 May 2024
Accepted: 4 November 2024
Available online: 27 November 2024

Abstract: A structure's form and shape influence how it behaves when loaded. This was achieved by contrasting the stiffened plate's performance with that of a solid plate made of the same material and volume. The results have demonstrated that bending stress in stiffened plates is decreased when a solid plate of the same material and volume is transformed into a stiffened plate. Because stiffened plates have a higher strength to weight ratio than solid plates, this supports the recommendation of stiffened plates for a variety of technical applications. In order to determine the impact of stiffener orientation on bending stress reduction in stiffened plates, additional investigations were carried out on a number of plates. An investigation was carried out to determine the ideal stiffener angle in a stiffened plate that could offer the least amount of stress. The current work offers insightful information about particular stiffened plate design characteristics that can be used in a variety of engineering contexts.

Keywords: stiffened plate; solid plate; stiffeners; orientation; finite element method

1. Introduction

In the fields of naval, aircraft, buildings, bridges, and vehicle transportation engineering, key structural elements like beams, plates, and their interconnected forms are widely analyzed. Various studies have applied different methodologies to explore the behavior of these elements. Langley et al. [1] utilized Statistical Energy Analysis (SEA) to investigate how periodically stiffened plates transmit vibration energy, specifically focusing on how the distance between stiffeners affects this energy transmission. Similarly, Bercin [2] employed both the direct-dynamic stiffness approach and SEA to study the flexural energy transfer in stiffened plates, considering factors like rotational inertia and shear distortion. Lin et al. [3] also applied the SEA method to analyze L-shaped plates with simply supported boundaries, estimating energy flow under specific force and moment excitations.

Research on stiffened plates has also been explored through static loading scenarios. For instance, Ghavami [4] conducted experimental studies to evaluate how longitudinal stiffener cross-sections and spacing influence buckling behavior and the maximum collapse load in stiffened steel plates under uniform axial loads. Here, test results were compared with different design codes which provided valuable insights into improving the accuracy of structural behavior predictions. Similarly, Hu and Jiang [5] performed full-scale tests and finite element simulations to examine the plastic post-buckling behavior of stiffened panels, enhancing our understanding of load-carrying capacity under practical loading conditions.

Dynamic approaches have been applied extensively in stiffened plate research, especially in terms of vibration and impact response. Pany et al. [6–9] leveraged the finite element (FE) method to explore wave propagation and vibration characteristics of line-supported plate and shell structures. In another dynamic analysis, Park et al. [10] applied the Flexural Stiffness Index (FSI) to optimize the design of corrugated core panels for durability under impact forces. Ke et al. [11] focused on the impact resistance of corrugated core sandwich panels within ship structures, analyzing mechanical properties under both static and dynamic loading conditions. The analyses of stiffened plates by finite element method were reported by [12–15]. Buckling analysis of these plates has been explored through both conventional and super finite element approaches, employing Mindlin plate theory and Timoshenko beam theory for modeling in [16]. Finite strip methods were also reported by [17–20]. The bending response of isotropic rectangular plates subjected to diverse loading scenarios is analyzed using MATLAB and the commercial FEM software ANSYS, incorporating Classical Plate Theory and plane stress assumptions in [21]. Additionally, [22] examines the performance of stiffened plates composed of different materials, including steel, unidirectional composite material in single-ply form, and laminated composites with five plies, highlighting the versatility of these structures in various applications.

Post-tensioned concrete bridge [23], tall RCC buildings [24], beam-column connections [25], bamboo-reinforced composite concrete [26] are just a few structural examples where beams and stiffened plate are important in design. Several studies have turned to FEA and mathematical modeling to explore complex behaviors in stiffened plates. Tanaka and Endo [27] proposed a method that combined elastic large deformation analysis with rigid-plastic analysis to assess local buckling and collapse behavior in stiffened plates with flat bar stiffeners. This method has been validated through experimental comparisons, highlighting its effectiveness in estimating ultimate loads and post-buckling behavior. Ghavami and Khedmati [28] used FEA to simulate non-linear behaviors under axial compression, revealing strong correlations with experimental results and offering predictive capabilities for flexural and local buckling phenomena. Nguyen et al. [29] have focused on refining theories for evaluating static behaviors in functionally graded plates, while others have looked at the role of stiffener angles in enhancing the load-bearing capacity of stiffened plates.

The present study aims in exploring the effect of shape and form of a structure in its behavior under loads. Research has shown that converting a solid plate into a stiffened plate of the same material and volume can significantly reduce bending stress. By carefully examining interactions between flanges and stiffeners, optimal designs can be identified to minimize stress and improve structural performance.In order to determine the effect of stiffener orientation/angles on structural performance (i.e., bending stress) in stiffened plates, additional investigations were carried out on a number of plates.

2. Analysis of stiffened plate

A stiffened plate is a plate that has stiffeners inserted between the flanges as shown in **Figure 1**. A 500 × 50 × 5000 mm steel [30] stiffened plate is analyzed under

uniform pressure of 0.01 N/mm^2. It is provided in a simply supported condition with hinge support at one end and roller support at the other end. The stiffeners have a thickness of 1 mm.

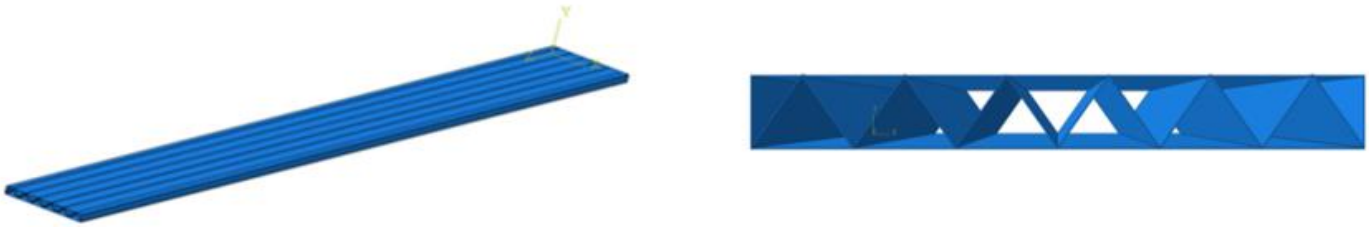

Figure 1. Stiffened plate.

2.1. Numerical simulation of stiffened plate in abaqus [12]

Abaqus software is used to model and simulate a stiffened plate, as illustrated in **Figure 2**, in order to investigate how a plate's form and shape impact its structural performance. **Figure 3** illustrates the cross section.

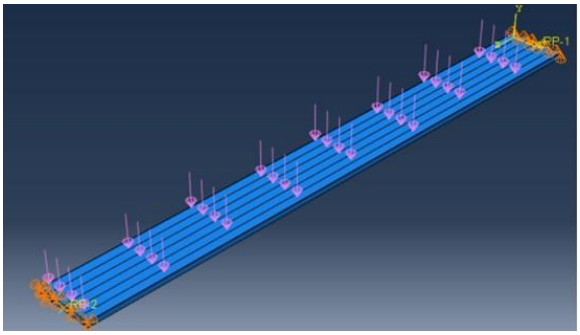

Figure 2. Stiffened plate modelled in Abaqus.

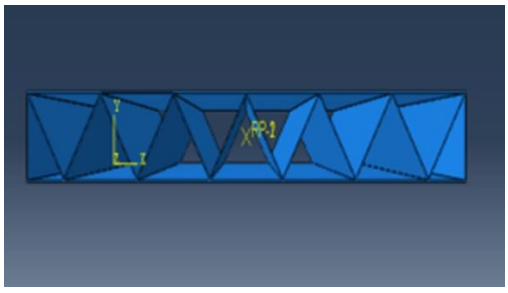

Figure 3. Cross section of the stiffened plate.

Figure 4 shows the bending stress results that were derived from Abaqus. The determined bending stress is 189.4 N/mm^2. It is evident from the research that the plate's flanges bear the majority of the bending load.

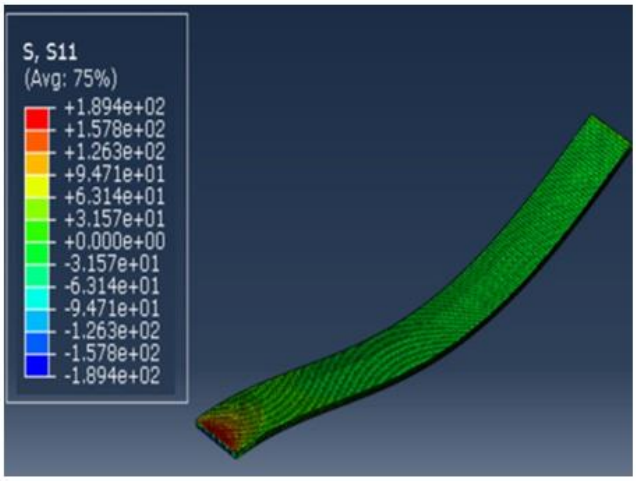

Figure 4. Bending stress of stiffened plate.

2.2. Analytical solution [31]

The accuracy of the findings obtained by the Abaqus program is verified by analytical solutions to the problems.

Span of the plate, L = 5000 mm Width of the plate, b = 500 mm

Depth of the plate, d = 50 mm

Load, $W = 0.01 \text{N/mm}^2 = 0.01 \times 5000 = 5 \text{ N/mm}$

Modulus of elasticity, $E = 2 \times 10^5 \text{ N/mm}^2$

Moment of inertia, $I = \frac{500\ x\ 50^3}{12} - \frac{24\ x\ 44.14\ x\ 47^3}{36} = 2153168.52 \text{ mm}^4$

Bending stress is evaluated from bending equation,

$$\frac{M}{I} = \frac{f}{y} = \frac{E}{R}$$

Maximum moment, M is obtained as 15625000Nmm and bending stress, f is found out as 181 N/mm^2

2.3. Comparison of abaqus FE results with analytical solutions

Using an analytical solution, the results of the examination of stiffened plates performed with Abaqus software are compared, and the percentage error is computed. **Table 1** tabulates the % error computation. The model is validated when the computed percentage error is less than 5%.

Table 1. Comparison of results for stiffened plates.

Structural parameter	Abaqus	Analytical	Percentage Error (%)
Bending stress (N/mm^2)	189.4	181	4.64

3. Analysis of solid plate

Under the same loading circumstances, the analysis is performed in a solid plate with the same volume and material as the stiffened plate and an equivalent depth. This provides information on how a structure's form influences its ability to withstand load and deformation.

By equating the volume of stiffened plate with the comparable volume of solid plate, one can determine the equivalent depth of solid plate.

Volume of the stiffened plate is obtained as 0.009242 m^3.

Volume of solid plate = 5000 × 500 ×t

where t is the depth of solid plate

5000 × 500 ×t = 0.009242

By solving the equation, equivalent depth of solid plate = 3.7 mm

3.1. Numerical simulation of solid plate

Using Abaqus software, a 500 × 3.7 × 5000 solid plate is modeled and examined to determine the maximum bending stress. **Figure 5** depicts a solid plate that has been modelled in Abaqus. **Figure 6** depicts the bending stress results that were obtained.

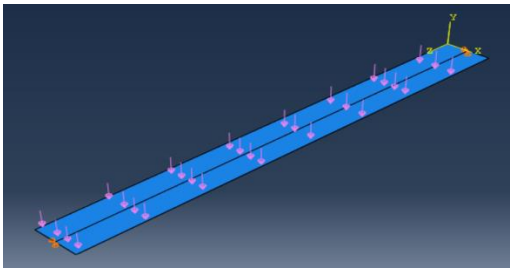

Figure 5. Finite element model of solid plate.

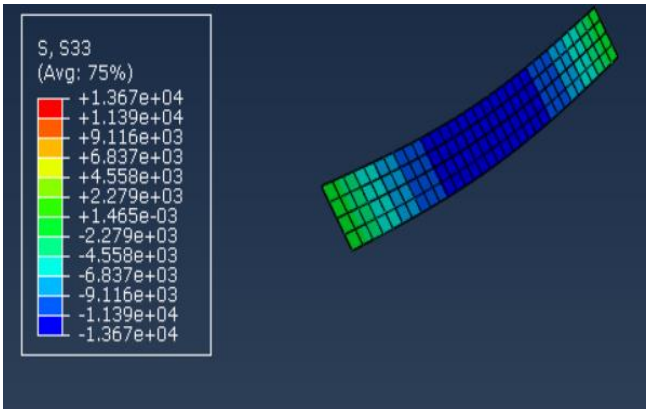

Figure 6. Bending stress (MPa) of solid plate.

3.2. Analytical solution

Maximum moment and bending stress is found out using analytical equations and are obtained as 15625000 Nmm and 0.137 × 10^5 N/mm^2 respectively.

3.3. Comparison of abaqus FE results with analytical solutions

Using analytical solution, the results of the solid plate analysis performed with Abaqus software arecompared, and the percentage error is computed. **Table 2** tabulates the % error computation. The model is validated when the computed percentage error is less than 5%.

Table 2. Comparison of results for solid plates.

Structural parameter	Abaqus	Analytical	Percentage Error (%)
Bending stress (N/mm^2)	0.136×10^5	0.137×10^5	0.73

3.4. Comparison of results for stiffened plate and solid plate

The comparison of results obtained for bending stress (MPa) in the stiffened plate and solid plate is tabulated in **Table 3**.

Table 3. Comparison of results for stiffened plate and solid plate.

Structural parameter	Stiffened Plate	Solid Plate
Bending stress (N/mm^2)	189.4	0.136×10^5

Ratio of bending stress of solid plate and stiffened plate is 71.8. So, there is a 71.8 reduction in bending stress when a solid plate is converted into a stiffened plate with the same material and volume. This is because stiffeners lessen the stress under load through distribution of load across the structure and stiffened plates have a higher strength to weight ratio than solid plates. This inference supports the recommendation of stiffened plates for a variety of technical applications.

4. Effect of angle of stiffeners on structural performance

In order to determine how the stiffeners' angle affects the stiffened plate's performance, the study varies the stiffeners' angle. The study also attempts to determine the ideal stiffener angle that yields the best results under loading circumstances. Analysis of stiffened plates is done with the stiffeners angled at 30, 40, 50, and 60 degrees. It is noteworthy that the study does not include plates with stiffeners positioned at an angle greater than 60° because failure occurs when stiffeners are oriented beyond an angle of 60°.

Variation of bending stress of stiffened plate with angle of stiffeners

The bending stress of a stiffened plate is analyzed as the stiffeners' angles are changed. **Figure 7** displays the bending stress values of a stiffened plate with stiffeners positioned at 30°, 40°, 50°, and 60°. The bending stress variation with stiffener angle is depicted in **Figure 8**. According to the results, bending stress shows a decreasing trend until it reaches an optimal value, after which it begins to grow. However, the graph does not include the value of 60° because, in this case, the plate's bending stress is greater than its strength (23570 N/mm^2)

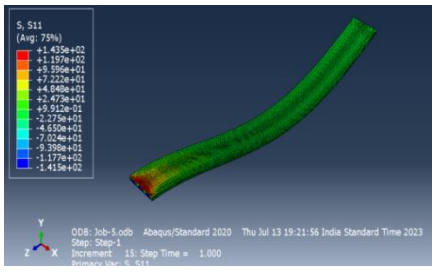

(a)

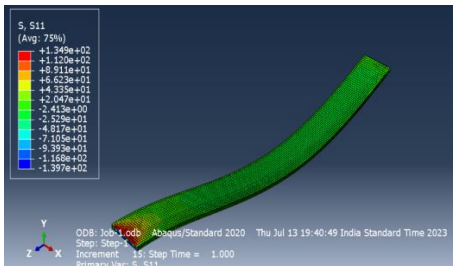

(b)

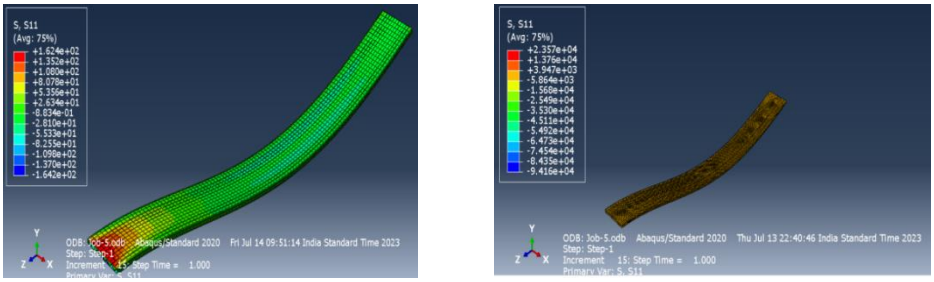

(c) **(d)**

Figure 7. Bending stress of stiffened plate with stiffeners at various angles **(a)**30° ;**(b)** 40°**;(c)** 50°; **(d)** 60°.

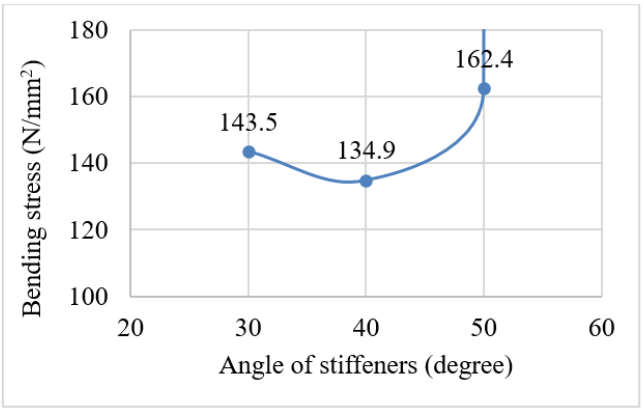

Figure 8. Variation of bending stress with angle of stiffeners.

5. Optimal angle of stiffeners in stiffened plate

The FE analysis of stiffened plate with angle of stiffeners oriented at 30°, 40°, 50°and 60° are performed and results are reported. To conduct a comprehensive analysis which enable a better assessment of optimal angle of stiffeners, further analysis is done on stiffened plate with angle of stiffeners between 40^0 and 50^0, incremented by 2°,until an upward trend in bending stress is observed. Two trails conducted at 42° and 44° and results for bending stress of stiffened plate with angle of stiffeners at 42° and 44°are shown in **Figure 9a,b** respectively. At a stiffener angle of 42°, the plate undergoes a bending stress of 134.5 N/mm^2, which increases to 149.1 N/mm^2 when the angle of stiffener is increased to 44°.

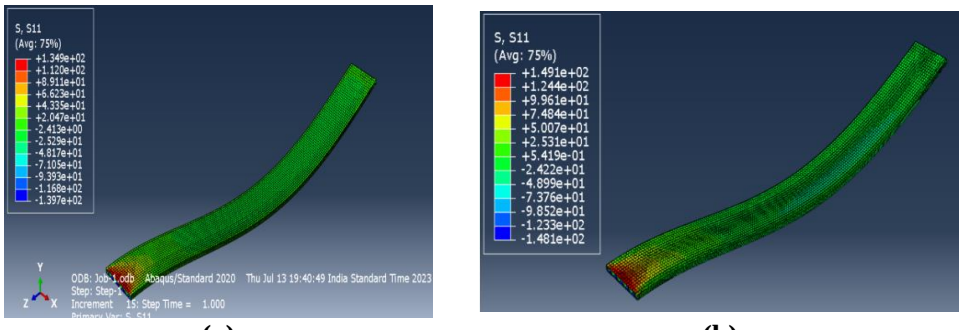

(a) **(b)**

Figure 9. Bending stress of stiffened plate with stiffeners at an angle of **(a)** 42°; **(b)** 44°.

Figure 10 shows the variation of stress of stiffened plate with angle of stiffeners. Notably, the graph excludes the case of stiffened plate with stiffeners oriented at 60° as the plate fails under this condition. The graph reveals that the plate demonstrates the lowest values of stress at an angle of 42°. Therefore, it can be concluded that the optimal angle of stiffeners, which offers improved performance under load is 42°.

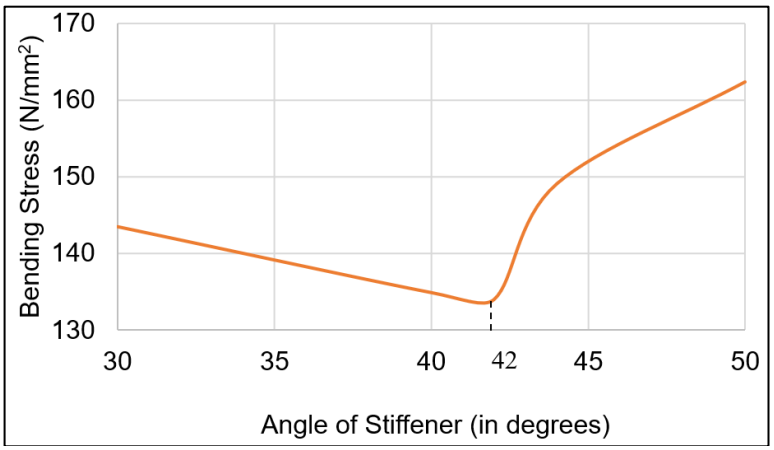

Figure 10. Graph between angle of stiffeners and bending stress.

6. Conclusions

In conclusion, this study signifies the consideration of form and shape in the design of a structure alongside its material properties in order to improve its structural performance. The key findings from the study can be summarized as follows:

1) The form and shape of a structure plays an important role in its ability to withstand external loads.
2) The transformation of a solid plate into a stiffened plate of identical material and volume results in reduction of bending stress (by a factor of 71.8) through improvement in load distribution. This strengthens the recommendation of stiffened plates for various engineering applications as the strength to weight ratio of stiffened plate is more than that of a solid plate.
3) The angle of stiffeners in a stiffened plate can be varied between 30° and 50°, with 42° being identified as the optimum value which can exhibit minimum stress in the plate through effective load distribution.

The work provides valuable insights into specific design parameters for stiffened plates, which can be applied in various engineering applications. Further studies can be conducted to delve deeper into enhancing the performance of stiffened plates by varying other design parameters, such as the depth of the sheet. Additionally, in the present work linear finite element (FE) analysis is performed. More realistic nonlinear FE analysis will give better design results of stiffened plates.

Author contributions: Conceptualization, KS and CP; methodology, KS and CP; software, KS; validation, KS; formal analysis, KS; investigation, KS; resources, KS; data curation, KS; writing—original draft preparation, KS; writing—review and editing, CP; visualization, KS; supervision, CP; project administration, KS and CP. All authors have read and agreed to the published version of the manuscript.

Conflict of interest: The authors declare no conflict of interest.

References

1. Langley RS, Smith JRD, Fahy FJ. Statistical energy analysis of periodically stiffened damped plate structures. Journal of Sound and Vibration. 1997; 208(3):407–426. doi: 10.1006/ jsvi.1997.1150
2. Bercin AN. Analysis of energy flow in thick plate structures. Computers and Structures. 1997; 62(4): 747–756.doi: 10.1016/S0045-7949(96)00235-0
3. Lin TR, Tan ACC, Yan C, Hargreaves D. Vibration response of an L-shaped plate under a deterministic force or moment excitation: a case of statistical energy analysis application.Journal of Sound and Vibration. 2011; 330(20):4780–4797.doi: 10.1016/j.jsv.2011.04.015
4. Ghavami K. Experimental study of stiffened plates in compression up to collapse. Journal of Constructional Steel Research. 1994; 28(2):197–222.
5. Hu SZ, Jiang L. A finite element simulation of the test procedure of stiffened plates. Journal of Marine Structures. 1998; 1:75–99.
6. Pany C, Parthan S, Mukherjee S. Vibration analysis of multi-supported curved panel using the periodic structure approach. International journal of mechanical sciences. 2002; 44(2):269–285.doi: 10.1016/S0020-7403(01)00099-6
7. Pany C, Parthan S. Axial wave propagation in infinitely long periodic curved panels. Journal of Vibration and Acoustics 2003; 125(1):24–30. doi: 10.1115/1.1526510
8. Pany C. An insight on the estimation of wave propagation constants in an orthogonal grid of a simple line-supported periodic plate using a finite element mathematical model. Frontiers in Mechanical Engineering. 2022; 8: 926559. doi: 10.3389/fmech.2022.926559
9. Pany C, Parthan S, Mukhopadhyay M. Free vibration analysis of an orthogonally supported multi-span curved panel. Journal of sound and vibration. 2001; 241(2):315–318.doi: 10.1006/jsvi.2000.3240
10. Park J, Kim G, Kwon S, et al. Finite Element Analysis of Corrugated Board Under Bending Stress. Journal of the Faculty of Agriculture Kyushu University. 2012; 57(1):181–188.
11. Ke L, Liu K, Wu G, et al. Multi-Objective Optimization Design of Corrugated Steel Sandwich Panel for Impact Resistance. Metals (Basel). 2021; 11(9):1378.
12. Singh D, Duggal S, Pal P. Analysis of stiffened plates using FEM–a parametric study. International Research Journal of Engineering and Technology. 2015. 2. 165-1656.
13. Fujikubo M, Kaeding P. New simplified approach to collapse analysis of stiffened plates. Marine Structures. 2002.15(3). 251-283.
14. Sheikh IA, Grondin GY, Elwi AE. Stiffened steel plates under uniaxial compression. Journal of Constructional Steel Research. 2002. 58(5-8). 1061-1080.
15. Grondin GY, Elwi AE, Cheng JJR. Buckling of stiffened steel plate - a parametric study. Journal of Constructional Steel Research. 1999. 50(2). 151-175.
16. Jafarpour HS, Ahmad RR. Buckling analysis of stiffened plates subjected to non-uniform biaxial compressive loads using conventional and super finite elements. Thin-Walled Structures. 2013.
17. Riks E. Buckling and post-buckling analysis of stiffened panels in wing box structures. International Journal of Solids and Structures. 2000. 37(46- 47). 6795-6824.
18. Xie W -C. Buckling model localization in rib-stiffened plates with randomly misplaced stiffeners. Computers and Structures.1998. 67(1-3).175-189.
19. Xie W-C, Ibrahim A. Buckling mode localization in rib-stiffened plates with misplaced stiffeners - a finite strip approach. Chaos, Solitons and Fractals. 2000. 11(10). 1543-1558.
20. Xie W-C. Elishakoff I. Buckling mode localization in rib-stiffened plates with misplaced stiffeners - kantorovich approach. Chaos, Solitons and Fractals. 2000. 11 (10). 1559-1574.
21. Bashir B, Amin P, Amir A. Analysis of Deflection of Rectangular Plates under Different Loading Conditions. International Journal of Natural and Engineering Science. 2012.
22. Sreedhar HK, Harsha VD. Structural Analysis of Stiffened Plates with Different Materials. International Journal of Research Publication and Reviews. 2023. 4(7). 2110-2114.

23. Lee WK, Billington SL. Performance-based earthquake engineering assessment of a self centering, post-tensioned concrete bridge system. Earthquake Engineering & Structural Dynamics. 2011; 40: 887-902.doi: 10.1002/eqe.1065
24. Sreadha AR, Pany C. Seismic Study of Multistorey Building using Floating Column. International Journal of Emerging Science and Engineering. 2020; 6(9):6-11.
25. Sreadha AR, Pany C, Varkey MV. A Review on Seismic Retrofit of Beam-Column Joints. International Journal for Modern Trends in Science and Technology. 2020; 6(9): 80-93.
26. Sreadha AR, Pany C. Review on fabrication of bamboo composite materials reinforced concrete. Journal of Science and Technology. 2020; 05(03):258-279.
27. Tanaka Y, Endo H. Ultimate strength of stiffened plates with their stiffeners locally buckled in compression. Journal of the Society of Naval Architects of Japan. 1988; 1998(164):456-467. doi: 10.2534/jjasnaoe1968.1988.164_456
28. Ghavami K, Khedmati MR. Numerical and experimental investigations on the compression behavior of stiffened plates. Journal of Constructional Steel Research. 2006; 62(11):1087-1100.
29. Nguyen VL, Tran MT, Nguyen VL, Le QH. Static behavior of functionally graded plates resting on elastic foundations using neutral surface concept. Archive of Mechanical Engineering. 2021; 68(1): 5–22.doi: 10.24425/ame.2020.131706
30. Bureau of Indian Standards. General Construction in Steelcode of practice. Bureau of Indian Standards; 2007.
31. Timoshenko, W-K. Theory of plates and shells. McGraw–Hill New York; 1959.

Mechanical Engineering Advances 2025, 3(1), 1921.
https://doi.org/10.59400/mea1921

Article

A novel approach for wear assessment of plastic gears using image processing

Mahmoud G. Elkasrawi[1], Marah A. Elsiedy[2], Hesham A. Hegazi[3,4,*]

[1] Department of Mechatronics, Faculty of Engineering and Materials Science, German University in Cairo, Cairo 11835, Egypt
[2] Department of Production Engineering and Mechanical Design, Faculty of Engineering, Tanta University, Tanta 31527, Egypt
[3] Mechanical Design and Production Engineering Department, Faculty of Engineering, Cairo University, Giza 12613, Egypt
[4] Design and Production Engineering Department, Faculty of Engineering and Materials Science, German University in Cairo, Cairo 11835, Egypt
*** Corresponding author:** Hesham A. Hegazi, hesham.hegazi@guc.edu.eg

CITATION

Elkasrawi MG, Elsiedy MA, Hegazi HA. A novel approach for wear assessment of plastic gears using image processing. Mechanical Engineering Advances. 2025; 3(1): 1921.
https://doi.org/10.59400/mea1921

ARTICLE INFO

Received: 23 October 2024
Accepted: 28 November 2024
Available online: 5 December 2024

Abstract: Plastic gears offer numerous advantages, poised to increasingly supplant metal gears across various applications. Notably, they boast silent operation, resistance to corrosion, and lightweight properties which make them ideal for wind turbine systems. Moreover, the expanding array of plastic materials, including eco-plastics and their natural fibre composites, underscores the imperative for ongoing research into plastic gears and their composites. Addressing existing challenges is pivotal to fully harnessing their potential in sustainable development efforts. The wear of plastic gears is an important factor in plastic gear design and optimization. This paper primarily examines wear assessment in polypropylene (PP) gears by proposing and implementing a novel approach to measure the amount of wear on gear tooth profile using an image processing technique. By subjecting plastic gears to wear experimentation and employing direct image processing methods, the percentage of damage can be accurately evaluated. These percentages were 0.2% and 2.5% for 2 and 5 hours respectively. This underscores the boundless possibilities of integrating image processing techniques into the assessment of plastic gears, paving the way for deeper exploration and optimization of polymer materials for plastic gear manufacturing.

Keywords: plastic gears; wear assessment; image processing; testing of plastic gears; gears performance

1. Introduction

Polymer gears create a surge in the world of industry through various advantages such as lightweight, low manufacturing cost, inherent lubrication, and functioning without noise [1,2]. Introducing these traits, plastic gears excel in their equivalents; metallic gears in renewable energy systems such as wind turbine systems, solar panel tracking systems, marine renewable energy devices, and hydroelectric power plants [3]. A reduction of 9% in fuel consumption, 80% in inertia, and 70% in mass could be achieved when using plastic gears [4,5].

The failure modes of plastic gears are entirely different from metallic ones. For example, higher temperatures (reaching a melting temperature of 175 °C in polyoxymethylene for example) during operation due to higher operational load and speed could lead to deterioration of the mechanical properties of polymer gears [6]. For this reason, a study such as the one conducted by Singh et al. [7], considered determining a transition torque from the equation of surface temperature at which the wear is extremely high. Following the same way, Mao et al. [8] experimented with the

glass fiber reinforced polyacetal (POM) and neat POM to assess the type of failure mode which depends on the transition torque evaluated from surface temperature. In studies conducted by Elsiedy et al. [9,10], wear was added to the optimization problem as a type of design constraint to obtain the optimum design of polymer spur gears in terms of several teeth, modules, face width, and profile coefficients. Wear of the polymer gears was contained in several formations such as cracks, debris formation, breakage, and thermal damage as suggested by Ghazali et al. [11].

A plethora of studies in the literature have been conducted to investigate the wear of polymer gears. In the study of Tunalioglu and Torun [12], a 3D printed spur pinion made of polylactic acid (PLA) material meshed with steel gear was examined experimentally at different loads and speeds to determine the amount of wear using the coordinate measuring machine. It was shown that wear was significant at the root region because of the increased temperature due to the opposite direction of rolling and sliding of the engaging teeth. The results also demonstrated that the wear resistance of the material could be increased by the increase of strain rate and decrease of single tooth contact time. PLA pinion along with two other pinions made from polyethylene terephthalate (PETG) and Acrylonitrile Butadiene styrene (ABS) were meshed with steel gear in the study of Tunalioglu and Agca [13]. The aim was to compare the wear of the three materials by applying a theoretical wear equation. It was found that PETG gears exhibited the least wear at the same number of cycles. The wear and fatigue life of spur gears made of two different materials such as polyamide with 20% carbon fiber (machine cut) and carbon fiber reinforced polyamide (additive manufactured) were assessed in the study of Hribersek et al. [14]. The study revealed that at lower loads, machine-cut polyamide gears are expected to have cracks near the pitch point. On the other hand, in additively manufactured polyamide gears, cracks occurred at the root area. It was concluded that load levels have a significant effect on the wear rate and the surface temperature of gears. The wear coefficient was determined in the study of Muratovic et al. [15] analytically according to Verein Deutscher Ingenieure (VDI) standard and experimentally. The experiment was done by meshing steel pinion with polymer gear on a wear test rig. The average linear wear resulting from the experiment is used to calculate the wear coefficient which in turn is used in an iterative process to assess the wear depth during the progressive cycles. Hlebanja et al. [16] investigated two types of gear profiles (S and E- involute profiles). It was found that S gears behaved better than E gears as the former gave lower contact pressure, and less sliding contact, thus less frictional losses, temperature and wear. Increasing the width of the single tooth contact region of the polymer gear will reduce the load and temperature which are the main reasons for higher wear rates at this region as suggested by Imrek [17]. Other studies conducted by Mao and coworkers considered determining the wear rate of different polymer materials either composites or neat [1,18–23]. Wear of a neat material such as acetal is affected by the load. This conclusion was elucidated by Breeds et al. [24], Kukureka et al. [25], and Li et al. [26]. Reaching a higher load (critical value of 9.5 Nm) leads to a higher surface temperature, and melts the teeth and this in turn causes thermal bending. When adding glass fibre reinforcements to acetal material, the load capacity increases by approximately 50%, thus the gear will take time to wear till the end of the specified number of cycles. Three materials were introduced in the study of Singh et al. [7]; Acrylonitrile Butadiene

styrene (ABS), High-density polyethylene (HDPE), and poly acetal (POM). When experimenting with gears made of these materials for calculating the amount of wear at different torques and speeds, POM exhibited lower wear rates compared to ABS and HDPE at all specified torques due to the high wear resistivity of the POM material (bear until 9.5 Nm in dry conditions). Xu et al. [27] investigated the wear performance of two types of polyacetal gears: homopolymer and copolymer. It was concluded that the two gear types behaved in the same way in the first two phases of running in and linear, however homopolymer POM gear took more cycles than copolymer POM gears. It is worth mentioning that besides the sheer goal of replacing the metals with polymers, environmental aspects should be taken into account. Zorko et al. [28] experimented with a bio-based gear material (polyamide 6.10) with steel pinion and compared it with the neat PA66 at different load levels. PA 6.10 exhibited a lower wear rate than PA66 due to a lower coefficient of friction and temperature. Also, these bio-based materials are non-contaminated to the environment. The surface roughness of steel gears was studied in the research conducted by Johnney et al. [29] to estimate the amount of wear of the polypropylene gear (PP). It was inferred that the increased surface roughness of the mating gears escalates surface temperature, thus accelerating the wear rate of the PP gears. Cerne and Petkovsek [30] used the digital image correlation method (DIC) and edge displacement detection method (EDD) to investigate the amount of deflection and wear of the in-mesh gears. Both methods prove their reliability in detecting the wear in gear meshing. In another study conducted by Soudmand and Shelesh-Nezhad [31] image processing was used to detect the wear of gear made from neat polybutylene terephthalate (PBT) and the same material with montmorillonite (MMT) as a polymer matrix. The results indicated that PBT/MMT is better than neat PBT in performance (more life span than PBT). Temperature also affects wear when it is accompanied by an increase in load and speed [11,32,33,34]. In materials such as POM gears, wear is the most predominant type of failure followed by thermal bending at critical torques. All of the aforementioned studies have evaluated the amount of wear empirically and analytically. So, from a numerical point of view and based on the above analysis, this paper examines the wear inflicted on a polypropylene plastic gear by employing an image processing code to directly detect and compare wear with its initial condition. To obtain this data, the plastic gear undergoes wear testing, during which images of the gear tooth profile are captured. These images are subsequently processed and analyzed in MATLAB to detect and compare the evolution of gear wear over time.

2. Materials and methods

The purpose of this paper as mentioned before is to assess and evaluate the wear occurring on the gear tooth. To accomplish this evaluation, the polymer gear was subjected to wear using a specific apparatus resembling the gear's operation in machinery. This was followed by capturing gear tooth' images, and then applying a code for image processing to disclose the gear tooth profile and estimate it in comparison to its pre-wear condition.

2.1. Materials and specimens

For conducting this test, an injection molded gear made of polypropylene (PP) material was utilized as a pinion. This pinion was produced in the PRC laboratory at German University in Cairo (GUC). PP materials have lower density, low cost, and acceptable mechanical strength [27]. These cons make the PP materials suitable for many applications including gears. After manufacturing the PP pinion by injection molding machine, it was deemed suitable for testing and meshing with a steel gear. The geometrical parameters of both gears are presented in the following **Table 1**.

Table 1. Geometrical specifications of the testing gear pair.

Material	**Polymer (PP)**	**Steel (St50DIN)**
Number of teeth	20	24
Face Width (mm)	5	5
Module (mm)	3	3
Inner Diameter (mm)	15	15
Pitch Diameter (mm)	60	102
Yield Strength (N/mm^2)	35–40	259
Melting Point (°C)	160–165	1370

2.2. The testing machine

Before compel wear on the PP gear through testing, the PP gear must be placed in an environment closely matching its conventional operating conditions, in other words, the polymer gear meshed with steel gear engaging in a wear testing machine to simulate regular operations. It is worth mentioning that this machine has the option of varying centre distance (testing gears with various diameters). Over time, the polymer gear will be worn when the testing machine continuously works in dry conditions. The wear testing machine consists of a source motor which propels the entire system and transmits its power via a belt to the polymer gear shaft, a PP pinion meshes with a steel gear and idler motor which connects the steel gear shaft via a belt and applies resistance torque to the system. This motor simulates a load on the polymer gear. The wear-testing machine setup can be seen in **Figure 1**. The source motor is a GAMAK-type M21D single-phase asynchronous motor, operating at 1400 RPM and with a torque of 2.52 Nm. This motor is directly linked to a polymer gear shaft via a belt of a ratio 1:1. As for the idler motor, it is Ahmed Daoud Group Motor, with a locked rotor torque of 1 Nm. Further details and specifications can be found in the following **Table 2**.

It is worth noting that the continuous operation of gear pair engagement leads to an increase in the temperature of the gears. This temperature increase causes material expansion, especially PP pinion. To prevent this expansion from affecting the engagement of PP pinion to its shaft, a woodruff shaft key was inserted to assure a complete appendage between the pinion and the shaft.

Table 2. Specifications of the source motor [28].

Model	**GAMAK type M21D 71 M 4d**
Rated output (kW)	0.37
Rated speed (RPM)	1400
Rated torque (Nm)	2.52
Rated current (A)	3.2
Efficiency	60%
Moment of inertia (Kg.m^2)	0.0056
Locked rotor torque (Nm)	1.1
Power Factor (cos φ)	0.88

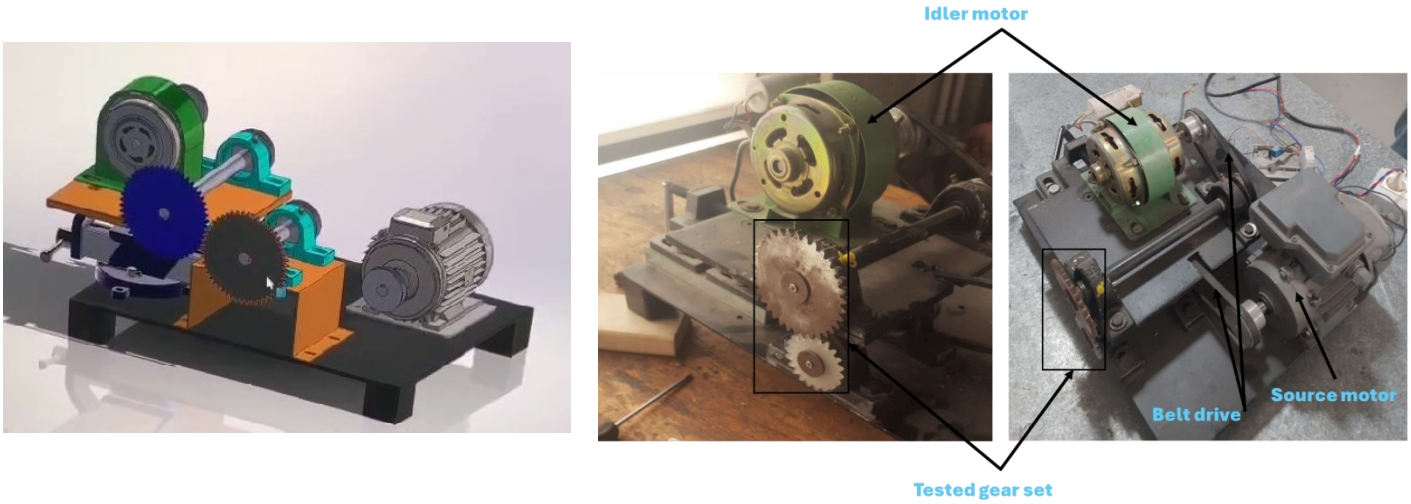

(a) 3D modelling. **(b)** Manufactured machine.

Figure 1. Wear testing machine set up.

2.3. Image and temperature capturing equipment

Using a high-quality digital camera directly correlates with the result accuracy and precise outcomes. It is essential to comprise a camera containing more pixels and high resolution to precisely capture the gear tooth. In this study, the digital camera used is Sony 12 Mega pixel with a resolution of 3024 × 4032 with f/1.8 and f/2.8 apertures, and optical image stabilization. The camera was fixed on a L-Shape bracket attached to the base of the testing machine and focused on the remarked tooth for measurements at a distance of 50 mm. For more test consistency the camera was secured to be stationary from the moment of mounting the gears on the testing machine, passing through capturing the initial pre-wear image till the final image after the machine has ceased to operate. The camera was connected to Arduino board and the figures captured were directly transformed into a Computer. It should be noted that images were captured intermittently swiftly to avoid losing temperature influence on the polymer gear tooth as the flank cools immediately after stopping the test as mentioned in previous studies. As the temperature affects the polymer gears, it was essential to estimate the pinion tooth temperature during the operation to study its effect alongside the wear of the pinion tooth. An infrared thermometer was used to

estimate pinion tooth temperature during the meshing. The thermometer used is handheld no contact Bosh model number GIS500. This thermometer offers a temperature range of −30 ℃ to 500 ℃, ensuring accurate temperature readings at image intervals.

2.4. Gear pair testing

Setting up the wear test machine, image and temperature capturing equipment, the machine operated continually for 5 hours, punctuated by an image capture at the 2nd-hour mark. A specific pinion tooth was defined by a small scratch on the pinion body as it is not certain that all teeth will wear the same way as each other. By defining the pinon tooth, one could not lose track of it at any point when the image was taken (see **Figure 2**).

(a) 0 hours. **(b)** 2 hours. **(c)** 5 hours.

Figure 2. Resulting images of the gear tooth with time interval.

Temperature readings of the specified pinion tooth were recorded at each interval of the operation alongside captured images (refer to **Table 3**). These Images served as input for image processing code calculating the wear percentage resulting from the test.

Table 3. Temperature of plastic pinion tooth in hourly intervals.

Time (hours)	Temperature (℃)
0 (pre-wear)	34.3
1	37.2
2	38.8
3	40.6
4	41
5	43.1

2.5. Image processing code

2.5.1. Preliminary image editing

To ensure no interference between steel and polymer gear teeth which may lead to inaccuracies in the wear comparison along the time intervals, preliminary editing to

crop the defined pinion tooth was required in addition to removing steel gear teeth from the cropped image (polymer gear tooth was the target image for estimating wear), thus facilitating an accurate wear comparison. This editing was done by using GUN Image Manipulation Program (GIMP). The image was cropped to a resolution of 1000 × 1000 pixels to maintain accuracy and consistency in the editing process. This resolution was selected to include the entire tooth from the dedendum to the very top of the tooth as can be seen in **Figure 3**.

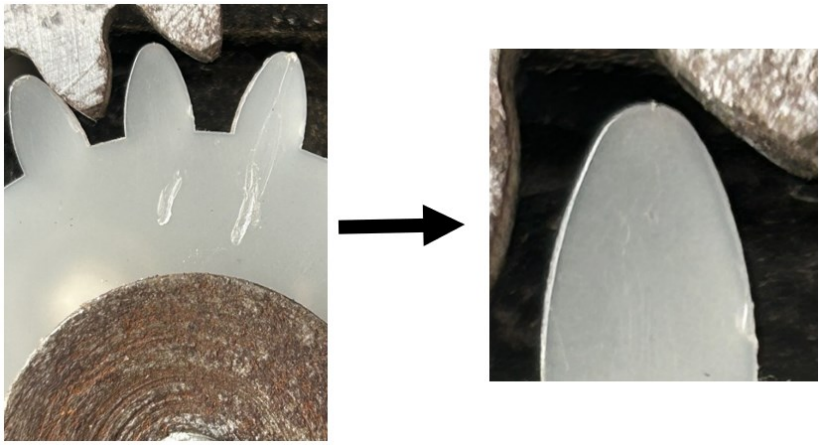

Figure 3. Cropping of the pre-wear image (0 hours).

By using a clone tool in GIMP, the steel gear teeth could be excluded from the cropped image. GIMP allows for selective copying and cloning of an image using a brush tool. **Figure 4** shows how effectively the steel gear teeth have been diminished from the cropped image, leaving the isolated polymer gear tooth for further processing. Despite the background not being a uniform solid colour due to the machine body, this minor variation shouldn't pose an issue. The detection code is designed to filter out background noise, focusing solely on selecting the profile of the plastic gear tooth, ensuring accurate analysis.

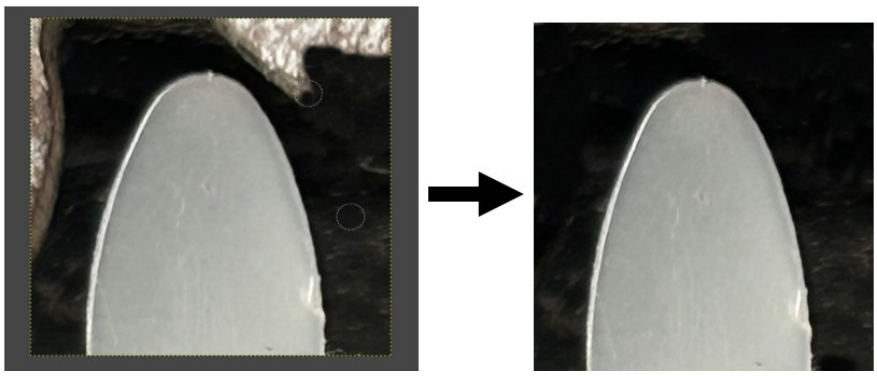

Figure 4. Usage of clone tool on steel gear (left) and pre-wear image post-editing (right).

2.5.2. Detection code

Following the preliminary editing, the edited images will be fed into the detection code, tasked with isolating the plastic gear tooth from the background. The code will then generate a binary mask, also known as a truth mask, of the gear tooth profile. In

this mask, pixels corresponding to the detected object will be turned white (with a value of 1), while all other pixels will be rendered black (with a value of 0), effectively excluding them from further analysis.

This process ensures accurate delineation of the gear tooth for subsequent processing steps. The code is implemented in MATLAB, leveraging functions from the image processing toolbox. This toolbox is renowned for its extensive collection of functions dedicated to image processing algorithms and is typically pre-installed with MATLAB due to its widespread use and popularity among researchers and practitioners. The code commences by reading the edited image of the plastic gear tooth, labelled "PP 0 plastic.jpg". In this nomenclature, 'PP' signifies the material, '0' indicates the testing hour (in this case, the pre-wear image), and 'plastic' denotes the image post-editing, indicating that the steel gear's teeth have been removed. Once the image is retrieved from the computer, it undergoes conversion to grayscale. This conversion eliminates colour information, transforming the image into a 2D matrix with dimensions of 1000 × 1000, representing the pixels with values depending on how bright or dark they are. This grayscale conversion streamlines image processing and facilitates the application of techniques such as binary masking and morphological operations (see **Figure 5**). The demonstrated code can be seen in Appendix A.

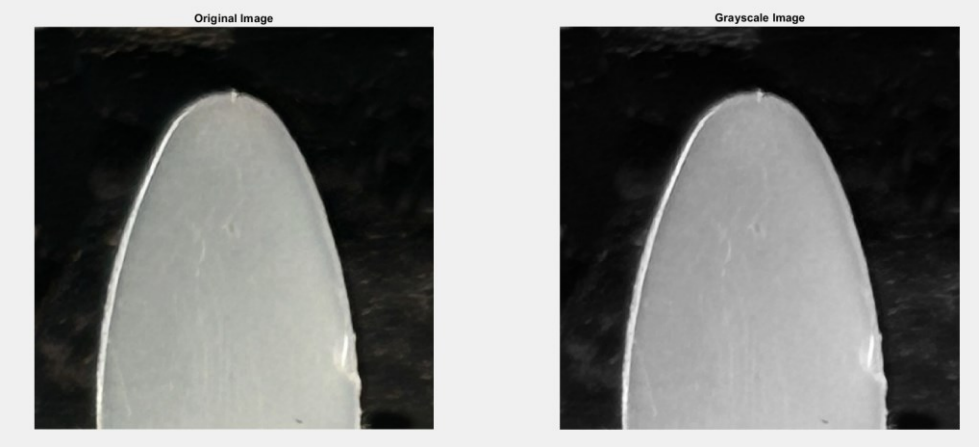

Figure 5. Grayscaling of the gear tooth image.

Following grayscaling, the image undergoes a binary thresholding process. During this process, a threshold value is established, dictating which parts of the image will become white pixels (value 1) and which will become black pixels (value 0). If a grayscale pixel's value exceeds the threshold, it is rendered as white; otherwise, it is rendered as black. It's essential to note that setting a threshold too high may only render the brightest parts of the object visible. Therefore, the threshold value, in this case set at 178, can be adjusted to accommodate different gear images based on the brightness or darkness of the gear tooth. This transformation converts the image from a 1000 × 1000 matrix with pixels of varying values into a 1000 × 1000 matrix of logical values (black 0 or white 1) as demonstrated in **Figure 6**. As depicted in **Figures 6** and **7**, the noise removal step didn't noticeably affect the image since the binary thresholding effectively addressed the background. However, this technique could prove beneficial for images where the background is brighter and inadvertently

captured during thresholding. The primary issue lies in the gaps within the gear tooth profile that haven't been accurately detected.

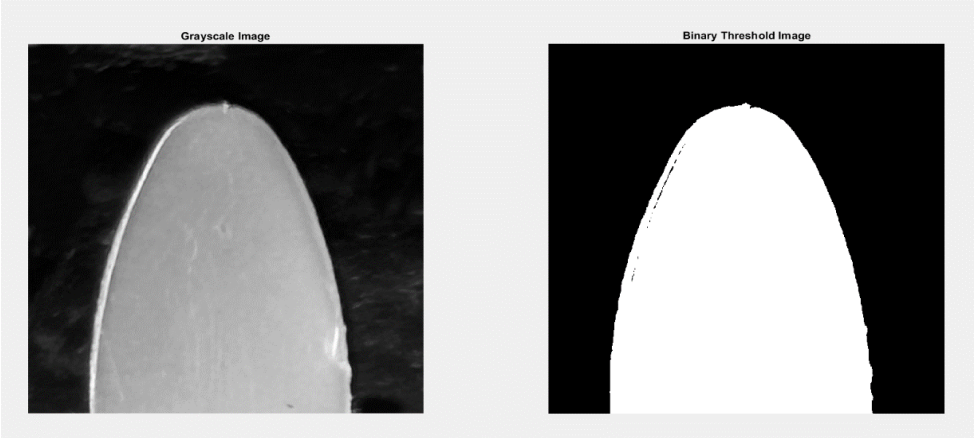

Figure 6. Binary thresholding process of the gear tooth image.

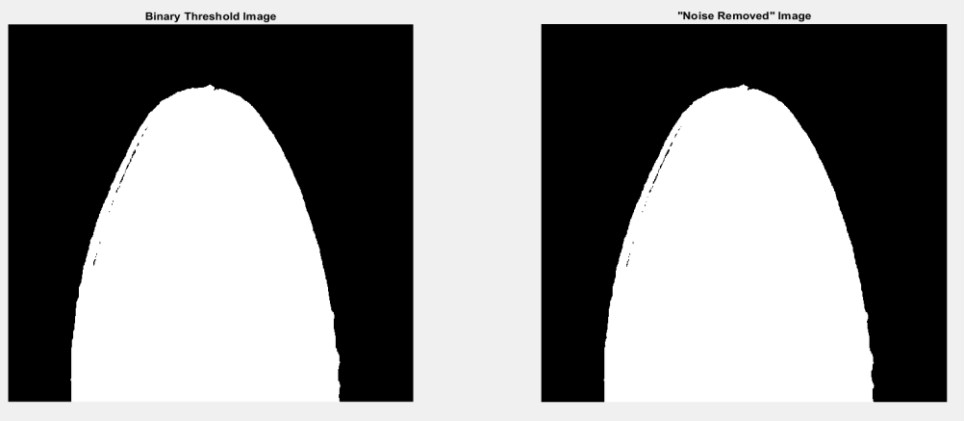

Figure 7. Noise removal in the gear tooth image.

Several solutions can rectify this issue, one of the methods, as employed in this case, is using the 'imfill' function. This function fills in any gaps or holes in image regions, effectively addressing the specific problem of incomplete detection within the gear tooth profile (see **Figure 8**).

To enhance the gear tooth profile, morphological operations are performed in **Figure 9**. A morphological operation involves creating and defining a structuring element to span the object, then joining these structural elements together using the 'imclose' function. The structuring element used in this code was a disk-shaped structure of radius 20 pixels. By applying that to the gear tooth image, the profile is enhanced to be akin to the original.

Following the morphological operation, the outcomes are visualized by displaying the original image alongside the isolated gear tooth profile. Additionally, the resulting binary image is saved on the computer. It bears the same name as the original image, except 'iso' replacing 'plastic' in the filename. This alteration underscores that the saved image represents the isolated binary mask version of that image as shown in **Figure 10**. With the detection code done, its processes are repeated for the 2-hour image and the final 5-hour image. The resulting isolated binary masks are then used as input for the wear percentage code.

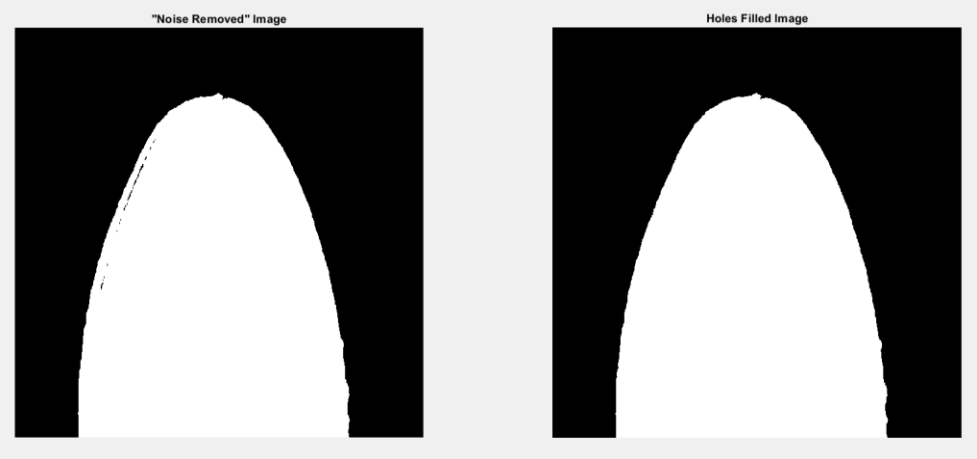

Figure 8. Gap filling the gear tooth image.

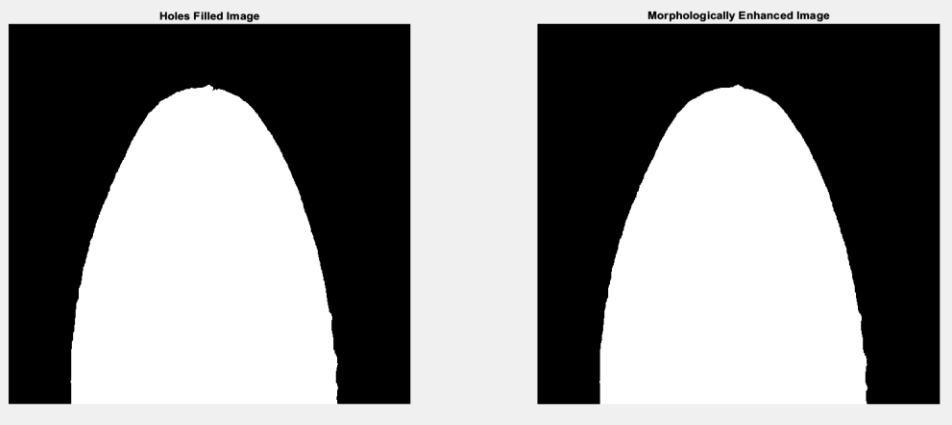

Figure 9. Morphologically enhancing the gear tooth image.

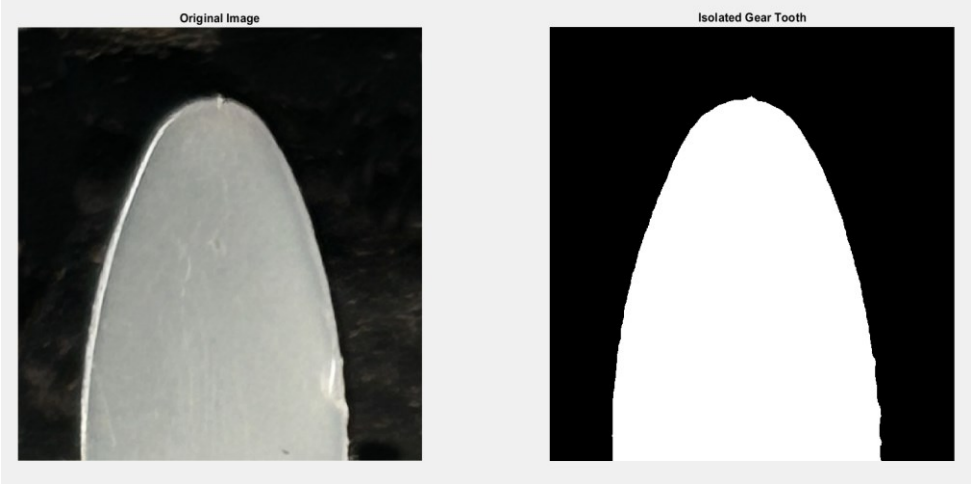

Figure 10. Output of the detection code.

2.5.3. Wear percentage calculation

The wear percentage code is designed to compute the percentage of wear on the gear tooth relative to the pre-wear image. Since all the images captured during testing undergo the same parameters of distance, angle, and zoom level, and are cropped to the same resolution without compromising quality, and processed using the same

detection code, they are effectively standardized. This ensures uniform positioning and processing of all images. Consequently, determining the wear percentage becomes straightforward. It involves counting all the white pixels in each image, subtracting the values from the pre-wear image, and then dividing by the pre-wear value to obtain the percentage of wear (wear percentage code is presented in the Appendix B) as shown by the following Equation (1).

$$W(\%) = \frac{No.of\ white\ pixels\ prewear - No.of\ white\ pixels\ worn}{No.of\ white\ pixles\ prewear} \times 100 \quad (1)$$

The wear percentage code being applied to an example binary masked gear tooth image isn't related to the test subject used in the materials and methods section, as this serves as an arbitrary example. The results of that test subject are displayed in the results and discussion section.

3. Results and discussion

Throughout the experimentation process, a systematic approach was adopted to capture images of the plastic gear tooth at regular intervals during testing. These images were subsequently processed using the detection code, which isolated the gear tooth profile and facilitated wear analysis. Upon completion of the experimentation phase and implementation of the detection code on all images, a comprehensive analysis was conducted to assess wear progression over time. The wear percentage was calculated for each image relative to the pre-wear image, providing insights into the extent of wear experienced by the gear tooth throughout the testing duration. The final results revealed a progressive increase in wear percentage over successive images, indicative of the cumulative effects of operational conditions on the gear tooth. Visual inspection of the images further corroborated these findings, with observable changes in wear patterns and surface characteristics.

3.1. Detection code results

Upon running the detection code, the pre-wear image served as the baseline for comparison. Subsequent images captured during the testing process were also processed using the same parameters and techniques outlined in the materials and methods section. To accurately represent the amount of testing undergone by each gear tooth image, we have adopted a nomenclature that includes both the timestamp and the number of cycles. This approach ensures consistency and uniformity in measuring the testing duration, accounting for potential variations in machine RPM and testing time between different tests.

The number of cycles for each image can be calculated using the following Equation (2).

$$No.of\ cycles = Time\ (mins)\ x\ input\ speed\ (RPM) \quad (2)$$

The previous equation provides a standardized metric for quantifying the testing duration and accurately tracking the wear progression of the gear tooth over time. Utilizing this equation and given that the machine operated at 1400 RPM as detailed in the materials and methods section, 2 hours give 168,000 cycles, and 5 hours give 420,000 cycles. **Figure 11** shows the zero hours (pre-wear) where it's evident that the

gear tooth profile exhibits some imperfections, particularly noticeable at the bottom right side and the top of the tooth, even before wear occurs. These nuances and imperfections may stem from manufacturing processes, such as excessive grinding during polishing, which can introduce irregularities in the gear tooth surface.

Figure 11. Detection code output for pre-wear image.

However, it's crucial to note that these imperfections in the baseline reference do not adversely affect the performance of the detection code. Since this image serves as the baseline reference for wear analysis, any wear incurred during testing will further diminish and alter the tooth profile, regardless of the initial imperfections.

After 168,000 cycles, the second picture was taken and has been run through preliminary editing and the detection code, displaying the following **Figure 12**. This figure highlights a noticeable visual disparity between the pre-wear image and the image captured after 2 hours of testing. For instance, the absence of the small chip at the top of the gear tooth in the latter image suggests that wear has occurred, resulting in the alteration or removal of this feature. Additionally, subtle changes in the profile of the gear tooth, particularly on the right side, further indicate the occurrence of wear in that region. At a total of 420,000 cycles, the final image was captured and run through the detection code, displaying the following **Figure 12**.

Figure 13 illustrates the continued evolution in the gear tooth profile, indicating further wear progression compared to the previous image. Notably, additional wear is evident around the top portion of the gear tooth, suggesting ongoing degradation in this area. Furthermore, the profile changes observed on the right and bottom-left sides of the gear tooth indicate continued alterations to the surface characteristics, possibly due to the accumulation of wear-induced damage.

Indeed, a careful examination of all the images reveals that significant deformation has not occurred in the gear tooth. If deformation had taken place, it would likely manifest as a noticeable angular displacement from the start of the dedendum, particularly indicating high-temperature deformation. The absence of such angular displacement across the images underscores the importance of conducting a thorough study of the images after processing them through the detection code. Beyond simple wear, it's crucial to scrutinize the images for any signs of deformation, such as distortion, warping, or irregularities in the gear tooth profile. These indicators

can provide valuable insights into the performance and integrity of the gear tooth under varying operational conditions.

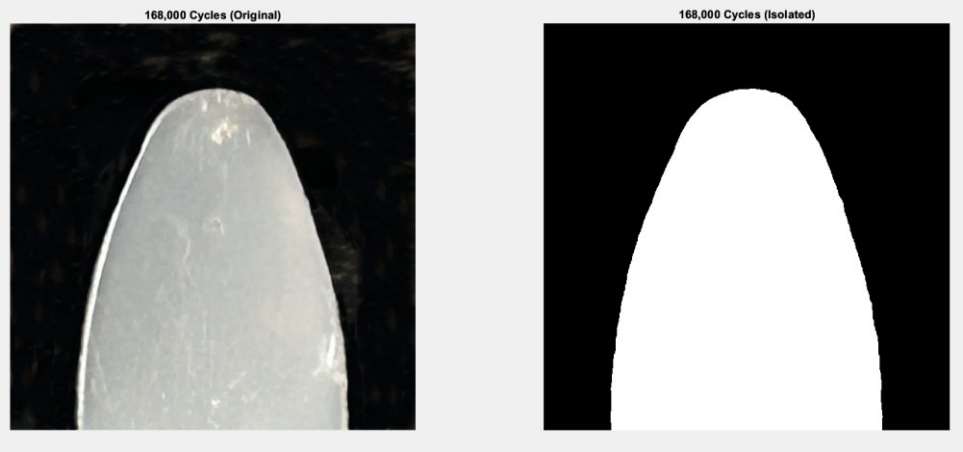

Figure12. Detection code output for 2-hour gear tooth image.

Figure 13. Detection code output for 5-hour gear tooth image.

3.2. Polymer gear wear estimation code

In this section, a quantitative analysis provided a numerical measure of the extent of wear experienced by the gear tooth over time, complementing the visual observations discussed previously. Using the wear percentage code, wear percentages were calculated as mentioned before by comparing the number of white pixels in each image to those in the pre-wear image. This comparison enables us to quantify the relative change in the exposed surface area of the gear tooth due to wear.

With the 2-hour image rendered into an isolated binary mask of the gear tooth profile, and by running the wear percentage code in comparison with the pre-wear image, the code resulted in a wear of 0.2%. This is presented in **Figure 14**. While the 5-hour image has undergone the detection code, it was inputted into the wear percentage code in comparison to the pre-wear image, displaying the following **Figure 15** with approximately 2.5% of a worn tooth. The close correspondence between visual and numerical analyses enhances our confidence in the results and underscores the importance of employing a multi-faceted approach to wear assessment.

Figure 14. Pre-wear and 2-hour image wear percentage output.

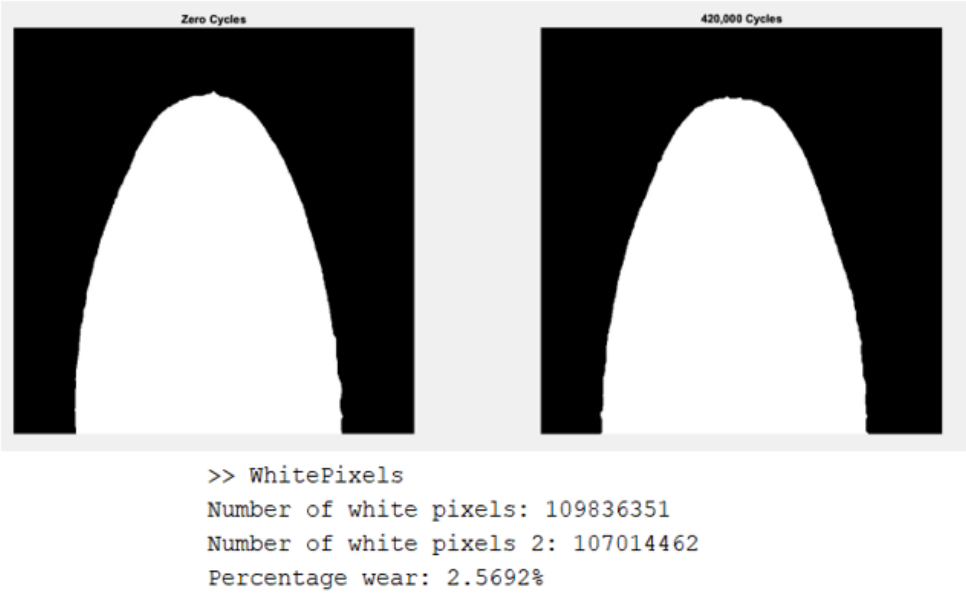

Figure 15. Pre-wear and 5-hour image wear percentage output.

3.3. Data compilation

Figure 16 represents a graph illustrating the wear percentage data collected previously. In this graph, the pointing triangles represent the experimental data points, providing a visual representation of wear progression over time. Additionally, the red solid curve depicts a cubic interpolation of the data, which attempts to interpolate the wear percentage values into a non-linear function.

The use of cubic interpolation is particularly beneficial when the nature of wear progression is unknown and cannot be easily expressed as a linear equation. By utilizing cubic interpolation, we can generate a smooth curve that closely approximates the wear percentage data points, enabling us to visualize wear progression more comprehensively. This graph facilitates the visualization of wear trends and patterns over time, providing insights into the rate and magnitude of wear experienced by the gear tooth throughout the testing duration. By analysing the wear

percentage graph, researchers can identify any notable trends, anticipate potential wear-related issues, and inform future research efforts aimed at optimizing gear performance and reliability.

Figure 17 illustrates a graph of temperature data collected during operation and testing, employing the same technique of cubic interpolation used in **Figure 16**. Similar to the wear percentage graph, the red solid curve represents the cubic interpolation of the temperature data points, providing a smooth curve that captures trends and patterns in temperature variation over time. It is noted that at low temperatures (below 370 ℃) and up to (38.50 ℃), the mechanism of wear was increasing slowly and then at a higher temperature and increased number of cycles, the mechanism increased rapidly. The material used is polypropylene without any additives and expecting at elevated temperature a large decrease in hardness. Further investigation and comparison with wear equations are needed for deep research direction.

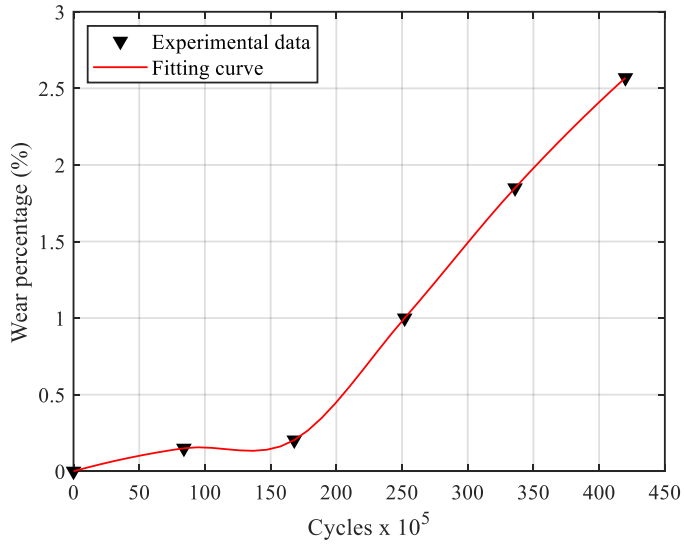

Figure 16. Wear test results for polypropylene against steel at 1.52 Nm.

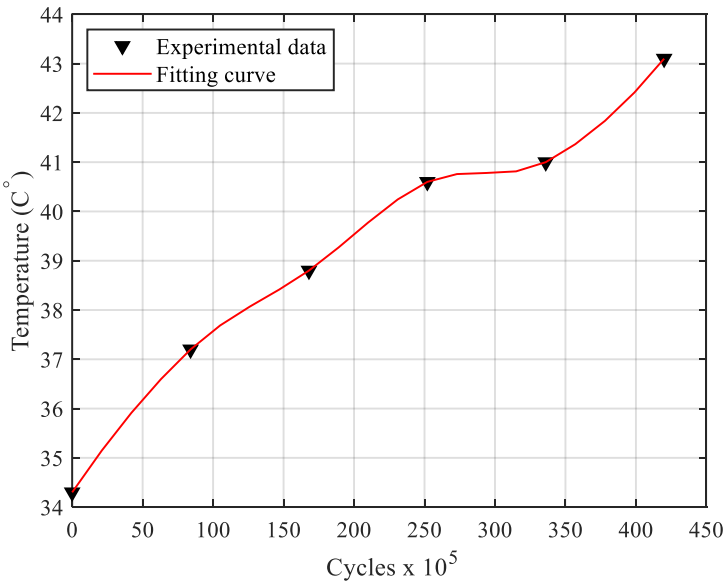

Figure 17. Temperature test results for polypropylene against steel at 1.52 Nm.

4. Conclusion

PP gear was meshed with steel gear on the wear test rig to estimate the amount of wear of the polymer gears at different cycle times. By capturing images of the PP pinion during operation at different time intervals, these images served as an input to a code for image processing to determine the amount of wear precisely without any sign of deformation. The code successfully helped in detecting the wear of the defined tooth of the PP pinion at various cycle times. Detecting tooth temperature using an infrared thermometer during the gear pair mesh assisted in accurately evaluating the tooth wear by image processing code. With this code, the wear could be detected at 2 and 5 hours with 0.2% and 2.5% respectively. It also collaborates in building graphs to explore the trends and patterns in temperature variation over time.

The paper explored avenues of assessing wear that have barely been applied in previous research papers. This research is merely the beginning of a field of gear optimization that is packed with untapped potential. With several improvements upon the methodology applied in this paper, researchers can evolve their understanding of polymers and their properties being implemented into power transmission systems. Although this novel technique succeeded in predicting the amount of wear present on the side of the gear teeth, further study needs to be conducted to predict the wear on the gear teeth flank. This technique can predict the early wear in gears while on-site without the need for disassembly. This will save time and maintenance costs, and improve the efficiency of power transmission.

Author contributions: Conceptualization, MGE and HAH; methodology, MGE and HAH; software, MGE; validation, MGE, MAE and HAH; formal analysis, MGE, MAE and HAH; investigation, MGE, MAE and HAH; resources, MGE, MAE and HAH; data curation, MGE, MAE and HAH; writing—original draft preparation, MGE, MAE and HAH; writing—review and editing, MGE, MAE and HAH; visualization, MGE, MAE and HAH; supervision, HAH. All authors have read and agreed to the published version of the manuscript.

Conflict of interest: The authors declare no conflict of interest.

References

1. Mao K, Langlois P, Hu Z, et al. The wear and thermal mechanical contact behaviour of machine cut polymer gears. Wear. 2015; 332–333: 822–826. doi: 10.1016/j.wear.2015.01.084
2. Elsiedy M, Hegazi H, Elkassas A, Zayed A. Optimum Design of Metallic and Plastic Cylindrical Gears Using Naturally-Inspired Algorithms: A Review. Journal of Engineering Research. 2023; 7(6).
3. Ignatijev A, Glodež S, Kramberger J. Computational Model for Analysing the Tooth Deflection of Polymer Gears. Polymers. 2024; 16(5): 677. doi: 10.3390/polym16050677
4. Jain M, Patil S, Ghosh SS. A review on failure characteristics of polymeric gears. In: Proceedings of the 1st international conference on advances in mechanical engineering and nanotechnology (ICAMEN 2019); 8–9 March 2019; Jaipur, India.
5. Snyder L. At the PEEK of polymer food chain. Gear Technology. 2010; 26–28.
6. Zorko D, Tavčar J, Bizjak M, et al. High cycle fatigue behaviour of autoclave-cured woven carbon fibre-reinforced polymer composite gears. Polymer Testing. 2021; 102: 107339. doi: 10.1016/j.polymertesting.2021.107339
7. Singh PK, Siddhartha, Singh AK. An investigation on the thermal and wear behavior of polymer based spur gears. Tribology International. 2018; 118: 264–272. doi: 10.1016/j.triboint.2017.10.007

8. Mao K, Greenwood D, Ramakrishnan R, et al. The wear resistance improvement of fibre reinforced polymer composite gears. Wear. 2019; 426–427: 1033–1039. doi: 10.1016/j.wear.2018.12.043
9. Elsiedy MA, Zayed AA, Hegazi HA, et al. Optimization of polyoxymethylene spur gear pair using meta-heuristic algorithms: A comparative study. Journal of Engineering Tribology. 2024; 238(9): 1153–1174. doi: 10.1177/13506501241250369
10. Elsiedy MA, Hegazi HA, El-Kassas AM, et al. Multi-objective design optimization of polymer spur gears using a hybrid approach. Journal of Engineering and Applied Science. 2024; 71(1). doi: 10.1186/s44147-024-00443-5
11. Ghazali WM, Idris DMND, Sofian AH, et al. A review on failure characteristics of polymer gear. EDP Sciences. 2017; 90: 01029. doi: 10.1051/matecconf/20179001029
12. Tunalioglu MS, Torun T. The investigation of wear on three-dimensional printed spur gears. Journal of Process Mechanical Engineering. 2021; 235(6): 2027–2034. doi: 10.1177/09544089211027732
13. Tunalioglu MS, Agca BV. Wear and Service Life of 3-D Printed Polymeric Gears. Polymers. 2022; 14(10): 2064. doi: 10.3390/polym14102064
14. Hriberšek M, Kulovec S, Ikram A, et al. Technological optimization and fatigue evaluation of carbon reinforced polyamide 3D printed gears. Heliyon. 2024; 10(13): e34037. doi: 10.1016/j.heliyon.2024.e34037
15. Muratovic E, Muminovic A, Pervan N, et al. Assessing Wear Coefficient and Predicting Surface Wear of Polymer Gears: A Practical Approach. Engineering, Technology & Applied Science Research. 2024; 14(4): 15923–15930. doi: 10.48084/etasr.7421
16. Hlebanja G, Hriberšek M, Erjavec M, et al. Durability Investigation of plastic gears. MATEC Web of Conferences. 2019; 287: 02003. doi: 10.1051/matecconf/201928702003
17. İmrek H. Performance improvement method for Nylon 6 spur gears. Tribology International. 2009; 42(3): 503–510. doi: 10.1016/j.triboint.2008.08.011
18. Mao K. A new approach for polymer composite gear design. Wear. 2007; 262(3–4): 432–441. doi: 10.1016/j.wear.2006.06.005
19. Mao K, Chetwynd DG, Millson M. A new method for testing polymer gear wear rate and performance. Polymer Testing. 2020; 82: 106323. doi: 10.1016/j.polymertesting.2019.106323
20. Mao K, Hooke CJ, Walton D. Acetal gear wear and performance prediction under unlubricated running condition. Journal of Synthetic Lubrication. 2006; 23(3): 137–152. doi: 10.1002/jsl.17
21. Mao K, Li W, Hooke CJ, et al. Polymer gear surface thermal wear and its performance prediction. Tribology International. 2010; 43(1–2): 433–439. doi: 10.1016/j.triboint.2009.07.006
22. Mao K, Langlois P, Madhav N, et al. A comparative study of polymer gears made of five materials. Gear Technology. 2019.
23. Mao K, Li W, Hooke CJ, et al. Friction and wear behaviour of acetal and nylon gears. Wear. 2009; 267(1–4): 639–645. doi: 10.1016/j.wear.2008.10.005
24. Breedsa AR, Kukureka SN, Maob K, et al. Wear behaviour of acetal gear pairs. Wear. 1993; 166: 85–91. doi: 10.1016/0043-1648(93)90282-Q
25. Kukureka SN, Chen YK, Hooke CJ, Liao P. The wear mechanisms of acetal in unlubricated rolling-sliding contact. Wear. 1995; 185: 1–8. doi: 10.1016/0043-1648(94)06575-6
26. Li W, Wood A, Weidig R, et al. An investigation on the wear behaviour of dissimilar polymer gear engagements. Wear. 2011; 271(9–10): 2176–2183. doi: 10.1016/j.wear.2010.11.019
27. Xu X, Gao F, Lopera Valle A, et al. Wear Performance of Commercial Polyoxymethylene Copolymer and Homopolymer Injection Moulded Gears. Tribology in Industry. 2021; 43(4): 561–573. doi: 10.24874/ti.1039.01.21.04
28. Zorko D, Demšar I, Tavčar J. An investigation on the potential of bio-based polymers for use in polymer gear transmissions. Polymer Testing. 2021; 93: 106994. doi: 10.1016/j.polymertesting.2020.106994
29. Johnney MA, Kumar P, Senthilvelan S. The effect of the mating gear surface over the durability of injection-molded polypropylene spur gears. Journal of Engineering Tribology. 2016; 230(12): 1401–1414. doi: 10.1177/1350650116635423
30. Černe B, Petkovšek M. High-speed camera-based optical measurement methods for in-mesh tooth deflection analysis of thermoplastic spur gears. Materials & Design. 2022; 223: 111184. doi: 10.1016/j.matdes.2022.111184
31. Soudmand BH, Shelesh-Nezhad K. Study on the gear performance of polymer-clay nanocomposites by applying step and constant loading schemes and image analysis. Wear. 2020; 458–459: 203412. doi: 10.1016/j.wear.2020.203412

32. Bravo A, Koffi D, Toubal L, et al. Life and damage mode modeling applied to plastic gears. Engineering Failure Analysis. 2015; 58: 113–133. doi: 10.1016/j.engfailanal.2015.08.040
33. Zaamout M. The Wear Behaviour of Nylon 66 and its Composites under Impact Loading. Journal of King Abdulaziz University-Engineering Sciences. 2005; 16(1): 79–95. doi: 10.4197/eng.16-1.6
34. Mertens AJ, Senthilvelan S. Mechanical and tribological properties of carbon nanotube reinforced polypropylene composites. Journal of Materials: Design and Applications. 2016; 232(8): 669–680. doi: 10.1177/1464420716642620

Appendix A

```
% Read the image
originalImage = imread('PP 0 plastic.jpg');

% Convert to grayscale
grayImage = rgb2gray(originalImage);

% Thresholding to separate the gear tooth
binaryImage = grayImage > 178;

% Remove small objects/noise
binaryImage = bwareaopen(binaryImage, 100);

% Fill holes in the binary image
binaryImage = imfill(binaryImage, 'holes');

% Morphological operations to enhance the gear tooth
se = strel('disk', 20); % Define a disk-shaped structuring element
binaryImage = imclose(binaryImage, se);

% Display the results
figure;
subplot(1, 2, 1);
imshow(originalImage);
title('Original Image');
subplot(1, 2, 2);
imshow(binaryImage);
title('Isolated Gear Tooth');

% Save the isolated gear tooth image
imwrite(binaryImage, 'PP 0 iso.jpg');

```

Figure A1. MATLAB gear tooth detection code.

Appendix B

```
% Read the image
binary_img = imread('PP 0 iso.jpg');

% Count the number of white pixels (pixels with value 1)
num_white_pixels = sum(binary_img(:));

% Display the number of white pixels
disp(['Number of white pixels: ', num2str(num_white_pixels)]);

% Read the 2nd image
binary_img2 = imread('PP 2 iso.jpg');

% Count the number of white pixels (pixels with value 1)
num_white_pixels2 = sum(binary_img2(:));

% Display both images
figure;
subplot(1, 2, 1);
imshow(binary_img);
title('Initial');
subplot(1, 2, 2);
imshow(binary_img2);
title('2 hours');

% Display the number of white pixels
disp(['Number of white pixels 2: ', num2str(num_white_pixels2)]);

% Calculate and display the wear percentage
percent_wear = ((num_white_pixels - num_white_pixels2)/num_white_pixels)*100;
disp(['Percentage wear: ', num2str(percent_wear), '%']);
```

Figure B1. Wear percentage code.

Mechanical Engineering Advances 2025, 3(1), 1962.
https://doi.org/10.59400/mea1962

Article

Implementing multi criteria decision making methods for computing complexity involved in industrial investment castings

Nikunj Maheta, Amit Sata*

Department of Mechanical Engineering, Marwadi University, Rajkot 360003, India
*** Corresponding author:** Sata Amit, amit.sata@marwadieducation.edu.in

CITATION

Maheta N, Sata A. Implementing multi criteria decision making methods for computing complexity involved in industrial investment castings. Mechanical Engineering Advances. 2025; 3(1): 1962. https://doi.org/10.59400/mea1962

ARTICLE INFO

Received: 1 January 2024
Accepted: 14 February 2024
Available online: 18 December 2024

Abstract: Investment casting is admired for its ability to produce industrial castings with remarkable precision, exceptional exterior finish and complex designs among diverse industrial application. Traditionally, the complexity of these castings is generally assessed qualitatively while quantitative measurement of this complexity remains largely unexplored. To identify the various parameters that affects the complexity of industrial investment casting, an in-person industrial survey was carried out in one of the major investment casting clusters that accounts for nearly 25% of India's investment casting foundries. Through this survey it was found that complexity of investment casting is determined by three factors related to geometry, features and manufacturability. These three factors are further driven by 19 elements and 52 attributes. These 52 attributes are further characterised by 212 meta-attributes. This research focuses on applying multi-criteria decision-making methods to quantify the complexity affects in manufacturing industrial investment castings. Numerous methodologies within the domain of Multi-Criteria Decision-Making (MCDM) have been explored to determine the appropriate weightage for the factors, elements, attributes and meta-attributes involved. It was observed that for the specific problem mentioned, the Weighted Criteria Approach (WCA) and Analytical Hierarchy Process (AHP) were identified as suitable choices, aligning well with the required level of accuracy. The result obtained through these methods were used to compute the complexity of industrial castings. The proposed complexity index was validated using various industrial castings and proved to be a valuable tool for designers in adopting investment casting process for producing complex castings.

Keywords: investment casting; complexity index; multi-criteria decision-making; weighted criteria approach; analytical hierarchy process

1. Introduction

Investment casting is a long-established manufacturing process used for developing complex castings with high precision, tight dimensional control and excellent surface finish. Investment casting process extends its application across diverse sectors such as aerospace, bio-medical, chemical, automobile and defense etc. The process contains several sub stages begins with development of die and wax pattern. A ceramic material is invested to the wax pattern to build a shell followed by dewaxing to form a cavity. This ceramic shell is then baked and filled with molten metal. After molten metal cooling, fettling is carried out to remove gating and feeding system followed by finishing of the component. Finally, the castings are thoroughly measured and verified to ensure quality standards are met.

An in-person industrial survey was carried out in an important investment casting cluster representing about 25% of India's total investment casting foundries. This survey intended to gain comprehensive insights related to capacity, capability,

competency, concerns and challenges of these foundries. It was discovered that these foundries employ a holistic approach to producing industrial castings through investment casting process. Typically, the decision to adopt investment casting process is made by the design and manufacturing teams based on a qualitative assessment of the production process. However, erroneous selection often leads to more shop floor trials that can waste resources, extend lead times and lower overall productivity. Moreover, the successful production of industrial castings through investment casting rest on various parameters related to geometry, desired features and manufacturability. This highlights the need for a systematic approach in selecting the investment casting process for optimum outcomes.

2. Prior work

Numerous investigators have endeavoured to develop complexity index that assist in decision-making to select appropriate manufacturing process for industrial components. Oliver et al. [1] proposed a method for assessing the complexity of manufacturing processes in both machining and layered manufacturing. Merkt et al. [2] presented a geometric complexity assessment within an Integrative Technology Evaluation Model known as ITEM. The proposed model includes a product, process, economic and technological factors to measure geometric complexity. Conner et al. [3] introduced a modified complexity factor based on geometric attributes. This factor serves as a crucial factor in selection of an additive manufacturing process and a subtractive manufacturing process for a particular industrial component. Hosseini et al. [4] presented a shape complexity index specifically designed for H-shaped forging. This index incorporates several geometric attributes of the process. It was found that proposed index proves valuable in determining the ideal number of preform steps.

Pradel et al. [5] discovered the impact of complexity on the time required for the building process for the material extrusion and jetting. It was found that factors related to geometry contribute to the overall duration of the building process. Qamar et al. [6] extended the application of shape complexity to predict process parameters, defects, friction and cost involved in extrusion process. Qamar et al. [7] explored the effects of profile complexity on various aspects of the cold extrusion process including process parameters and occurrence of defects. It was concluded that dies with more intricate geometries resulted in a non-uniform flow of metal and leading to an increased requirement for extrusion force.

Joshi et al. [8] presented shape complexity factor that takes into account various geometric features of the desired casting. This index was afterward correlated with both tooling and manufacturing costs providing valuable insights into the intricate relationship between geometric considerations and the associated economic implications in the sand casting process. Martof et al. [9] demonstrated a complexity assessment method using computer aided design models to identify the optimal and economical approach for casting. This tool assesses interior and exterior complexity. This innovative complexity assessment tool was applied to inform decisions concerning the potential integration of additive manufacturing techniques with conventional manufacturing process.

It was observed from comprehensive study of literature reported in direction of development of complexity index that they are mostly related to Multi-Criteria Decision Making (MCDM) problems. MCDM methods are employed for outranking relations, global ranking, relative weight computation and preferences for complex decision making problems and its use has been exponentially increase in last thirty years [10,11]. Different MCDM methods including Analytical Hierarchy Process (AHP), Fuzzy Analytical Hierarchy Process (FAHP), Preference Ranking Organization Method for Enrichment Evaluation (PROMETHEE), Analytic Network Process (ANP), Decision Making Trial and Evaluation Laboratory (DEMATEL), Technique for Order Preference by Similarity to Ideal Solution (TOPSIS), Elimination and Choice Translating Reality (ELECTRE), Compromise Ranking Method (VIKOR) and Weighted Criteria Approach (WCA) were widely employed in decision making applications. Detailed understanding of these methods as well as their capabilities are discussed in various technical literatures published in that direction [12–20]. It was observed that TOPSIS, VIKOR, PROMETHEE, DEMATEL and ELECTRE methods are used for finding best alternative solution and ANP is used for finding solution of network related problem. Furthermore, it was also concluded that WCA method is useful in computation of relative weightage for early stage of complex decision making problems. It was also revealed from a comprehensive literature published in the direction of MCDM methods and its applications that AHP and FAHP were widely employed for finding relative weightage of various parameters related to complex MCDM problems [21].

Numerous researchers have implemented WCA and AHP for calculating weightage in various engineering problem. Karthik et al. [22] established a method to adopt a metal casting process based on a WCA. The proposed methodology comprises several criteria related to geometric and manufacturing parameters for choosing the metal casting process. Fadzli et al. [23] considered use of kenaf fibers compared to usual fibers for friction material using WCA. It was recognized that selection of kenaf fibers using WCA provides possible use as a friction material. Anjum et al. [24] proposed a method based on WCA for measurement of performance. It was identified that the WCA provides a valuable technique in software reliability growth models comparisons.

Akarte et al. [25] developed web-based system for the assessment of casting suppliers. The relative weightage of the criteria has been computed using the AHP. This system proves valuable in evaluating the compatibility of product, process and producer. Chougale et al. [26] demonstrated shape complexity for sand casting process using parameters related to geometry and process. Shape complexity was established by comparing the surface area and volume of the intended casting with that of a simple geometric shape like a cube. The AHP was utilized for pairwise comparisons enabling the calculation of relative weightage for different parameters. Joshi et al. [27] implemented AHP to calculate the relative weightage of several criteria in the early assessment of castability. This proposed methodology presents a systematic approach for assessing the manufacturability of casting design during the early stage of the design process.

It was concluded from the published literature that WCA as well as AHP were more suitable for calculating relative weightage of influencing parameters. In this

paper, implementation of a MCDM methods for computing complexity index of investment casting process has been demonstrated.

3. Methodology

An in person industrial survey was carried out in one of the important clusters of investment casting foundries that represents 30% of total investment casting foundries of India. This survey mainly focused on collection and interpretation of inputs received from investment casting foundries that further categorized for development of complexity index [28]. Industry experts provided input to recognize the key parameters related to geometry, features and manufacturability that affect the complexity of the investment casting process. This information was methodically categorized into factors, elements, attributes and meta-attributes to facilitate complexity index calculation for the investment casting process. It was observed that the geometry factor is primarily influenced by two main elements: surface characteristics and dimensional characteristics. The features factor is driven by eight elements that include hole, slot, groove, fillet, chamfer, hollow region, rib and boss. The manufacturability factor is influenced by nine elements encompassing type of alloy, property requirements, bulk density, melting aids, solidification aids, supplementary aids, melting temperature, batch size and application. Furthermore, the dimensional characteristics element is associated with four attributes: overall length, height, width, and average thickness. Similarly, the surface characteristics element is determined by three attributes: flat, curved, and slanted surfaces.

Overall, it was found that complexity is driven by 3 factors (broad category of parameters), 19 elements (characteristics of the factors), 52 attributes (possible variations of elements) and 212 meta-attributes (values of each variation for attributes). A framework designed for all factors, elements, attributes and meta-attributes is shown in **Figure 1**. These recognized parameters were then organized into a hierarchical structure to enable the calculation of relative weightage. This weightage calculation was achieved using the WCA and AHP. In the WCA, equal importance is assigned to all criteria and a value scale is established for each level of the hierarchy. For the AHP, inputs regarding the relative importance of criteria are collected from industry experts. These inputs are then used to calculate the geometric mean, determine the relative weightage and assess the consistency ratio to ensure reliability in decision-making. The detailed calculation of the relative weightage has been demonstrated in the published literature [29,30].

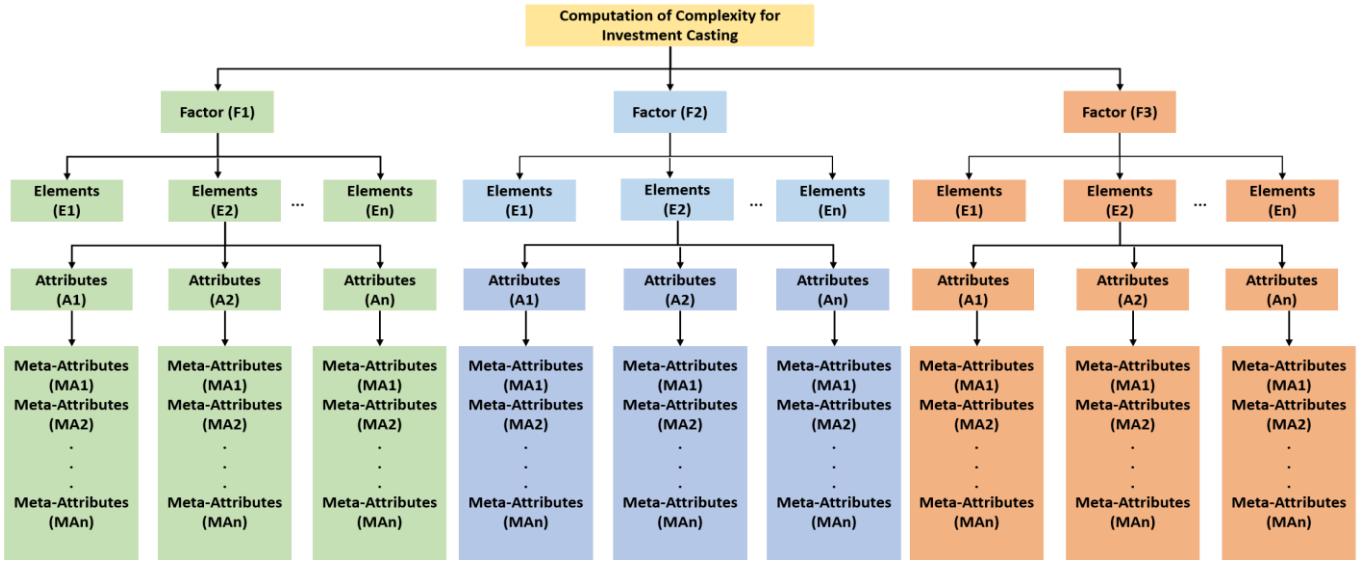

Figure 1. Structure of factor, elements, attributes and meta-attributes for computing complexity index [29].

To demonstrate the application of the complexity index in selecting the investment casting process, a set of specific industrial castings were chosen as use cases focusing on the architecture, automobile, biomedical, chemical and machine tool sectors. This selection provides different requirements of these sectors by investment casting process. The complexity index for each industrial casting was computed and presented in **Tables 1** to **5**. Meta-attributes related to all factors for each selected casting were collected from investment casting foundries that provides a accurate industry perspective.

Table 1. Industrial casting 1.

Attributes	Meta Attributes	Complexity WCA	Complexity AHP
Overall Length (mm)	235.90	1.37	0.20
Overall Height (mm)	134.60	1.37	0.16
Overall Width (mm)	235.90	4.12	0.12
Average Thickness (mm)	9.85	4.12	1.03
Surface Characteristics	C	5.50	12.28
Number of Holes	1.00	0.13	0.02
Maximum Length of Hole (mm)	27.20	0.68	0.02
Maximum Diameter of Hole (mm)	18.60	0.68	0.22
Contour of Hole (Circular, Square)	C	0.34	0.10
Open to Surface (Flat, Curvature))	F	0.34	0.14
Type of Hole (Through, Blind)	T	0.34	0.19
Number of Slots	-	-	-

Table 1. (*Continued*).

Attributes	Meta Attributes	Complexity WCA	Complexity AHP
Maximum Length of Slot (mm)	-	-	-
Maximum Width of Slot (mm)	-	-	-
Maximum Depth of Slot (mm)	-	-	-
Number of Grooves	2.00	0.20	0.08
Maximum Length of Groove (mm)	68.10	0.34	0.20
Maximum Width of Groove (mm)	37.70	1.03	0.11
Maximum Depth of Groove (mm)	37.70	1.03	1.83
Number of Fillets	22.00	2.06	0.14
Maximum Radius of Fillet (mm)	3.00	2.06	0.18
Number of Chamfers	-	-	-
Chamfer Angle (degree)	-	-	-
Distance (mm)	-	-	-
Number of Hollow Regions	-	-	-
Maximum Length of Hollow Region (mm)	-	-	-
Maximum Diameter of Hollow Region (mm)	-	-	-
Number of Ribs	8.00	0.61	0.05
Maximum Length of Rib (mm)	50.61	1.03	0.09
Maximum Thickness of Rib (mm)	5.80	1.03	0.19
Maximum Width of Rib (mm)	17.52	0.68	0.07
Number of Bosses	-	-	-
Maximum Diameter of Boss (mm)	-	-	-
Maximum Thickness of Boss (mm)	-	-	-
Alloying Elements	9.00	2.20	0.36
Hardness (HRC)	19.00	0.73	0.39
Relative Density (gm/cm^3)	8.00	0.73	0.35
Insulating Sleeve	-	-	-
Chills	-	-	-
Exothermic Powder	-	-	-
Degassing	Y	1.23	1.31
Filler	-	-	-
Slag Powder	Y	1.22	0.69
Heat Treatment	Y	0.91	0.76
Machining	Y	0.91	1.56
Destructive Testing	Y	0.91	0.98
Non-Destructive Testing	-	-	-
Melting Temperature (°C)	1450.00	2.19	0.46

Table 1. (*Continued*).

Attributes	Meta Attributes	Complexity WCA	Complexity AHP
Application	Architecture	2.19	0.62
Quantity	500.00	2.19	0.35
Overall Complexity (Normalize):		40.23	38.28

Table 2. Industrial casting 2.

Attributes	Meta Attributes	Complexity WCA	Complexity AHP
Overall Length (mm)	482.50	2.75	0.51
Overall Height (mm)	172.00	2.75	0.22
Overall Width (mm)	162.00	4.13	0.09
Average Thickness (mm)	20.00	2.75	0.29
Surface Characteristics	F	5.50	9.38
Number of Holes	6.00	0.14	0.03
Maximum Length of Hole (mm)	25.00	0.69	0.03
Maximum Diameter of Hole (mm)	20.05	0.69	0.22
Contour of Hole (Circular, Square)	C	0.34	0.11
Open to Surface (Flat, Curvature))	F	0.34	0.14
Type of Hole (Through, Blind)	T	0.34	0.20
Number of Slots	2.00	0.21	0.06
Maximum Length of Slot (mm)	47.00	0.69	0.09
Maximum Width of Slot (mm)	4.00	1.03	0.32
Maximum Depth of Slot (mm)	3.00	1.03	0.15
Number of Grooves	-	-	-
Maximum Length of Groove (mm)	-	-	-
Maximum Width of Groove (mm)	-	-	-
Maximum Depth of Groove (mm)	-	-	-
Number of Fillets	1.00	0.41	0.09
Maximum Radius of Fillet (mm)	2.00	2.06	0.19
Number of Chamfers	-	-	-
Chamfer Angle (degree)	-	-	-
Distance (mm)	-	-	-
Number of Hollow Regions	-	-	-

Table 2. (*Continued*).

Attributes	Meta Attributes	Complexity WCA	Complexity AHP
Maximum Length of Hollow Region (mm)	-	-	-
Maximum Diameter of Hollow Region (mm)	-	-	-
Number of Ribs	-	-	-
Maximum Length of Rib (mm)	-	-	-
Maximum Thickness of Rib (mm)	-	-	-
Maximum Width of Rib (mm)	-	-	-
Number of Bosses	-	-	-
Maximum Diameter of Boss (mm)	-	-	-
Maximum Thickness of Boss (mm)	-	-	-
Alloying Elements	11.00	2.94	0.41
Hardness (HRC)	10.00	0.73	0.39
Relative Density (gm/cm^3)	7.80	0.73	0.36
Insulating Sleeve	Y	1.23	1.09
Chills	-	-	-
Exothermic Powder	Y	1.22	0.73
Degassing	Y	1.23	1.31
Filler	Y	1.22	1.64
Slag Powder	Y	1.22	0.69
Heat Treatment	Y	0.92	0.76
Machining	Y	0.92	1.57
Destructive Testing	Y	0.92	0.99
Non-Destructive Testing	Y	0.92	1.16
Melting Temperature (°C)	1460.00	2.20	0.46
Application	Automobile	0.73	0.32
Quantity	1500.00	3.66	0.46
Overall Complexity (Normalize):		43.02	35.53

Table 3. Industrial casting 3.

Attributes	Meta Attributes	Complexity WCA	Complexity AHP
Overall Length (mm)	35.52	4.13	0.31
Overall Height (mm)	170.00	2.75	0.22
Overall Width (mm)	10.50	4.13	0.24
Average Thickness (mm)	10.50	4.13	1.04
Surface Characteristics	F	5.50	9.38
Number of Holes	-	-	-
Maximum Length of Hole (mm)	-	-	-
Maximum Diameter of Hole (mm)	-	-	-
Contour of Hole (Circular, Square)	-	-	-
Open to Surface (Flat, Curvature))	-	-	-
Type of Hole (Through, Blind)	-	-	-
Number of Slots	8.00	0.41	0.08
Maximum Length of Slot (mm)	108.96	1.03	0.11
Maximum Width of Slot (mm)	1.00	1.03	0.32
Maximum Depth of Slot (mm)	1.00	1.03	0.15
Number of Grooves	-	-	-
Maximum Length of Groove (mm)	-	-	-
Maximum Width of Groove (mm)	-	-	-
Maximum Depth of Groove (mm)	-	-	-
Number of Fillets	6.00	0.82	0.09
Maximum Radius of Fillet (mm)	1.00	2.06	0.19
Number of Chamfers	-	-	-
Chamfer Angle (degree)	-	-	-
Distance (mm)	-	-	-
Number of Hollow Regions	-	-	-
Maximum Length of Hollow Region (mm)	-	-	-
Maximum Diameter of Hollow Region (mm)	-	-	-
Number of Ribs	-	-	-
Maximum Length of Rib (mm)	-	-	-
Maximum Thickness of Rib (mm)	-	-	-
Maximum Width of Rib (mm)	-	-	-
Number of Bosses	-	-	-
Maximum Diameter of Boss (mm)	-	-	-
Maximum Thickness of Boss (mm)	-	-	-
Alloying Elements	8.00	2.20	0.37
Hardness (HRC)	37.00	1.47	0.44

Table 3. (*Continued*).

Attributes	Meta Attributes	Complexity WCA	Complexity AHP
Relative Density (gm/cm^3)	7.80	0.73	0.36
Insulating Sleeve	-	-	-
Chills	-	-	-
Exothermic Powder	Y	1.22	0.73
Degassing	Y	1.23	1.31
Filler	-	-	-
Slag Powder	Y	1.22	0.69
Heat Treatment	Y	0.92	0.76
Machining	-	-	-
Destructive Testing	Y	0.92	0.99
Non-Destructive Testing	Y	0.92	1.16
Melting Temperature (°C)	1600.00	2.93	0.54
Application	Biomedical	3.66	2.00
Quantity	100.00	0.73	0.39
Overall Complexity (Normalize):		41.00	28.01

Table 4. Industrial casting 4.

Attributes	Meta Attributes	Complexity WCA	Complexity AHP
Overall Length (mm)	122.20	2.75	0.31
Overall Height (mm)	71.00	2.75	0.17
Overall Width (mm)	122.20	2.75	0.09
Average Thickness (mm)	5.50	4.13	1.04
Surface Characteristics	C	5.50	12.29
Number of Holes	1.00	0.14	0.03
Maximum Length of Hole (mm)	25.50	0.69	0.03
Maximum Diameter of Hole (mm)	33.00	0.46	0.22
Contour of Hole (Circular, Square)	C	0.34	0.11
Open to Surface (Flat, Curvature))	F	0.34	0.14
Type of Hole (Through, Blind)	T	0.34	0.20
Number of Slots	12.00	0.62	0.08

Table 4. (*Continued*).

Attributes	Meta Attributes	Complexity WCA	Complexity AHP
Maximum Length of Slot (mm)	6.00	1.03	0.09
Maximum Width of Slot (mm)	25.00	1.03	0.10
Maximum Depth of Slot (mm)	7.32	0.69	0.15
Number of Grooves	1.00	0.21	0.09
Maximum Length of Groove (mm)	110.00	0.69	0.21
Maximum Width of Groove (mm)	13.84	0.34	0.28
Maximum Depth of Groove (mm)	5.63	1.03	0.33
Number of Fillets	19.00	1.65	0.12
Maximum Radius of Fillet (mm)	4.00	2.06	0.12
Number of Chamfers	-	-	-
Chamfer Angle (degree)	-	-	-
Distance (mm)	-	-	-
Number of Hollow Regions	-	-	-
Maximum Length of Hollow Region (mm)	-	-	-
Maximum Diameter of Hollow Region (mm)	-	-	-
Number of Ribs	-	-	-
Maximum Length of Rib (mm)	-	-	-
Maximum Thickness of Rib (mm)	-	-	-
Maximum Width of Rib (mm)	-	-	-
Number of Bosses	1.00	0.28	0.06
Maximum Diameter of Boss (mm)	45.19	1.38	0.04
Maximum Thickness of Boss (mm)	6.09	0.92	0.13
Alloying Elements	10.00	2.94	0.37
Hardness (HRC)	22.00	1.47	0.44
Relative Density (gm/cm^3)	7.90	0.73	0.36
Insulating Sleeve	Y	1.23	1.09
Chills	-	-	-
Exothermic Powder	Y	1.22	0.73
Degassing	Y	1.23	1.31
Filler	-	-	-
Slag Powder	Y	1.22	0.69
Heat Treatment	Y	0.92	0.76
Machining	Y	0.92	1.57
Destructive Testing	Y	0.92	0.99
Non-Destructive Testing	Y	0.92	1.16
Melting Temperature (°C)	1450.00	2.20	0.46

Table 4. (*Continued*).

Attributes	Meta Attributes	Complexity WCA	Complexity AHP
Application	Chemical	1.46	0.41
Quantity	1000.00	3.66	0.46
Overall Complexity (Normalize):		51.98	43.52

Table 5. Industrial casting 5.

Attributes	Meta Attributes	Complexity WCA	Complexity AHP
Overall Length (mm)	385.19	2.75	0.27
Overall Height (mm)	222.00	4.12	0.22
Overall Width (mm)	222.00	4.12	0.12
Average Thickness (mm)	17.42	2.75	0.28
Surface Characteristics	F	5.50	9.37
Number of Holes	9.00	0.13	0.04
Maximum Length of Hole (mm)	340.19	0.68	0.30
Maximum Diameter of Hole (mm)	45.00	0.23	0.22
Contour of Hole (Circular, Square)	C	0.34	0.10
Open to Surface (Flat, Curvature))	F	0.34	0.14
Type of Hole (Through, Blind)	T	0.34	0.19
Number of Slots	-	-	-
Maximum Length of Slot (mm)	-	-	-
Maximum Width of Slot (mm)	-	-	-
Maximum Depth of Slot (mm)	-	-	-
Number of Grooves	-	-	-
Maximum Length of Groove (mm)	-	-	-
Maximum Width of Groove (mm)	-	-	-
Maximum Depth of Groove (mm)	-	-	-
Number of Fillets	5.00	0.41	0.09
Maximum Radius of Fillet (mm)	15.00	0.68	0.07
Number of Chamfers	-	-	-
Chamfer Angle (degree)	-	-	-
Distance (mm)	-	-	-

Table 5. (*Continued*).

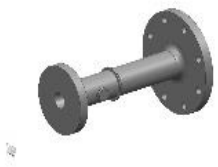

Attributes	Meta Attributes	Complexity WCA	Complexity AHP
Number of Hollow Regions	-	-	-
Maximum Length of Hollow Region (mm)	-	-	-
Maximum Diameter of Hollow Region (mm)	-	-	-
Number of Ribs	-	-	-
Maximum Length of Rib (mm)	-	-	-
Maximum Thickness of Rib (mm)	-	-	-
Maximum Width of Rib (mm)	-	-	-
Number of Bosses	1.00	0.27	0.05
Maximum Diameter of Boss (mm)	33.00	1.37	0.04
Maximum Thickness of Boss (mm)	42.95	1.37	0.19
Alloying Elements	9.00	2.20	0.36
Hardness (HRC)	18.00	0.73	0.39
Relative Density (gm/cm^3)	7.90	0.73	0.35
Insulating Sleeve	-	-	-
Chills	-	-	-
Exothermic Powder	-	-	-
Degassing	-	-	-
Filler	-	-	-
Slag Powder	-	-	-
Heat Treatment	-	-	-
Machining	Y	0.91	1.56
Destructive Testing	Y	0.91	0.98
Non-Destructive Testing	-	-	-
Melting Temperature (°C)	1450.00	2.19	0.46
Application	Machine tool	0.73	0.31
Quantity	500.00	2.19	0.35
Overall Complexity (Normalize):		28.49	12.62

4. Discussion

The analysis of the complexity index for various industrial castings reveals that complexity is primarily affect by required features and manufacturability. Additionally, it is observed that simple geometric castings exhibit higher complexity using WCA compared to AHP due to equal importance assigned to all parameters in WCA. It was observed that addressing criteria related to feature and manufacturability presents significant challenges leading to increased complexity in the investment casting process.

Moreover, the complexity index is further divided into five categories: Low (0–20), Medium (21–40), High (41–60), Very High (61–80), and Extremely High (81–100). These categories establish a connection between the complexity value and manufacturing cost. In the computation of the complexity index for various use cases, it was noted that the complexity of industrial castings varied from 28 to 52 using WCA and while using AHP complexity varied from 12 to 43 falling within the low, medium and high categories. This correlation proves advantageous for cost estimation where castings exhibit very closed complexity values. The categorization of the presented use cases is illustrated in the **Figures 2–6**.

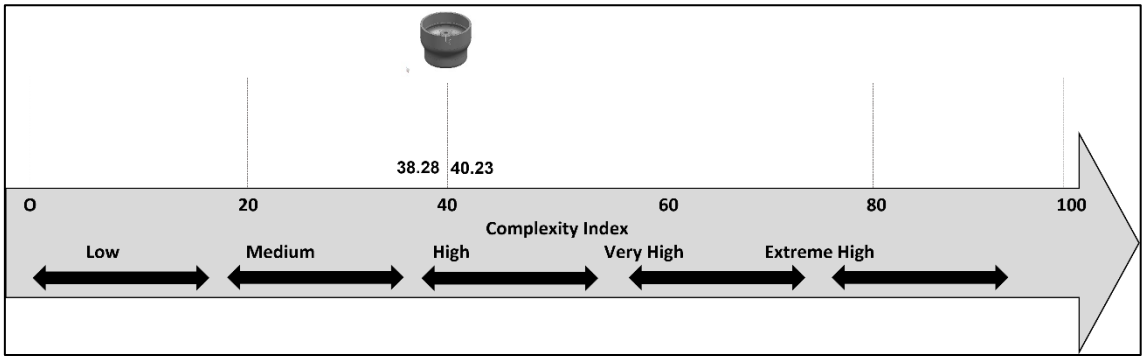

Figure 2. Categorization of industrial casting 01.

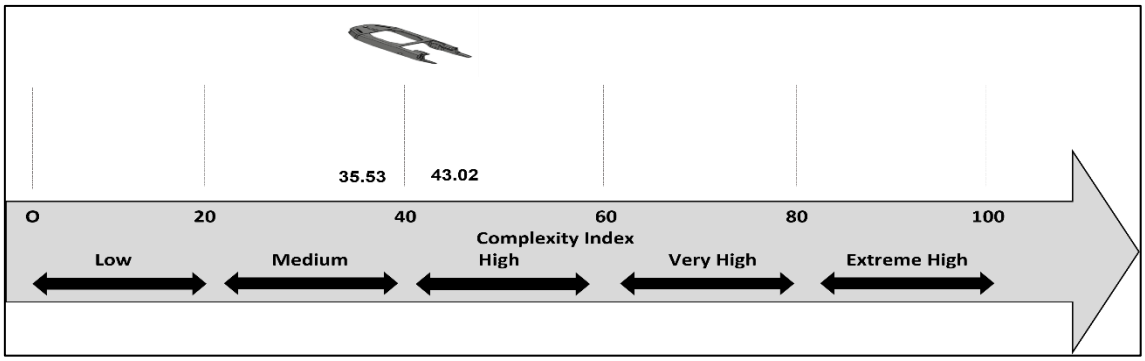

Figure 3. Categorization of industrial casting 02.

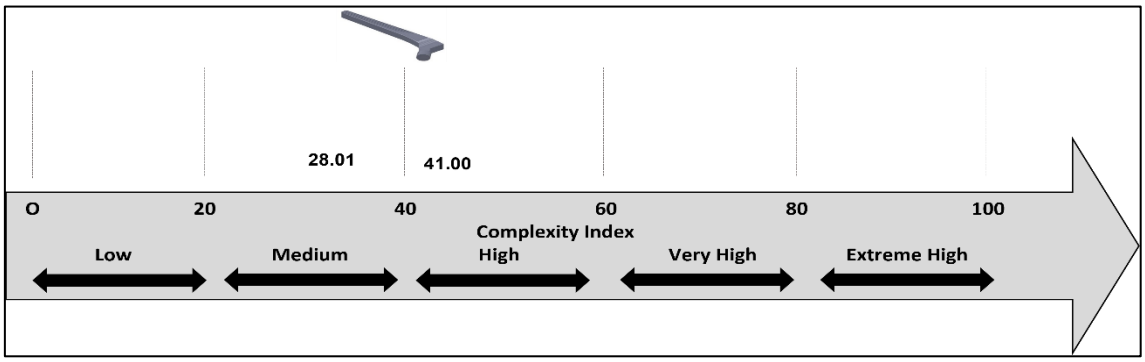

Figure 4. Categorization of industrial casting 03.

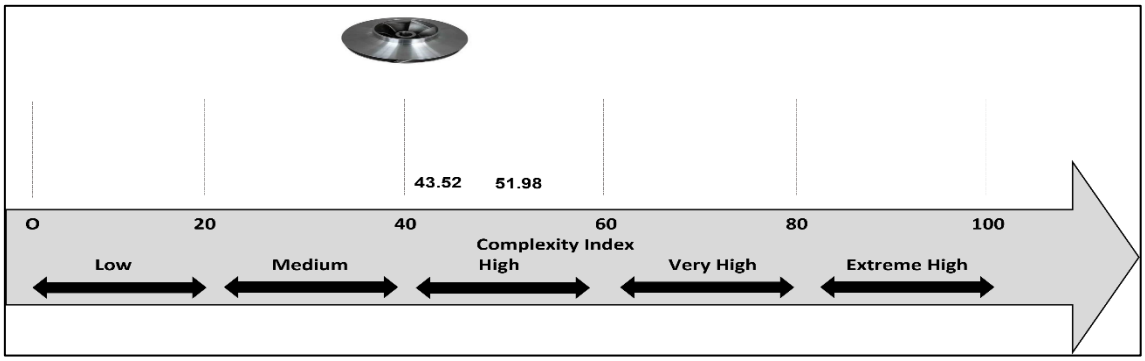

Figure 5. Categorization of industrial casting 04.

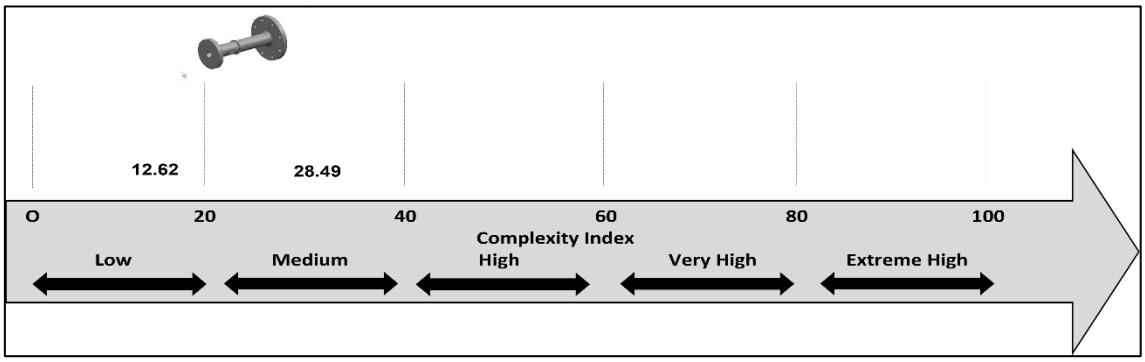

Figure 6. Categorization of industrial casting 05.

5. Conclusions

Investment casting process is a widely familiar process for manufacturing intricate industrial castings with high surface quality and tight dimensional tolerances. Selecting the investment casting process for manufacturing specific castings generally involves a comprehensive approach that qualitatively assesses various parameters of each casting. However, inaccurate decisions in this selection can lead to unnecessary resource and energy consumption, longer lead times and decreased productivity.

In this paper, implementation of MCDM methods for computing complexity involved in investment casting has been presented. More than 5 use cases were demonstrated to assess the complexity of industrial investment castings. The findings revealed that these castings exhibit complexities ranging from 28 to 52 using WCA and while using AHP complexity varied from 12 to 43. This index offers designers a more comprehensive understanding of the influence of individual parameters (such as geometry and features) on the overall complexity index. Additionally, this approach plays an important role in predicting early-stage critical parameters and helps in making informed decisions about employing process.

Author contributions: Conceptualization, AS and NM; methodology, AS; software, AS and NM; validation, NM and AS; resources, NM; writing—original draft preparation, NM and AS; writing—review and editing, NM; visualization, AS; supervision, AS. All authors have read and agreed to the published version of the manuscript.

Conflict of interest: The authors declare no conflict of interest.

References

1. Kerbrat O, Mognol P, Hascoet JY. Manufacturing complexity evaluation at the design stage for both machining and layered manufacturing. CIRP Journal of Manufacturing Science and Technology. 2010; 2(3): 208-215. doi: 10.1016/j.cirpj.2010.03.007
2. Merkt S, Hinke C, Schleifenbaum H, et al. Geometric complexity analysis in an integrative technology evaluation model (item) for selective laser melting (SLM)#. The South African Journal of Industrial Engineering. 2011; 23(2). doi: 10.7166/23-2-333
3. Conner BP, Manogharan GP, Martof AN, et al. Making sense of 3-D printing: Creating a map of additive manufacturing products and services. Additive Manufacturing. 2014; 1–4: 64-76. doi: 10.1016/j.addma.2014.08.005
4. Hosseini-Ara R, Yavari P. A new criterion for preform design of H-shaped hot die forging based on shape complexity factor. International Journal of Material Forming. 2017; 11(2): 233-238. doi: 10.1007/s12289-017-1345-8
5. Pradel P, Bibb R, Zhu Z et al. Exploring the Impact of Shape Complexity on Build Time for Material Extrusion and Material Jetting. Springer International Publishing; 2018. pp. 24-33.
6. Qamar SZ, Chekotu JC, Al-Maharbi M, et al. Shape Complexity in Metal Extrusion: Definitions, Classification, and Applications. Arabian Journal for Science and Engineering. 2019; 44(9): 7371-7384. doi: 10.1007/s13369-019-03886-8
7. Qamar SZ, Chekotu JC, Qamar SB. Effect of Shape Complexity on Ram Pressure and Metal Flow in Aluminum Extrusion. JOM. 2019; 71(12): 4378-4392. doi: 10.1007/s11837-019-03748-6
8. Joshi D, Ravi B. Quantifying the Shape Complexity of Cast Parts. Computer-Aided Design and Applications. 2010; 7(5): 685-700. doi: 10.3722/cadaps.2010.685-700
9. Martof A, Gullapalli R, Kelly J, et al. Economies of complexity of 3D printed sand molds for casting. ResearchGate; 2018. pp. 117-134.
10. Zavadskas EK, Turskis Z, Kildiene S. State of art surveys of overviews on MCDM/MADM methods. Technological and Economic Development of Economy. 2014; 20(1): 165-179. doi: 10.3846/20294913.2014.892037
11. Toloie-eshlaghy A. MCDM Methodologies and Applications: A Literature Review from 1999 to 2009. Research Journal of Internatıonal Studıes. 2011; 21(21): 86-137.
12. Saaty TL. How to make a decision: The analytic hierarchy process. Eur J Oper Res. 1990; 48(1): 9-26. doi: 10.1016/0377-2217(90)90057-I
13. Pal DK, Ravi B, Bhargava LS. Rapid tooling route selection for metal casting using QFD–ANP methodology. International Journal of Computer Integrated Manufacturing. 2007; 20(4): 338-354. doi: 10.1080/09511920600883229
14. Singh C, Singh D, Khamba JS. Analyzing barriers of Green Lean practices in manufacturing industries by DEMATEL approach. Journal of Manufacturing Technology Management. 2020; 32(1): 176-198. doi: 10.1108/jmtm-02-2020-0053
15. Che Hassan MF, Mohd Rosli MU, Mohd Redzuan MA. Material selection in a sustainable manufacturing practice of a badminton racket frame using Elimination and Choice Expressing Reality (ELECTRE) Method. Journal of Physics: Conference Series. 2018; 1020(1): 012012. doi: 10.1088/1742-6596/1020/1/012012
16. Athawale VM, Chatterjee P, Chakraborty S. Decision making for facility location selection using PROMETHEE II method. International Journal of Industrial and Systems Engineering. 2012; 11(1/2): 16. doi: 10.1504/ijise.2012.046652
17. Chodha V, Dubey R, Kumar R, et al. Selection of industrial arc welding robot with TOPSIS and Entropy MCDM techniques. Materials Today: Proceedings. 2022; 50: 709-715. doi: 10.1016/j.matpr.2021.04.487
18. Ibrahim A, Surya RA. The Implementation of Simple Additive Weighting (SAW) Method in Decision Support System for the Best School Selection in Jambi. Journal of Physics: Conference Series. 2019; 1338(1): 012054. doi: 10.1088/1742-6596/1338/1/012054
19. Dev S, Aherwar A, Patnaik A. Material Selection for Automotive Piston Component Using Entropy-VIKOR Method. Silicon. 2019; 12(1): 155-169. doi: 10.1007/s12633-019-00110-y
20. Durán O, Aguilo J. Computer-aided machine-tool selection based on a Fuzzy-AHP approach. Expert Systems with Applications. 2008; 34(3): 1787-1794. doi: 10.1016/j.eswa.2007.01.046
21. Pelissari R, Khan SA, Ben-Amor S. Application of Multi-Criteria Decision-Making Methods in Sustainable Manufacturing Management: A Systematic Literature Review and Analysis of the Prospects. International Journal of Information Technology & Decision Making. 2021; 21(02): 493-515. doi: 10.1142/s0219622021300020

22. Karthik S, Chung CW, Ramani K, et al. Methodology for Metalcasting Process Selection. SAE Technical Paper Series; 2003.
23. Mustafa A, Abdollah MFB, Shuhimi FF, et al. Selection and verification of kenaf fibres as an alternative friction material using Weighted Decision Matrix method. Materials & Design. 2015; 67: 577-582. doi: 10.1016/j.matdes.2014.10.091
24. Anjum Mohd, Haque MdA, Ahmad N. Analysis and Ranking of Software Reliability Models Based on Weighted Criteria Value. International Journal of Information Technology and Computer Science. 2013; 5(2): 1-14. doi: 10.5815/ijitcs.2013.02.01
25. Akarte MM, RaviB. Casting Process Selection using AHP and Fuzzy Logic. International Seminar on Manufacturing Technology Beyond. 2000; 1: 1-10.
26. Chougule RG, Ravi B. Variant process planning of castings using AHP-based nearest neighbour algorithm for case retrieval. International Journal of Production Research. 2005; 43(6): 1255-1273. doi: 10.1080/00207540412331320517
27. Joshi D, Ravi B. Early castability evaluation using analytical hierarchy process. The International Journal of Advanced Manufacturing Technology. 2010; 50(1-4): 21-36. doi: 10.1007/s00170-010-2517-6
28. Sata AV, Maheta NR. 5 Cs of Investment Casting Foundries in Rajkot Cluster – An Industrial Survey. Archives of Foundry Engineering. Published online September 8, 2021: 102-108. doi: 10.24425/afe.2021.138672
29. Maheta N, Sata DA. Systematic Development of Cumulative Complexity Index for Investment Casting. Journal of Advanced Manufacturing Systems. 2022; 22(02): 323-338. doi: 10.1142/s0219686723500166
30. Maheta N, Sata A. Development of a Novel Complexity Index for Investment Casting. International Journal of Metalcasting. 2023; 18(3): 2165-2180. doi: 10.1007/s40962-023-01151-1

Mechanical Engineering Advances 2025, 3(1), 2469.
https://doi.org/10.59400/mea2469

Article

Deep neural network enhanced modeling and adaptive control of a malfunctional spacecraft under unknown accessory breakage

Krzysztof Zalewski[1,*], Aliaksei Zakrevsky[2], Mikko Virtanen[3], Johan Svensson[4], Anders Joe[5], James Wilson[6]

[1] Warsaw University of Technology, 00-661 Warsaw, Poland
[2] Belarusian National Technical University, 220013 Minsk, Belarus
[3] Aalto University, 02150 Espoo, Finland
[4] KTH Royal Institute of Technology, 114 28 Stockholm, Sweden
[5] Norwegian University of Science and Technology, 2802 Gjøvik, Norway
[6] University of Bristol, Bristol BS8 1TH, UK
*** Corresponding author:** Krzysztof Zalewski, krzyz77@bsu.edu.pl

CITATION

Zalewski K, Zakrevsky A, Virtanen M, et al. Deep neural network enhanced modeling and adaptive control of a malfunctional spacecraft under unknown accessory breakage. Mechanical Engineering Advances. 2025; 3(1): 2469. https://doi.org/10.59400/mea2469

ARTICLE INFO

Received: 30 December 2024
Accepted: 17 January 2025
Available online: 26 January 2025

Abstract: This manuscript presents a sophisticated deep neural networks (DNNs)-driven adaptive control paradigm for concurrently regulating the attitude and suppressing structural oscillations of a flexible spacecraft in a fully three-dimensional domain. By leveraging Hamilton's principle, the spacecraft's motion is formulated as an infinite-dimensional dynamic model described by partial differential equations, capturing the subtle interactions between rigid-body rotational maneuvers and flexible panel deformations. In contrast to traditional schemes, the proposed control methodology integrates a DNNs module to compensate for uncertain actuator anomalies and external input disturbances in real time, thereby ensuring fault tolerance under arbitrary, potentially unbounded actuator malfunctions. A rigorously constructed Lyapunov-based stability analysis corroborates that the system's energy, angular rates, and transverse deflections remain uniformly bounded and asymptotically converge to zero, even in the face of multiple actuator failures. This theoretical guarantee stems from the synergistic interplay between the network's representational power and the adaptive control law's robust learning capabilities. Extensive computational experiments demonstrate the efficacy of the developed framework in orchestrating high-precision attitude stabilization while simultaneously mitigating detrimental vibrations, showcasing the superior performance and resiliency of the proposed DNNs-infused control architecture.

Keywords: deep learning; neural network; aerospace robot; adaptive control

1. Introduction

Flexible spacecraft have garnered substantial attention in recent years, primarily due to their advantageous attributes of diminished mass and reduced power requirements. By enabling increased functionality at lower launch costs, these pliable structures concurrently engender intricate coupling phenomena between elastic deflections and overall attitude maneuvers [1–3]. Such couplings inevitably compromise the performance of the spacecraft if not carefully mitigated through control strategies. Early efforts aimed at preserving attitude precision and alleviating unwanted vibrations often relied on truncation-based approximations of the flexible dynamics, which can introduce spillover effects and even precipitate instability. Consequently, to accurately capture the salient characteristics of both the spacecraft's rigid-body dynamics and its structural deformations, an infinite-dimensional representation governed by coupled partial differential equations (PDEs) and ordinary differential equations (ODEs) has emerged as a more rigorous modeling paradigm.

Historically, significant strides have been made in controlling flexible structures formulated within infinite-dimensional frameworks. Various schemes have targeted heat equations, beam equations, and string equations to demonstrate sophisticated methods for boundary or distributed control. In the context of flexible spacecraft specifically, the ubiquitous Euler–Bernoulli beam model has frequently been adopted to describe cantilever-like appendages attached to a central rigid hub. In Zhang et al. [4], the authors provide an innovative approach, as it highlights the efficacy of deep neural networks in optimizing coordination strategies for multi-aerospace systems during complex tasks. Their findings align with and further underscore the importance of leveraging DNNs in enhancing adaptability and robustness under uncertain conditions. The antecedent studies established foundational techniques—ranging from disturbance observers to fault-tolerant switches—for mitigating vibrational effects, many focused on two-dimensional (2D) or simplified geometric settings that do not adequately reflect the more complex three-dimensional (3D) coupling behaviors [5]. Several investigations into 3D beam-like systems have illustrated the significance of multiple deflection axes and their strong interactions with the spacecraft's rotational degrees of freedom, thereby highlighting the necessity for more nuanced control designs. Furthermore, most extant works operate under the assumption of perfectly functioning actuators, overlooking the real-world possibility of actuator malfunctions or failures.

In practical scenarios, actuators can degrade due to phenomena such as aging, abrasion, or manufacturing imperfections, resulting in partial losses of effectiveness or complete failures that can occur unpredictably over the spacecraft's operational lifespan. Ensuring the reliability of flexible spacecraft under these adverse conditions demands robust and fault-tolerant approaches that address potential infinite sets of unknown failures. Traditional control strategies (e.g., robust, sliding mode, or classical adaptive control) have demonstrated some efficacy, yet they often presume limited failure scenarios or rely on truncation-based models that may overlook higher-order dynamics of the flexible appendages. Gao et al. [6] develop a novel adaptive decentralized control framework for multi-robot servicing tasks in space environments, addressing both civilian applications, such as extending spacecraft operational lifespans (e.g., SpaceX initiatives), and military aerospace operations, where robust handling of uncertain dynamics and system malfunctions is critical for mission success in unpredictable environments. Consequently, guaranteeing asymptotic stability in the presence of unbounded actuator anomalies remains nontrivial, particularly when dealing with PDE-based representations [7–10].

In parallel, deep neural networks (DNNs) have emerged as powerful universal function approximators with strong capacity to adapt to highly nonlinear and uncertain systems [11]. Their integration with adaptive control laws offers a promising avenue for augmenting the robustness and adaptability of fault-tolerant strategies. By harnessing DNNs within a PDE-based framework, one can dynamically learn the evolving actuator efficacy and external disturbance profiles, thereby compensating for unknown anomalies more effectively than classical methods. This synergy of DNN-based estimation and adaptive boundary control allows real-time adjustments to the feedback law, accommodating an unbounded number of actuator faults across a potentially infinite time horizon.

The primary objective of this study is to devise a sophisticated DNNs-infused adaptive control methodology that simultaneously stabilizes the spacecraft's attitude and suppresses the structural vibrations of its flexible panels in a fully three-dimensional configuration. To achieve this, we adopt an extended Hamilton principle for modeling the overall system with coupled PDE–ODE dynamics, ensuring a comprehensive representation of both rigid-body motions and elastic deformations. The control strategy incorporates DNN modules to estimate and compensate for actuator anomalies of arbitrary complexity, while an adaptive boundary control scheme ensures robust command authority over the PDE-governed vibrations. A Lyapunov-based analysis is conducted to prove that the system energies, rotational velocities, and deformation trajectories remain uniformly bounded and converge asymptotically, even amid uncountably many actuator failures [12–15].

The remainder of this paper is organized as follows. First, the governing equations for a spatially flexible spacecraft are formulated, emphasizing the coupling between the rigid hub's attitude states and the PDE-driven flexible panels [16]. Subsequently, the DNNs-augmented fault-tolerant control scheme and accompanying parameter update laws are introduced. A rigorous Lyapunov analysis then validates the boundedness and decay properties of the closed-loop system [17–20]. Numerical simulations corroborate the efficacy and resilience of the proposed approach, and final conclusions are drawn regarding future directions and broader implications of this research.

Space exploration missions are increasingly reliant on flexible spacecraft due to their lightweight designs, reduced launch costs, and ability to carry advanced instrumentation. However, these advantages come with significant challenges. The interaction between structural deformations and attitude dynamics can lead to performance degradation, particularly under unforeseen conditions like actuator malfunctions. While traditional control strategies provide partial solutions, they often fail to address the complexities introduced by unbounded uncertainties, actuator degradation, or external disturbances. This work is motivated by the critical need to ensure reliability and precision in demanding operational environments, such as satellite repair and orbital debris management, where failures could jeopardize mission success and incur significant financial and operational costs. By integrating deep learning and adaptive control, this study aims to establish a robust, fault-tolerant control framework capable of addressing these multifaceted challenges, paving the way for safer and more efficient space missions.

2. Problem statement

We investigate a flexible aerospace apparatus composed of a rigid core and a slender, compliant panel, consistent with the illustrative schematics in **Figures 1** and **2**. In its undeformed configuration, the flexible panel is oriented along the $\Omega\Xi_\beta$ axis and assumed inextensible, permitting solely transverse deflections in the Υ_β and Υ_β directions. Denote these deflections by $\chi(\phi,\tau)$ and $\zeta(\phi,\tau)$, where ϕ and τ represent the spatial and temporal coordinates, respectively. Hence, the instantaneous position of any point $\mathcal{P}$ on the panel may be written as

$$\varrho = [\phi, \chi, \zeta]^\top,$$

where ϕ is the distance measured from the origin Ω.

The angular velocities of the body frame relative to the orbital frame are collected in

$$\lambda = [\lambda_1, \lambda_2, \lambda_3]^\top,$$

while the attitude of the flexible aerospace system is parameterized by Euler angles

$$\alpha = [\alpha_1, \alpha_2, \alpha_3]^\top,$$

where indicating successive rotations about the $\Xi_\beta, \Upsilon_\beta$, and $\mathcal{Z}_\beta$ axes.

Given that actuators may deteriorate or abruptly malfunction during prolonged operation, a robust fault-mitigation strategy is imperative. To address this, the present study proposes a DNNs-augmented adaptive control methodology capable of reconciling structural dynamics and attitude requirements under uncertain actuator conditions [21]. By embedding a neural approximator based on the research work in Zhang et al. [22] into the PDE-based framework of the slender panel's deformations, the controller can dynamically estimate and compensate for unknown parameters, actuator losses, and external disturbances. This synergy between deep learning and adaptive control ensures reliable real-time corrections [23], facilitating both vibration suppression and precise angular stabilization in the presence of potentially unbounded actuator anomalies across the spacecraft's lifespan [24–27].

Figure 1. One spacecraft using one robot arm to pick up the broken part from one malfunctioning aerospace device in a space environment.

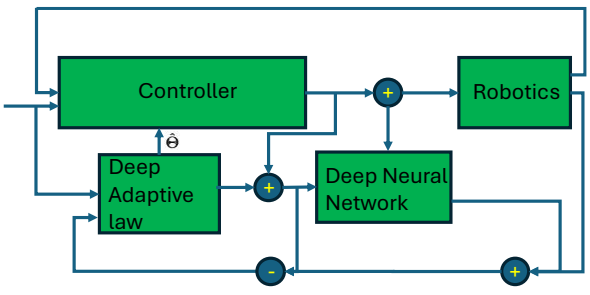

Figure 2. Block diagram of our deep adaptive control algorithm.

3. Methodology

In this section, we develop a deep neural network–augmented adaptive control

strategy for a malfunctioning aerospace vehicle whose dynamics are modeled by coupled partial differential equations (PDEs) and ordinary differential equations (ODEs). The overarching goal is to stabilize both the angular motion of the rigid hub and the transverse deflections of the flexible panel, even under adverse actuator anomalies. By integrating a neural approximator within the control law, the scheme can dynamically learn and counteract model uncertainties and time-varying disturbances, thereby ensuring robust performance.

3.1. Dynamics analysis of repairing robotics

A robust grasp of the intrinsic physics and mechanical characteristics of industrial robots is essential for model-based identification. Under the Lagrangian formalism, the inverse dynamics of a fully actuated nnn-link robot manipulator can be succinctly written as

$$\tau = M(q)\ddot{q} + C(q,\dot{q}) + D$$

where $\tau \in \mathbb{R}^{n\times 1}$ represents the joint torques, $q, \dot{q}, \ddot{q} \in \mathbb{R}^{n\times 1}$ denote the vectors of joint angles, angular velocities, and angular accelerations, respectively. The matrix $M(q) \in \mathbb{R}^{n\times n}$ is the inertia matrix of the manipulator, $C(q,\dot{q})$ captures the Coriolis, centripetal, and D encapsulates deterministic disturbances such as sensor drift or unmodeled dynamics.

3.2. Governing equations via Hamilton's principle

To capture the essential rigid-body and flexible-panel interactions, we start by applying Hamilton's principle to the kinetic and potential energies of the system. Let Γ_f denote the positive-definite inertia tensor of the rigid body, and let $\Upsilon \in \mathbb{R}^3$ represent the angular velocity of the hub relative to an inertial (orbital) frame. Suppose further that Σ is the linear mass density of the flexible appendage, while κ is its damping coefficient. Denoting by $\varphi(\ell, \tau)$ and $\xi(\ell, \tau)$ the small deflections of the panel in two orthogonal directions, with $\ell \in [0, L]$ as the spatial coordinate and τ the temporal variable, one obtains:

$$\Gamma_f \dot{\Upsilon} + \Upsilon \times \left(\Gamma_f \Upsilon\right) + \Omega = \Theta + \Delta,$$
$$\Sigma \begin{bmatrix} \varphi_{\tau\tau}(\ell,\tau) \\ \xi_{\tau\tau}(\ell,\tau) \end{bmatrix} + \kappa \begin{bmatrix} \varphi_{\tau}(\ell,\tau) \\ \xi_{\tau}(\ell,\tau) \end{bmatrix} + \mathcal{F}(\Upsilon, \varphi, \xi) = 0,$$

where Ω encapsulates nonlinear terms that may arise from gyroscopic and Coriolis-like effects, Θ is the external torque acting on the rigid hub, Δ represents cumulative disturbances or actuator faults, and $\mathcal{F}$ encompasses the higher-order spatial derivatives (e.g., bending stiffness terms) of $\varphi(\ell, \tau)$ and $\xi(\ell, \tau)$. The boundary conditions for the flexible panel typically specify zero transverse displacements and slopes at $\ell = 0$ and free-end conditions at $\ell = L$, although exact formulations may vary depending on the structural configuration:

$$\varphi(0,\tau) = \xi(0,\tau) = 0,$$
$$\varphi_{\ell}(0,\tau) = \xi_{\ell}(0,\tau) = 0,$$
$$\varphi_{\ell\ell}(L,\tau) = \xi_{\ell\ell}(L,\tau) = 0$$

3.3. DNNs based adaptive controller

Actuator failures can manifest unpredictably during extended missions, necessitating a control framework that autonomously recognizes and compensates for partial or complete loss of actuation authority. The key innovation here is to integrate a DNNs module—trained online—as part of an adaptive control law.

Concretely, consider a DNN $\mathcal{N}_\Theta(\times)$ parameterized by weights Θ. At each instant τ, the DNN processes measured signals (e.g., deflections $\varphi(\ell, \tau)$, $\xi(\ell, \tau)$, angular velocities $\Upsilon(\tau)$ and partial estimates of actuator health) and outputs compensatory control adjustments. These outputs feed into an adaptive boundary [28] or distributed controller $\mathcal{C}(\tau)$, which acts on the PDE–ODE system:

$$\Theta(\tau) = -\mathcal{C}(\varphi, \xi, \Upsilon, \dots) - \mathcal{N}_\Theta(\varphi, \xi, \Upsilon, \dots)$$

The neural parameters Θ are continuously updated via an online learning rule (e.g., a backpropagation-through-time variant adapted to PDE constraints), thus minimizing a composite cost functional that penalizes vibration amplitude, tracking errors in the angular motion, and deviations from nominal performance metrics. Mathematically, one might define an instantaneous error signal ε(τ) that encapsulates both attitude- and vibration-related tracking objectives, and then refine Θ using a gradient-based adaptation:

$$\dot{\Theta}(\tau) = -\eta \frac{\partial \varepsilon(\tau)}{\partial \Theta}$$

where η is the learning rate. This iterative scheme allows the controller to "learn" complex fault patterns, even in the presence of an unbounded number of malfunctions throughout the spacecraft's operational timeline.

3.4. Lyapunov stability analysis

To certify the convergence properties of the overall closed-loop system (i.e., the PDE–ODE dynamics combined with the DNN-based adaptive controller), a Lyapunov functional $\mathcal{V}(\tau)$ is devised to incorporate both rigid-body energy terms and flexible energy components as

$$\mathcal{V}(\tau) = \frac{1}{2}\left(\Upsilon^{\mathrm{T}}\Gamma_f\Upsilon\right) + \frac{\Sigma}{2}\int_0^L \left[(\varphi_\tau^2 + \xi_\tau^2) + \beta_1\left(\varphi_\ell^2 + \xi_\ell^2\right) + \beta_2\left(\varphi_{\ell\ell}^2 + \xi_{\ell\ell}^2\right)\right]\mathrm{d}\ell$$

where β_1 and β_2 are positive constants that account for bending stiffness in the panel. By examining the time derivative $\dot{\mathcal{V}}(\tau)$ under the proposed control law, one demonstrates that $\mathcal{V}(\tau)$ remains uniformly bounded and ultimately converges to an arbitrarily small neighborhood around zero—thereby implying that both $\Upsilon(\tau)$ and the deflections $\varphi(\ell, \tau), \xi(\ell, \tau)$ vanish asymptotically. The DNN adaptation ensures that unidentified disturbances and unknown actuator failure profiles are effectively counteracted, preventing divergence of the system states [29–33].

4. Simulation results

To investigate the effectiveness of the proposed deep neural network–augmented adaptive scheme for a malfunctioning aerospace platform, a series of numerical

experiments are performed using a finite-difference approximation of the governing partial differential equations (PDEs). For analytical simplicity, we presume that the satellite's body inertia matrix $\Lambda \in \mathbb{R}^{3\times3}$ is diagonal, reflecting a scenario where cross-coupling inertias are negligible.

To emulate real-world perturbations, constant disturbances $\delta_1(\tau), \delta_2(\tau), \delta_3(\tau)$ are introduced in the spacecraft's torque channels:

$$\delta_1(\tau) = 2\mathfrak{N}, \delta_2(\tau) = 1\mathfrak{N}, \delta_3(\tau) = 6\mathfrak{N},$$

where $\mathfrak{N}$ symbolizes units of Newton–meter (or an equivalent torque measure), and τ denotes time. These constant values facilitate straightforward comparisons with theoretical bounds. The initial angular velocities of the rigid body are specified as

$$\omega_1(0) = 0.02\text{rad/s}, \omega_2(0) = 0.03\text{rad/s}, \omega_3(0) = 0.04\text{rad/s},$$

To replicate the uncertain and possibly abrupt malfunctions common in aerospace actuators, the net torques $\varsigma_1(\tau), \varsigma_2(\tau), \varsigma_3(\tau)$ applied to each rotational axis are decomposed into two parts:

$$\varsigma_1(\tau) = \rho_{1,1}(\tau) + \rho_{1,2}(\tau), \varsigma_2(\tau) = \rho_{2,1}(\tau) + \rho_{2,2}(\tau), \varsigma_3(\tau) = \rho_{3,1}(\tau) + \rho_{3,2}(\tau).$$

Each $\rho_{i,j}(\tau)$ can experience time intervals of diminished effectiveness, complete dropout, or partial gain according to a predefined fault profile. For instance,

$$\rho_{1,1}(\tau) = \begin{cases} 0.3v_{1,1}(\tau), \tau \in [2k, 2k+1), \\ 0.5v_{1,1}(\tau), \tau \in [2k+1, 2k+2) \end{cases}$$

A DNNs-based adaptive law is utilized to compute the correction signals necessary to counteract both the structural vibrations and the actuator degradations. The underlying proportional-derivative (PD) component addresses nominal dynamics as

$$\eta_{i,j}(\tau) = -k_{p_i}\omega_i(\tau) - k_{d_i}\dot{\omega}_i(\tau), i = 1,2,3, j = 1,2$$

where $\omega_i(\tau)$ indicates the i-th rotational rate, and k_{p_i}, k_{d_i} are PD gains. Meanwhile, the neural network $\Xi(\mathrm{x}(\tau); \Theta(\tau))$, parameterized by weights $\Theta(\tau)$ monitors observable states $\mathrm{x}(\tau)$, deflections, or partial actuator diagnostics and outputs an estimated compensation term. The combined control input can be expressed as

$$v_{i,j}(\tau) = \eta_{i,j}(\tau) - \Xi_{i,j}(\mathrm{x}(\tau); \Theta(\tau))$$

Ensuring that any mismatch between the nominal model and real-time behavior—whether due to unmodeled dynamics or actuator failures—is addressed adaptively. An online learning rule updates $\Theta(\tau)$ based on a Lyapunov-like criterion to preserve overall stability.

In **Figure 3**, each panel corresponds to a distinct joint of our space-based robot arm tasked with repairing a malfunctioning aerospace device. The horizontal axis indicates time, while the vertical axis represents the torque generated by each joint's actuator. Multiple curves—namely the reference trajectory, baseline adaptive control, a deep reinforcement strategy (Deep-Q), and our proposed DNNs-enabled adaptive algorithm—are plotted to facilitate a comparative evaluation. From the visual inspection, the reference curve (green) captures the nominal torque profile required

for precise maneuvering. Notably, our approach (pink) aligns closely with the reference track, especially in the presence of sudden torque deviations or partial actuator failures. This behavior underscores the method's ability to learn and adapt quickly to unforeseen anomalies in actuator performance, maintaining near-optimal tracking even when the robot arm must contend with harsh environmental conditions and hardware deterioration.

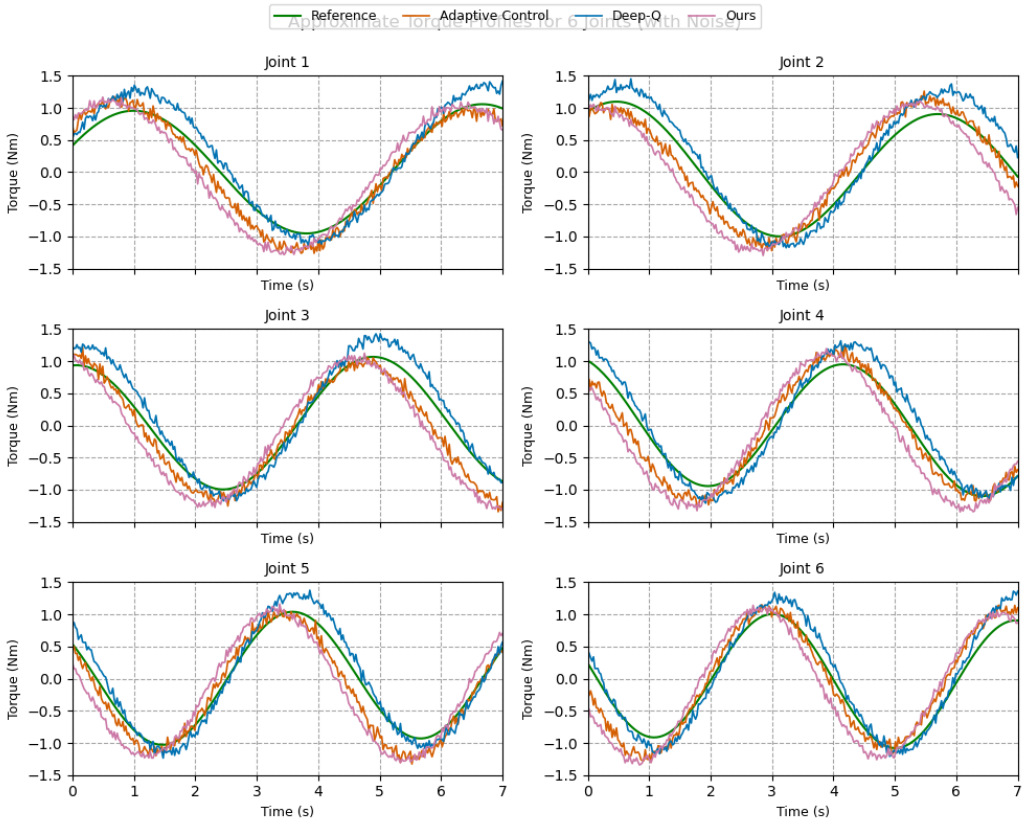

Figure 3. Approximate torque applied from each joint in the robot arm.

A key insight revealed by these torque plots is the robustness of the proposed DNNs-infused controller against abrupt variations in load and unknown system parameters. By integrating real-time learning into the adaptive control loop, the method effectively redistributes control effort across the joints, thereby ensuring smooth operation and stable torque outputs for each actuator. Consequently, the space-borne manipulator can maintain high-precision articulation and mitigate vibrations or oscillations—critical when attempting intricate repair tasks on sensitive aerospace equipment. This combination of real-time adaptation and machine learning–based fault compensation is pivotal to guaranteeing mission success under uncertain conditions in orbit.

Figure 4 shows that the horizontal axes in each subplot indicate the spatial coordinate and time (τ in seconds), whereas the vertical axis denotes the instantaneous deflection magnitude (in feet). By examining the color gradient, one can observe that our proposed DNNs-assisted control strategy effectively suppresses excessive bending or oscillatory modes that might arise when joints experience degraded actuator authority. The near-uniform surfaces in some regions highlight that structural

perturbations are kept to a minimum, ensuring that the manipulator remains stable even as it extends or retracts to access damaged hardware.

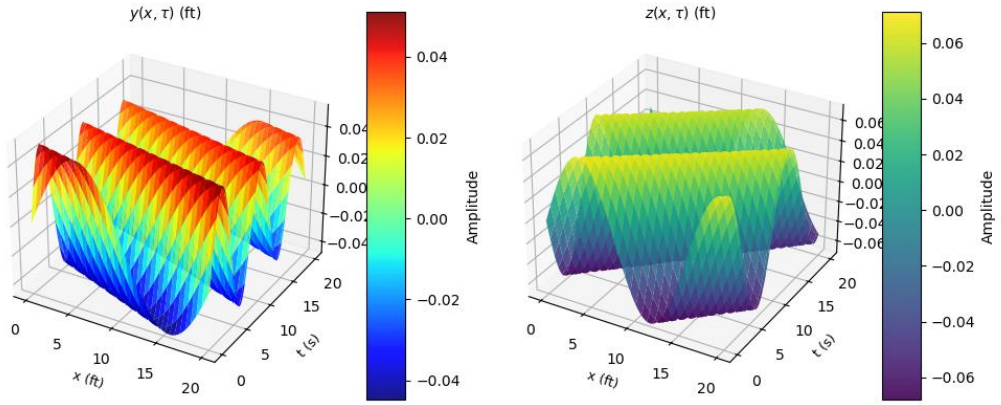

Figure 4. Three-dimensional deflection evolution of the space-based robot arm under DNNs-enhanced adaptive control.

In practical terms, these surfaces confirm that the adaptive controller, augmented with deep learning, successfully anticipates and compensates for uncertain loads, micro-vibrations, and partial failures of actuators distributed along the manipulator's span. The reduction in peak deflections not only fosters a safer operational envelope—minimizing collision risks with neighboring satellite components—but also prolongs the service life of the robot arm by reducing stress on critical joints [34]. Ultimately, this capacity for real-time deflection mitigation is crucial in precision tasks, such as repairing a broken part in orbit, where slight positioning errors might jeopardize the integrity of expensive aerospace assets [35].

5. Conclusions

In this study, we introduced a multifaceted approach that merges physics-based formulations with data-driven refinement to achieve accurate and robust control in the presence of unmodeled nonlinearities. By enriching the conventional observer–based system learning (OSBL) technique with a DNNs model, we obtained an enhanced identification scheme. This novel framework addresses residual modeling discrepancies through an online DNN that effectively captures deviations unaccounted for by classical physics-based models. Subsequently, the identified dynamics were integrated into a deep adaptive control (DAC) architecture, leveraging a model reference paradigm to counteract uncertainties and external noise. The adaptive update laws were systematically derived from Lyapunov-like stability analysis, thereby guaranteeing asymptotic error convergence despite significant disturbances.

Experimental evaluations on a physical six-degree-of-freedom (6-DOF) robotic arm demonstrated both the standard OSBL and least-squares (LS) methods, particularly when confronted with intricate dynamics that are challenging to capture via pure analytical modeling. The observed mismatch between the physical model's torque predictions and the real-world measurements underscores the necessity of a data-driven correction. Incorporating the DNN allowed the controller to accommodate unmodeled dynamics and actuator anomalies—an advantage that becomes even more

critical for malfunctioning aerospace devices, where actuators may degrade unexpectedly and precise maneuvers are essential for on-orbit repairs. Furthermore, the proposed DAC scheme reliably handled multi-input multi-output (MIMO) motion control in the 6-DOF manipulator without sacrificing stability or performance.

Author contributions: Conceptualization, KZ, AZ and MV; methodology, KZ; software, JS; validation, MV, KZ and AJ; formal analysis, JW; investigation, JS; resources, KZ; data curation, KZ; writing—original draft preparation, KZ; writing—review and editing, MV; visualization, JW; supervision, JW; project administration, AJ; funding acquisition, MV. All authors have read and agreed to the published version of the manuscript.

Conflict of interest: The authors declare no conflict of interest.

References

1. Le Clainche S, Ferrer E, Gibson S, et al. Improving aircraft performance using machine learning: A review. Aerospace Science and Technology. 2023; 138: 108354. doi: 10.1016/j.ast.2023.108354
2. Ke X, Jiang A, Lu N. Load profile analysis and short-term building load forecast for a university campus. In: Proceedings of the 2016 IEEE Power and Energy Society General Meeting (PESGM); 17–21 July 2016; Boston, MA. pp. 1-5.
3. Tsukamoto H, Chung SJ, Slotine JJ. Learning-based Adaptive Control using Contraction Theory. In: Proceedings of the 60th IEEE Conference on Decision and Control (CDC); 14–17 December 2021; Austin, TX, USA. pp. 2533-2538.
4. Zhang Y, Chu L, Xu L, et al. Optimized Coordination Strategy for Multi-Aerospace Systems in Pick-and-Place Tasks By Deep Neural Network. Available online: https://arxiv.org/html/2412.09877v1 (accessed on 3 December 2024).
5. Dastider A, Raza SJA, Lin M. Learning adaptive control in dynamic environments using reproducing kernel priors with bayesian policy gradients. In: Proceedings of the 37th ACM/SIGAPP Symposium on Applied Computing; 25–29 April 2022; New York, NY, USA. pp. 748-757.
6. Gao L, Cordova G, Danielson C, et al. Autonomous multi-robot servicing for spacecraft operation extension. In: Proceedings of the 2023 IEEE/RSJ International Conference on Intelligent Robots and Systems (IROS); 1–5 October 2023; Detroit, MI, USA.
7. Shabestary SMA, Baher A. Deep learning vs. discrete reinforcement learning for adaptive traffic signal control. In: Proceedings of the 21st International Conference on Intelligent Transportation Systems (ITSC); 4–7 November 2018; Maui, HI, USA.
8. Mo K, Liu W, Shen F, et al. Precision Kinematic Path Optimization for High-DoF Robotic Manipulators Utilizing Advanced Natural Language Processing Models. In: Proceedings of the 5th International Conference on Electronic Communication and Artificial Intelligence (ICECAI); 31 May 2024–2 June 2024; Shenzhen, China.
9. Zhang Y, Wang X, Gao L, et al. Manipulator control system based on machine vision. In: *Advances in Intelligent Systems and Computing*, Proceedings of the International Conference on Applications and Techniques in Cyber Intelligence ATCI 2019: Applications and Techniques in Cyber Intelligence 7. Springer International Publishing; 2020.
10. Zhang Y, Mo K, Shen F, et al. Self-adaptive robust motion planning for high dof robot manipulator using deep mpc. In: Proceedings of the 3rd International Conference on Robotics, Artificial Intelligence and Intelligent Control (RAIIC); 5–7 July 2024; Mianyang, China.
11. Gao L, Aubert K, Saldana D, et al. Decentralized adaptive aerospace transportation of unknown loads using a team of robots. Available online: https://arxiv.org/html/2407.08084v2 (accessed on 3 December 2024).
12. Jiang A. Building Load Analysis and Forecasting—A Case Study of the Building Load of the North Carolina State University Centennial Campus. LAP LAMBERT Academic Publishing; 2014.
13. Gao L, Claus D, Rafael F. Adaptive robot detumbling of a non-rigid satellite. Available online: https://arxiv.org/html/2407.17617v2 (accessed on 3 December 2024).
14. Liu R, Xu X, Shen Y, et al. Enhanced detection classification via clustering svm for various robot collaboration task. Available online: https://arxiv.org/html/2405.03026v1 (accessed on 3 December 2024).

15. Rengasamy D, Rothwell B, Figueredo GP. Asymmetric loss functions for deep learning early predictions of remaining useful life in aerospace gas turbine engines. In: Proceedings of 2020 International Joint Conference on Neural Networks (IJCNN); 19–24 July 2020; Glasgow, UK.
16. Zhang Y, Zhu M, Gui K, et al. Development and application of a monte carlo tree search algorithm for simulating da vinci code game strategies. Available online: https://arxiv.org/html/2403.10720v1 (accessed on 3 December 2024).
17. Kuchuk H, Podorozhniak A, Hlavcheva D, Yaloveha V, et al. Application of Deep Learning in the Processing of the Aerospace System's Multispectral Images. In: Shmelova T, Sikirda Y, Sterenharz A (editors), Handbook of Research on Artificial Intelligence Applications in the Aviation and Aerospace Industries. IGI Global; 2020. pp. 134-147.
18. National Academies of Sciences, Engineering, and Medicine. Methodology to Develop the Airport Terminal Building Energy Use Intensity (ATB-EUI) Benchmarking Tool. Washington, DC: The National Academies Press.
19. Brunton SL, Kutz JN, Manohar K, et al. Data-driven aerospace engineering: reframing the industry with machine learning. AIAA Journal. 2021; 59(8): 2820-2847. doi: 10.2514/1.J060131
20. Zhang Y, Leng Q, Zhu M, et al. Enhancing Text Authenticity: A Novel Hybrid Approach for AI-Generated Text Detection. In: Proceedings of the 4th International Conference on Electronic Technology, Communication and Information (ICETCI); 24–26 May 2024; Changchun, China.
21. Saetchnikov I, Victor S, Elina T. Pattern recognition on aerospace images using deep neural networks. In: Proceedings of 2020 IEEE 7th International Workshop on Metrology for AeroSpace (MetroAeroSpace); 22–24 June 2020; Pisa, Italy.
22. Zhang Y, Gong Y, Cui D, et al. Deepgi: An automated approach for gastrointestinal tract segmentation in mri scans. Available online: https://arxiv.org/html/2401.15354v1 (accessed on 3 December 2024).
23. Ebrahimkhanlou A, Salamone S. Single-Sensor Acoustic Emission Source Localization in Plate-Like Structures Using Deep Learning. Aerospace. 2018; 5(2): 50. doi: 10.3390/aerospace5020050
24. Tan L, Liu S, Gao J, et al. Enhanced Self-Checkout System for Retail Based on Improved YOLOv10. Journal of Imaging. 2024; 10(10): 248. doi: 10.3390/jimaging10100248
25. Uzun M, Demirezen MU, Inalhan G. Physics Guided Deep Learning for Data-Driven Aircraft Fuel Consumption Modeling. Aerospace. 2021; 8(2): 44. doi: 10.3390/aerospace8020044
26. Zhu M, Zhang Y, Gong Y, et al. Ensemble methodology: Innovations in credit default prediction using lightgbm, xgboost, and localensemble. Available online: https://arxiv.org/html/2402.17979v1 (accessed on 3 December 2024).
27. Dara S, Priyanka T. Feature extraction by using deep learning: A survey. In: Proceedings of 2018 Second international conference on electronics, communication and aerospace technology (ICECA); 29–31 March 2018; Coimbatore, India.
28. Jiang A. A Simplified Dynamic Model of DFIG-based Wind Generation for Frequency Support Control Studies. International Journal of Current Science Research and Review. 2024; 7(10): 7617-7625. doi: 10.47191/ijcsrr/V7-i10-17
29. Josh G, Girish C. Deep model reference adaptive control. In: Proceedings of 2019 IEEE 58th Conference on Decision and Control (CDC); 11–13 December 2019; Nice, France.
30. Mo K, Chu L, Zhang X, et al. DRAL: Deep Reinforcement Adaptive Learning for Multi-UAVs Navigation in Unknown Indoor Environment. Available online: https://arxiv.org/html/2409.03930v3 (accessed on 3 December 2024).
31. Xu Z, Yang P, Hu K, et al. Deep learning control model for adaptive optics systems. Applied optics. 2019; 58(8): doi: 10.1364/AO.58.001998998-2009.
32. Mo K, Liu W, Xu X, et al. Fine-Tuning Gemma-7B for Enhanced Sentiment Analysis of Financial News Headlines. Available online: https://arxiv.org/html/2411.14568v1 (accessed on 3 December 2024).
33. Annaswamy AM, Guha A, Cui Y, et al. Integration of Adaptive Control and Reinforcement Learning for Real-Time Control and Learning. IEEE Transactions on Automatic Control. 2023; 68(12): 7740-7755. doi: 10.1109/tac.2023.3290037
34. Jiang A, Mo K, Fujimoto S, et al. Maximum Solar Energy Tracking Leverage High-DoF Robotics System with Deep Reinforcement Learning. Available online: https://arxiv.org/html/2411.14568v1 (accessed on 3 December 2024).
35. He Y, Liu Y, Yang L, Qu X, et al. Deep adaptive control: Deep reinforcement learning-based adaptive vehicle trajectory control algorithms for different risk levels. IEEE Transactions on Intelligent Vehicles. 2023; 9(1); 1654-1666. doi: 10.1109/TIV.2023.3303408

Mechanical Engineering Advances 2025, 3(1), 2511.
https://doi.org/10.59400/mea2511

Article

Modeling penetration depth in submerged arc welding using artificial neural networks: A comprehensive approach

Farhad Rahmati[1,2,*], Ali Shafipour[2], Masood Aghakhani[2], Farhad Kolahan[1]

[1] Department of Mechanical Engineering, Ferdowsi University of Mashhad, Mashhad 9177948944, Iran
[2] Department of Mechanical Engineering, Razi University, Kermanshah 6714967346, Iran
*** Corresponding author:** Farhad Rahmati, farhadrahmati_24@mail.um.ac.ir

CITATION

Rahmati F, Shafipour A, Aghakhani M, Kolahan F. Modeling penetration depth in submerged arc welding using artificial neural networks: A comprehensive approach. Mechanical Engineering Advances. 2025; 3(1): 2511. https://doi.org/10.59400/mea2511

ARTICLE INFO

Received: 16 January 2025
Accepted: 20 February 2025
Available online: 27 February 2025

Abstract: Penetration depth, defined as the distance from the surface of the base material to the deepest point of the molten zone, is a critical factor influencing the strength and mechanical properties of welds. This study investigates the effects of process parameters in submerged arc welding (SAW) on penetration depth, utilizing a two-hidden-layer artificial neural network (ANN) for modeling. The input parameters include arc voltage, welding current, electrode stick-out, welding speed, and the thickness of a manganese-enriched nanoparticle layer, with penetration depth as the output variable. The results demonstrate that increasing the welding current to 700 amps enhances heat transfer to the molten pool, thereby improving base material melting and penetration depth. Similarly, raising the arc voltage from 24 to 32 volts results in a moderate increase in penetration depth due to higher heat input while maintaining a relatively stable electrode melting rate. These findings highlight the potential of optimizing SAW parameters to achieve consistent weld quality and desirable mechanical properties.

Keywords: nanoparticles; penetration depth; weld geometry; submerged arc welding; artificial neural networks

1. Introduction

Welding is a versatile and essential process in manufacturing, facilitating the joining of metallic or non-metallic materials to create cohesive and durable structures. As a method that eliminates the need for disassembly, welding provides permanent and robust connections, making it indispensable across diverse industries. Applications range from infrastructure and construction projects to the automotive, aerospace, shipbuilding, and nuclear sectors, where precision and reliability are critical [1–4]. The importance of welding lies not only in its ability to create strong bonds but also in its adaptability to various materials, shapes, and industrial demands. Among the diverse welding techniques, Submerged Arc Welding (SAW) has gained prominence as a specialized and highly efficient method tailored for large-scale and demanding applications. In SAW, the welding arc is formed between a continuously fed electrode wire and the workpiece, with the arc completely submerged under a layer of granular flux. This flux, dispensed from a hopper positioned in front of the electrode, serves multiple functions, including protecting the weld zone from atmospheric contamination, stabilizing the arc, and contributing to the chemical composition of the weld metal [5,6]. The shielding effect of the flux prevents oxidation and other adverse reactions, ensuring a high-quality weld. What sets SAW apart from other welding processes is its efficiency and reliability. With a higher deposition rate compared to conventional methods, SAW allows for faster and more economical welding

operations. This efficiency is coupled with the ability to produce welds that are largely free from defects such as porosity and slag inclusions, which can compromise the structural integrity of the joint. The result is cleaner, stronger welds that meet the rigorous standards of industries requiring high-performance connections [7,8]. SAW is particularly advantageous when welding thicker materials, as it achieves deep penetration and uniform fusion across the joint. Additionally, the controlled heat input and the protective flux layer reduce thermal distortion in the workpiece, a common issue in other welding methods. The process's automation further enhances its appeal by ensuring consistent results, minimizing human error, and boosting overall production efficiency. These features make SAW a preferred choice for applications such as shipbuilding, pipeline construction, and the fabrication of pressure vessels, where precision, durability, and productivity are paramount [9,10]. The quality of welds produced through SAW is determined by evaluating both mechanical properties and geometric characteristics. Mechanical attributes, including tensile strength, hardness, and impact resistance, are critical for ensuring the weld can withstand various stresses and environmental conditions. On the other hand, geometric parameters such as bead height, width, and penetration depth are vital in assessing the weld's structural performance. Among these, penetration depth, which refers to the distance between the surface of the base material and the deepest part of the weld, is particularly significant, as it directly influences the load-bearing capacity and overall strength of the joint. Insufficient penetration can lead to weak bonds, reducing the reliability and safety of the structure [11–15]. Achieving optimal penetration depth in SAW requires precise control of process variables. Key parameters, including welding current, arc voltage, travel speed, and electrode stick-out, collectively determine the heat input, fusion efficiency, and quality of the weld. The interplay between these factors is complex, necessitating advanced methods to analyze and optimize them effectively [16–19]. In recent years, Artificial Neural Networks (ANNs) have emerged as powerful tools for studying and optimizing welding parameters. ANNs are computational models capable of identifying patterns and nonlinear relationships within datasets, making them ideal for understanding the multifaceted interactions in welding processes. By simulating the effects of variables such as current, voltage, and travel speed, ANNs enable researchers to predict welding outcomes with remarkable accuracy. This approach not only reduces the need for extensive experimental trials but also facilitates the identification of optimal parameter settings for specific applications, enhancing the efficiency and reliability of the welding process. In this study, an artificial neural network (ANN) model is applied to analyze the influence of arc voltage, electric current, electrode stick-out, and welding speed on penetration depth. In addition to the standard process parameters, the integration of nanoparticles has emerged as a promising approach to enhancing the microstructure and mechanical properties of welded joints. This novel approach underscores the potential of nanotechnology to address some of the longstanding challenges in welding, particularly in applications requiring superior performance and reliability [20–23]. Consequently, this research also examines the role of a layer of surface-adsorbed Boehmite nanoparticles containing manganese cations, exploring how this additional factor influences the welding process alongside other key parameters.

2. Boehmite nanoparticles

Aluminum oxide, commonly known as alumina, is a white crystalline powder with widespread applications in various industrial fields, including ceramics, refractory materials, and electrotechnology. Among its many phases, Boehmite (γ-AlOOH) stands out as a semi-stable form of aluminum oxide, characterized by the presence of unique surface hydroxyl (OH) groups. These groups facilitate the adsorption of various elements through OH–OH interactions, rendering Boehmite a versatile material for applications involving adsorption and catalysis [24]. The properties of Boehmite nanoparticles are particularly noteworthy due to their combination of chemical stability, superior mechanical strength, and remarkable thermal resistance. They exhibit high catalytic activity, which is further enhanced by their ability to transform into α-alumina, a thermodynamically stable phase, at elevated temperatures [25]. This transformation, combined with the cost-effective synthesis of Boehmite nanoparticles, has positioned them as a material of interest in numerous industrial and scientific endeavors [26]. One of the prominent industrial applications of Boehmite nanoparticles is their role as adsorbents in composite materials, especially in the automotive and oil industries [27]. These nanoparticles have been employed to remove impurities and enhance material properties, owing to their capacity to adsorb metallic cations. In welding processes, for instance, the incorporation of Boehmite nanoparticles enables the adsorption of manganese cations. During welding, the heat facilitates their conversion into alumina and manganese oxide, both of which contribute to the weld pool's properties. This approach offers a low-cost and efficient method to improve the mechanical and chemical characteristics of welded joints. The current study focuses on synthesizing Boehmite nanoparticles and employing them as adsorbents for manganese cations in aqueous media. This process is achieved through a chemical reaction between Boehmite nanoparticles and potassium permanganate ($KMnO_4$) solution. The synthesis method involves a carefully controlled procedure designed to ensure high adsorption efficiency and reproducibility [28,29]. The synthesis begins with the preparation of two distinct solutions. The first solution contains 6.49 g of sodium hydroxide (NaOH) dissolved in 50 mL of distilled water, while the second consists of 20 g of aluminum nitrate nonahydrate ($Al(NO_3)_3 \cdot 9H_2O$) dissolved in 30 mL of distilled water. The NaOH solution is then added dropwise at a rate of 2.94 mm/min to the aluminum nitrate solution, forming a milky suspension. To enhance the uniformity of the reaction, the suspension is subjected to sonication in an ultrasonic bath maintained at 25 ℃ for 3 h. This step ensures the homogeneous distribution of nanoparticles and promotes the formation of the desired Boehmite phase. After sonication, the precipitate is filtered and subsequently dried in an oven at 220 ℃ for 4 h to stabilize the Boehmite nanoparticles. To enable the adsorption of manganese cations onto the synthesized Boehmite nanoparticles, a secondary process is performed. A mixture containing 60 g of Boehmite nanoparticles and 19 g of $KMnO_4$ is dissolved in 400 mL of distilled water. The resulting solution undergoes ultrasonication at 25 ℃ for 15 min to enhance the interaction between the nanoparticles and the potassium permanganate. Following this, the mixture is subjected to reflux at a controlled temperature for 5 h, ensuring sufficient time for the chemical interactions to occur. To complete the process, the solution is stirred

continuously for 24 h, allowing maximum adsorption of manganese cations onto the Boehmite nanoparticle surfaces. This dual-step synthesis and adsorption methodology provides a straightforward yet effective means of enhancing the properties of Boehmite nanoparticles for specific industrial applications. The ability of these nanoparticles to adsorb manganese and subsequently convert into alumina and manganese oxide during high-temperature processes underscores their utility in welding and similar applications. By integrating this approach, it becomes possible to improve the performance and quality of welded materials while keeping production costs low. The synthesis process of boehmite nanoparticles and the formation of crystalline phases are schematically illustrated in **Figure 1**. The diagram includes the preparation of precursors, crystallization at room temperature, formation of the bayerite phase, conversion to the boehmite phase through heating, and the application of ultrasound waves to enhance nanoparticle dispersion.

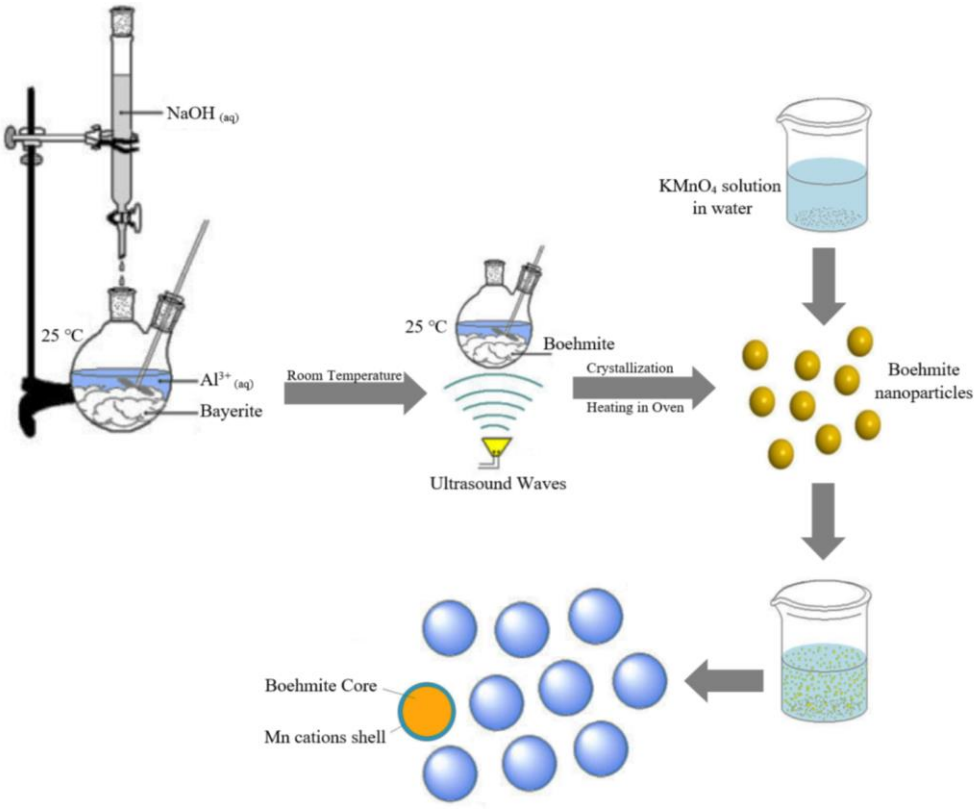

Figure 1. Schematic illustration of boehmite nanoparticle synthesis and crystalline phase formation.

3. Artificial neural network

The Submerged Arc Welding (SAW) process is widely utilized in industrial applications due to its capability to produce high-quality welds with excellent mechanical properties. However, optimizing the process parameters to achieve desired outcomes, such as penetration depth, remains a challenging task. Various factors, including arc voltage, electric current, electrode stick-out, and welding speed, significantly influence the weld quality and characteristics. Modeling the intricate relationships among these parameters is crucial for improving the efficiency and

reliability of the SAW process. Artificial neural networks (ANNs) have emerged as a potent computational tool to model complex systems and nonlinear relationships [30,31]. These systems are inspired by the biological neural networks of the human brain, mimicking their ability to process and analyze data through interconnected layers of nodes or neurons. ANNs have been extensively employed in diverse domains, including image recognition, natural language processing, solving differential equations, and predictive modeling [32,33]. Their adaptability and capability to generalize make them suitable for applications in welding and materials science. A typical ANN structure comprises three main layers: The input layer, one or more hidden layers, and the output layer. The input layer serves as the interface for receiving raw data from the external environment. Each node in this layer corresponds to a specific input parameter. For the SAW process, the input parameters include arc voltage, electric current, electrode stick-out, welding speed, and nanoparticle layer thickness. These parameters are critical as they directly impact the weld penetration and overall quality. The hidden layer, positioned between the input and output layers, plays a central role in processing and analyzing the input data. The number of hidden layers and the nodes within each layer can be customized based on the complexity of the problem. For relatively simple problems, a single hidden layer with a small number of nodes might suffice. However, more intricate relationships demand deeper networks with multiple hidden layers, often requiring greater computational resources. In the context of SAW modeling, the hidden layer processes the input parameters through weighted connections and activation functions, enabling the network to learn and approximate the underlying relationships effectively. The output layer constitutes the final stage of an ANN, producing the model's predictions or classifications. In the present study, the output layer consists of a single node that predicts the penetration depth based on the processed data from the hidden layer. By mapping the input parameters to the desired output, the ANN provides a robust framework for understanding and optimizing the SAW process. The architecture of the ANN used in this research is designed to capture the nonlinear dependencies between the input parameters and the output variable. Specifically, the input layer comprises five nodes representing the aforementioned parameters, while the hidden layer consists of three nodes to balance computational efficiency and modeling accuracy. The connections between the nodes are governed by weights, which are iteratively adjusted during the training phase to minimize the error between the predicted and actual values. This iterative process, known as backpropagation, involves calculating the gradient of the error concerning the weights and updating them accordingly. One of the key advantages of using ANNs for modeling the SAW process is their ability to generalize from training data to unseen scenarios. By leveraging a sufficient dataset that encapsulates a wide range of input-output combinations, the ANN can identify patterns and relationships that are difficult to discern through traditional analytical methods. Moreover, the flexibility of ANNs allows for the incorporation of additional input parameters or the adjustment of network architecture as needed, making them a versatile tool for process optimization.

The current research focuses on utilizing an ANN model to predict the penetration depth during the SAW process. By systematically altering input parameters such as arc voltage, current, electrode stick-out, welding speed, and the

thickness of a nanoparticle layer composed of manganese-containing Boehmite nanoparticles, the model offers critical insights into the underlying process dynamics. The structure of the ANN used in this study, shown in **Figure 2**, demonstrates the arrangement of input, hidden, and output layers specifically designed to address the complexities of the SAW process. This architecture ensures a balance between computational efficiency and prediction accuracy. The findings emphasize the transformative role of ANNs in welding applications, highlighting their capability to manage intricate nonlinear relationships and adapt to varying operational conditions. By offering a robust framework for optimizing process parameters, ANNs significantly enhance the efficiency, quality, and consistency of welds, contributing to the advancement of modern manufacturing methodologies.

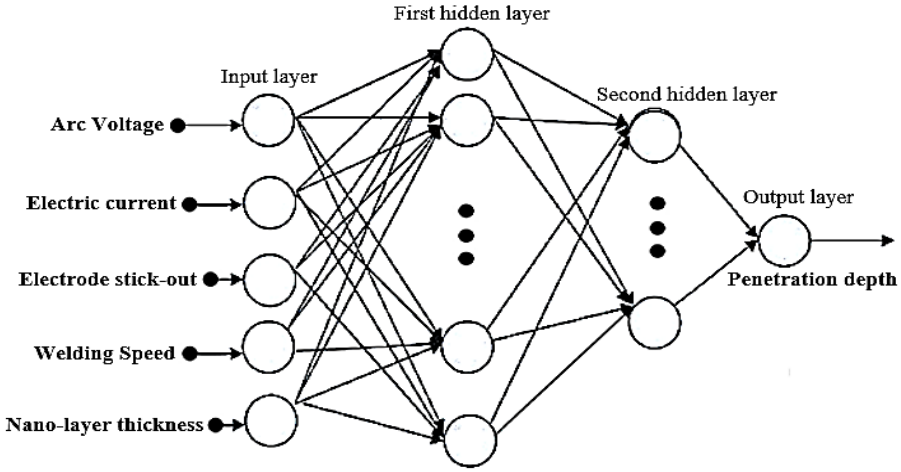

Figure 2. Developed the structure of an artificial neural network model.

4. Experimentation and data collection

ST37 is a mild carbon steel known for its ease of processing and favorable mechanical properties. With a carbon content of approximately 0.17%, this steel is characterized by its ability to maintain a balance between strength and flexibility, making it ideal for a wide range of structural applications. Frequently used in industries such as construction and manufacturing, ST37's qualities make it suitable for components like beams, bridges, and machinery frames that require reliable load-bearing performance. Its excellent weldability further enhances its utility in processes like Submerged Arc Welding (SAW), where achieving robust, durable joints is essential for maintaining long-term structural integrity. In this study, SAW was performed on St37 steel plates, each with dimensions of 15 × 50 × 150 mm^3. The welding operation utilized a direct current (DC) reverse polarity configuration, known for its stability and efficient heat input during the welding process. The setup included a PARS CAT P2310 semi-automatic robotic system, ensuring precision and repeatability throughout the welding operations. The power supply was provided by a PARC ARC 1203T unit, designed with a constant voltage characteristic, which is critical for maintaining consistent weld quality. The consumables used in the welding process comprised a specialized welding wire and flux, whose detailed chemical compositions are provided in **Table 1**. These consumables were carefully selected to

ensure optimal compatibility with the base material and enhance the mechanical properties of the resulting weld joint. In addition, the experimental setup incorporated a layer of Boehmite nanoparticles adsorbed with manganese cations applied to the surface of the base material. This layer was introduced to investigate its potential effects on the welding process and the quality of the weld zone. The key process parameters examined in this investigation included arc voltage, electric current, electrode stick-out length, welding speed, and the thickness of the nanoparticle layer. Preliminary experiments were conducted using a One Variable at a Time (OVAT) approach to establish appropriate ranges for these variables. During these trials, each parameter was varied independently while maintaining all other conditions constant, allowing for the identification of its influence on weld quality. The outcomes of these initial experiments helped define the minimum and maximum values for each parameter, ensuring a systematic and well-controlled experimental design. These ranges are summarized in **Table 2**. Following the determining suitable parameter ranges, a Central Composite Rotatable Design (CCRD) was employed to organize the experimental framework. This statistical method enables a comprehensive evaluation of parameter interactions while minimizing the number of required experiments. The input variables were varied across five levels (−2, −1, 0, +1, and +2), creating a robust design matrix. The matrix and the corresponding experimental results are detailed in **Table 3**. By using this approach, the study aimed to model the complex relationships between the input variables and the welding outcomes, focusing particularly on the depth of weld penetration. Weld penetration depth is a critical factor in ensuring the structural integrity of welded joints, as it directly influences the mechanical performance and load-bearing capacity of the weld. To accurately model this parameter, an artificial neural network (ANN) was implemented. The ANN was trained using the experimental data, enabling it to predict weld penetration depth based on variations in the input parameters. **Figure 3** illustrates the weld-melted zone observed in the prepared workpiece. This zone represents the region where the base material has undergone melting and subsequent solidification during the welding process. The microstructural characteristics of this region are of significant importance, as they directly impact the mechanical properties and long-term performance of the weld. The formation of a uniform and defect-free melted zone is indicative of successful parameter selection and process control.

Table 1. Chemical composition of the wire and flux.

Chemical composition of the welding wire				
Element	C	Mn	Si	Fe
%W	0.04–0.08	0.9–1.3	0.5–0.8	Balance
Chemical composition of the consumed flux				
$SiO_2 + TiO_2$	$Al_2O_3 + MnO$		CaF_2	
% 5	% 55		% 30	

Table 2. Input parameters and their ranges.

Parameter	Coded values				
	−2	**−1**	**0**	**+1**	**+2**
Arc Voltage (volts)	24	26	28	30	32
Electric current (amp)	500	550	600	650	700
Electrode stick-out (mm)	30	32.5	35	37.5	40
Welding Speed (mm/min)	300	350	400	450	500
Nano-layer thickness (mm)	0	0.25	0.5	0.75	1

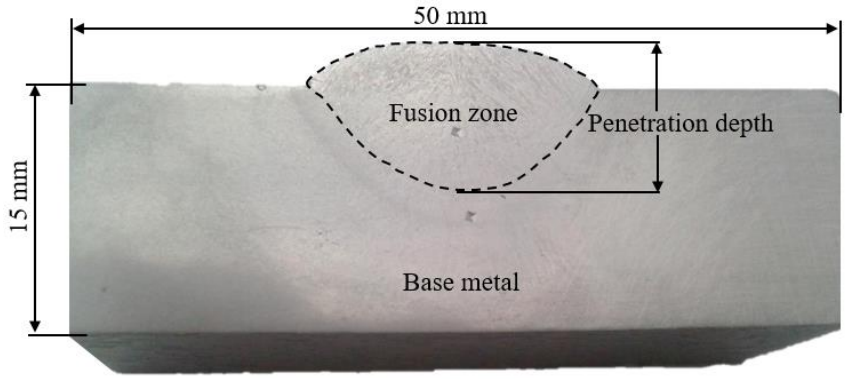

Figure 3. Weld-melted zone in the prepared sample.

Table 3. Input parameters and their ranges.

Std.	Arc voltage (volts)	Electric current (amp)	Electrode stick-out (mm)	Welding speed (mm/min)	Nano-layer thickness (mm)	Penetration depth (mm)	Error
1	28	600	35	400	0.5	7.01	−0.242
2	28	600	35	300	0.5	8.14	0.400
3	26	650	32.5	450	0.75	7.65	0.179
4	26	550	37.5	450	0.75	4.14	−1.363
5	30	650	37.5	350	0.25	9.28	0.363
6	28	700	35	400	0.5	8.80	−0.169
7	30	650	32.5	450	0.25	10.13	1.409
8	28	600	30	400	0.5	7.68	0.312
9	26	550	32.5	350	0.75	5.98	0.090
10	30	650	32.5	350	0.75	8.37	−0.599
11	26	550	37.5	350	0.25	6.09	0.587
12	28	600	35	400	0.5	6.90	−0.352
13	28	600	35	400	0	8.24	0.987
14	26	550	32.5	450	0.25	5.55	−0.129
15	30	550	37.5	450	0.25	5.18	−0.323
16	28	600	35	400	0.5	7.05	−0.202
17	28	600	35	400	0.5	6.89	−0.362
18	26	650	37.5	350	0.75	7.81	−0.207
19	28	600	35	400	1	6.57	−0.188

Table 3. (*Continued*).

Std.	Arc voltage (volts)	Electric current (amp)	Electrode stick-out (mm)	Welding speed (mm/min)	Nano-layer thickness (mm)	Penetration depth (mm)	Error
20	30	650	37.5	450	0.75	8.37	−0.396
21	30	550	32.5	350	0.25	8.14	0.935
22	30	550	37.5	350	0.75	7.29	1.787
23	24	600	35	400	0.5	6.43	−0.823
24	28	600	35	400	0.5	7.27	0.018
25	30	550	32.5	450	0.75	4.62	−0.883
26	28	600	35	400	0.5	6.98	−0.272
27	26	650	32.5	350	0.25	7.75	−0.170
28	26	650	37.5	450	0.25	7.48	0.227
29	28	600	35	500	0.5	6.31	0.094
30	32	600	35	400	0.5	7.89	−0.705
31	28	600	40	400	0.5	6.81	1.307
32	28	500	35	400	0.5	4.64	−0.863
33	28	600	35	300	0.5	8.13	0.316
34	26	650	32.5	450	0.75	7.60	0.149
35	30	650	37.5	350	0.25	9.25	0.193
36	28	700	35	400	0.5	8.75	0.111
37	28	600	30	400	0.5	7.60	0.102
38	26	550	32.5	350	0.75	6.20	0.160
39	26	550	37.5	350	0.25	6.30	0.727
40	28	600	35	400	0.5	6.50	−0.132
41	26	550	32.5	450	0.25	5.70	−0.049
42	30	550	37.5	450	0.25	5.20	−0.333
43	28	600	35	400	0.5	7.10	−0.132
44	26	650	37.5	350	0.75	7.80	−0.327
45	28	600	35	400	1	6.60	−0.068
46	30	650	37.5	450	0.75	8.40	−0.676
47	30	550	37.5	350	0.75	7.30	1.777
48	28	600	35	400	0.5	6.90	−0.132
49	30	550	32.5	450	0.75	4.80	−0.893
50	28	600	35	400	0.5	7.02	−0.132
51	26	650	37.5	450	0.25	7.50	0.227
52	32	600	35	400	0.5	7.80	−0.495
53	28	600	40	400	0.5	6.80	1.257

5. Results and discussion

This study aimed to optimize the penetration depth in Submerged Arc Welding (SAW) by developing a neural network model that links input parameters to the output

variable, which is the penetration depth. The structure of the Artificial Neural Network (ANN) consisted of five neurons in the input layer and one neuron in the output layer. To identify the optimal welding conditions for achieving maximum penetration depth, regression analysis was employed alongside the neural network to evaluate the relationships between the input parameters and the resulting penetration depth. The input parameters included arc voltage, electric current, electrode stick-out, welding speed, and the thickness of the nanoparticle layer, while the output layer represented the penetration depth. For model training, data were randomly selected, and the Levenberg-Marquardt optimization algorithm was applied. A total of 70% of the data was used for training the neural network, adjusting the model based on the calculated error. The remaining 20% was reserved for validating the network, allowing for an assessment of its generalization ability and the cessation of training once further improvements were no longer observed. The final 10% of the data served as the test set, providing an independent measure of the network's performance throughout and after training. **Figure 4** shows an error histogram, representing the distribution of errors for each data group. The regression coefficients comparing the experimental and neural network data for maximizing penetration depth are displayed in **Figure 5**. **Figure 6** illustrates the performance plot of the Artificial Neural Network (ANN) in terms of Mean Squared Error (MSE) and *R*-values, which evaluate the correlation between predicted outputs and target values. The MSE values for the training, validation, and testing datasets were 7.8396×10^{-2}, 5.3101×10^{-2}, and 9.1429×10^{-2}, respectively, highlighting the model's predictive accuracy. A lower MSE value corresponds to better network performance, indicating reduced deviation between predicted and actual values. The *R*-values, reflecting the correlation strength, were 9.9712×10^{-1}, 9.8534×10^{-1}, and 9.6030×10^{-1} for training, validation, and testing, respectively. These values, close to 1, demonstrate a high correlation between network outputs and the target data. The performance plot shows how MSE decreases over 35 epochs for all datasets, with a rapid decline in the initial stages, indicating effective learning. By epoch 29, the network achieves its optimal configuration, as denoted by the circled point labeled "Best." The model exhibits the lowest validation MSE at this point, signifying an optimal balance between accuracy and generalization. The training process halts after six consecutive validation checks without improvement, which prevents overfitting and ensures a robust model. The consistent trend across the training, validation, and testing datasets suggests that the ANN maintains reliability across different data partitions. These findings confirm the network's ability to effectively learn complex input-output relationships and provide accurate predictions for penetration depth in SAW. Additionally, the study explored the influence of various factors, including arc voltage, electric current, electrode stick-out, welding speed, and nanoparticle layer thickness, on the weld penetration depth. **Figure 7** illustrates the influence of various input parameters on penetration depth during the SAW process. The results show that electric current has the most significant impact, with penetration depth increasing markedly as the current rises from 500 to 700 amps due to higher heat input, enhancing base material melting. The results revealed that the intensity of the electric current plays a significant role in determining the welding geometry, as higher current values led to increased penetration depth. This effect is attributed to the greater melting of both the base metal and the welding wire. However,

excessively high currents can result in energy loss and deterioration of the welding wire [34,35]. Arc voltage also contributes to penetration depth, albeit to a lesser extent, with a modest increase observed as the voltage rises from 24 to 32 volts, resulting from slightly higher heat input without substantial changes in electrode melting rate. Electrode stick-out, on the other hand, exhibits an inverse relationship with penetration depth; increasing the distance from 30 to 40 mm reduces heat concentration at the weld pool, leading to shallower penetration. Similarly, welding speed inversely affects penetration depth, with faster speeds (300 to 500 mm/min) reducing the time for heat transfer, thereby diminishing weld penetration [34,35]. Lastly, the addition of nanoparticles reduces penetration depth by decreasing the thermal conductivity of the molten pool, limiting heat transfer to the workpiece as the nano-layer thickness increases.

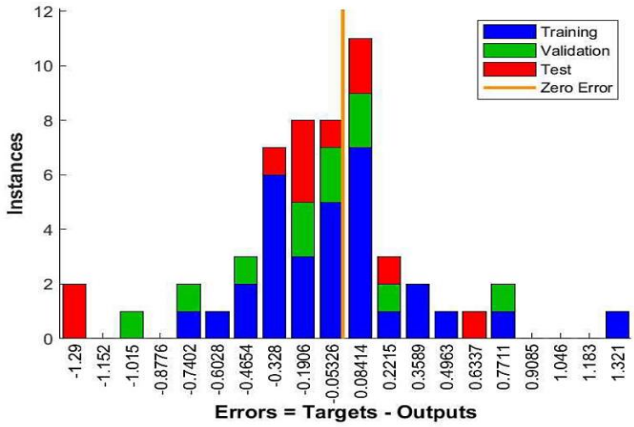

Figure 4. The regression coefficients of experimental data and neural network training data.

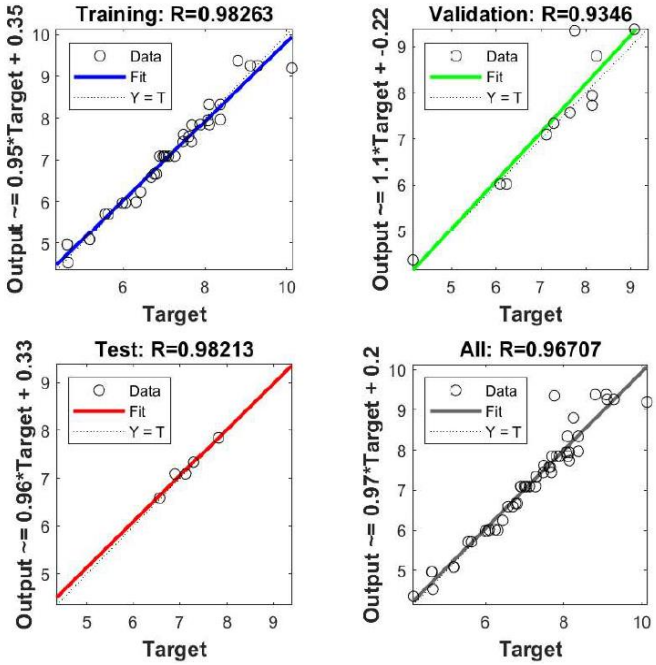

Figure 5. The regression coefficients of experimental data and neural network training data.

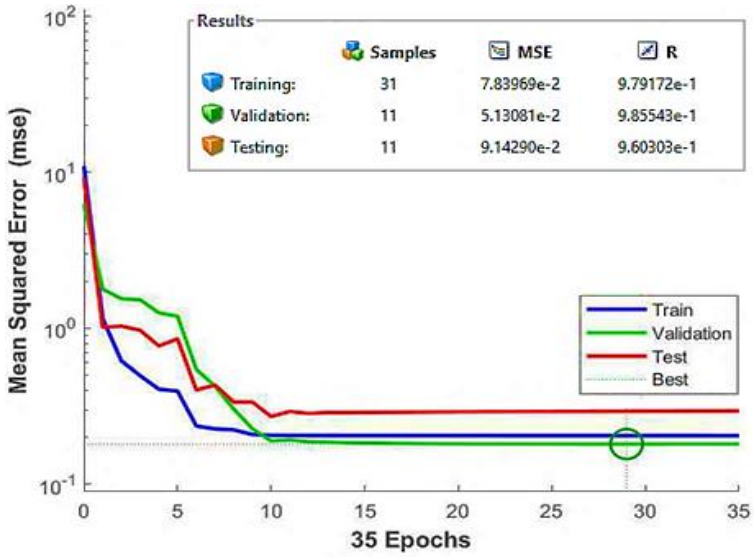

Figure 6. Performance plot: The mean squared error and *R*-values between outputs and target.

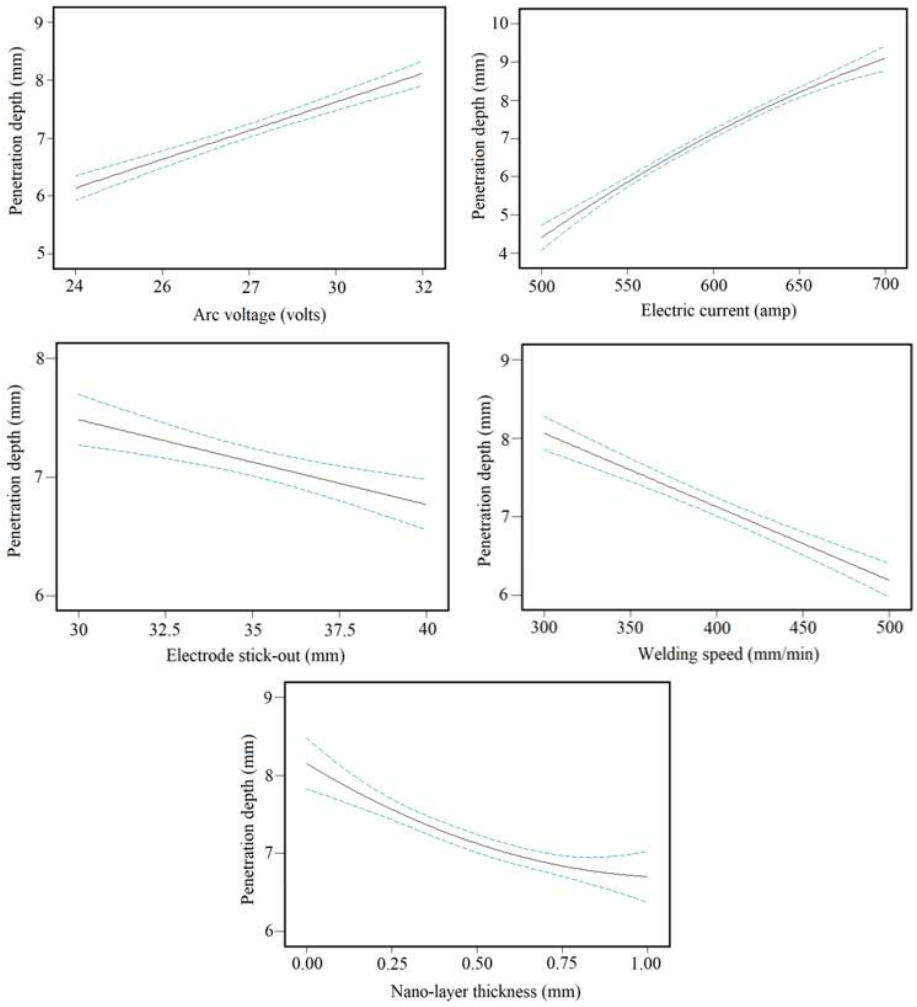

Figure 7. The effect of input parameters on the penetration depth.

6. Conclusions

Submerged Arc Welding (SAW) is a widely employed technique in various industrial sectors, appreciated for its ability to produce strong, defect-free welds. In this research, Artificial Neural Networks (ANNs) were applied to model and optimize penetration depth in the SAW process, addressing the challenges posed by traditional experimental methods. The ANN model provided highly accurate predictions, as demonstrated by low Mean Squared Error (MSE) and high correlation coefficients, verifying its reliability in predicting the effects of input parameters on penetration depth. The study revealed that electric current has the most significant impact on penetration depth, with higher currents increasing heat input and thus enhancing penetration. Arc voltage also contributed to heat transfer, but with a smaller effect. On the other hand, greater electrode stick-out and faster welding speeds were found to decrease penetration depth, as they reduce the concentration of heat in the weld pool. Additionally, the inclusion of nanoparticle layers on the workpiece reduced penetration depth due to their lower thermal conductivity, which limited heat transfer. These findings confirm that ANN-based modeling is a powerful tool for optimizing the SAW process. By offering precise predictions of penetration depth, this approach aids in improving the understanding of key process parameters and can help reduce the need for extensive experimental trials.

Author contributions: Conception and design of the study, FR, AS, MA and FK; prepared the manuscript and conducted data collection and analysis, FR; performed the experiments and collected the data, AS; designed and supervised the project revised the data, and performed the data analysis, MA; analyzed and revised the manuscript, FK. All authors have read and agreed to the published version of the manuscript.

Acknowledgments: The authors would like to thank the Razi University for their assistance throughout the research.

Ethical approval: Not applicable.

Data and code availability: All data used in the paper are cited.

Conflict of interest: The authors declare no conflict of interest.

References

1. Zhang YM, Yang YP, Zhang W, et al. Advanced Welding Manufacturing: A Brief Analysis and Review of Challenges and Solutions. Journal of Manufacturing Science and Engineering. 2020; 142(11). doi: 10.1115/1.4047947
2. Rahmati F, Aghakhani M, Kolahan F. Influence of Siliconized Zn-Graphene Oxide Complex Nanoparticles on the Microstructure and Mechanical Properties of AA5083: Focus on Gas Metal Arc Welding. Advances in Materials Science and Engineering. 2023; 2023: 1-14. doi: 10.1155/2023/3892612
3. Dwivedi DK. Dissimilar Metal Joining. Springer Nature Singapore; 2023. doi: 10.1007/978-981-99-1897-3
4. Rahmati F, Kolahan F, Aghakhani M. Prediction of weld bead geometry of AA5083 using taguchi technique: in the presence of siliconized zn-graphene oxide complex nanoparticles. The International Journal of Advanced Manufacturing Technology. 2024; 136(1): 3-14. doi: 10.1007/s00170-024-13074-0
5. Dwivedi DK. Fundamentals of Metal Joining. Springer Singapore; 2022. doi: 10.1007/978-981-16-4819-9

6. Rathi AK. To study the effect of submerged arc welding parameters on bead geometry and hardness for mild steel (IS-2062A) using fractional factorial design. Materials Today: Proceedings. 2021; 34: 525-530. doi: 10.1016/j.matpr.2020.03.106
7. Patel HN, Chauhan VD, George PM. Effect of process parameters on submerged arc welding: A review. In: Proceedings of the 14th asia-pacific physics conference; 2021. doi: 10.1063/5.0036234
8. Jindal S, Singh M, Chauhan J. Effect and Optimization of Welding Parameters and Flux Baking on Weld Bead Properties and Tensile Strength in Submerged Arc Welding of HSLA 100 Steel. Transactions of the Indian Institute of Metals. 2023; 77(3): 747-766. doi: 10.1007/s12666-023-03158-y
9. Barbosa LHS, Modenesi PJ, Godefroid LB, et al. Fatigue crack growth rates on the weld metal of high heat input submerged arc welding. International Journal of Fatigue. 2019; 119: 43-51. doi: 10.1016/j.ijfatigue.2018.09.020
10. Rajkumar T, Prabakaran MP, Arunkumar G, et al. Evaluation of mechanical and metallurgical properties of submerged arc welded plate joint. Materials Today: Proceedings. 2021; 37: 1367-1371. doi: 10.1016/j.matpr.2020.06.563
11. Choudhary A, Kumar M, Unune DR. Experimental investigation and optimization of weld bead characteristics during submerged arc welding of AISI 1023 steel. Defence Technology. 2019; 15(1): 72-82. doi: 10.1016/j.dt.2018.08.004
12. Kumar R, Dikshit I, Verma A. Experimental investigations and statistical modelling of dilution rate and area of penetration in submerged arc welding of SS316-L. Materials Today: Proceedings. 2021; 44: 3997-4003. doi: 10.1016/j.matpr.2020.10.201
13. Garg J, Garg SB, Jeet B, et al. The effects of flux particle size and column height on the bead geometry in submerged arc welding. Sādhanā. 2022; 47(4). doi: 10.1007/s12046-022-01971-7
14. Mezaache M, Benaouda OF, Kellai A. Maximizing welding efficiency: applying an improved whale optimization algorithm for parametric optimization of bead width in a submerged arc welding process. The International Journal of Advanced Manufacturing Technology. 2024; 134(5-6): 2737-2752. doi: 10.1007/s00170-024-14231-1
15. Shafipour A, Rahmati F, Aghakhani M, et al. Optimization of penetration depth in submerged arc welding using genetic algorithm. The International Journal of Advanced Manufacturing Technology. 2024; 136(1): 123-132. doi: 10.1007/s00170-024-13976-z
16. Sharma H, Rajput B, Singh RP. A review paper on effect of input welding process parameters on structure and properties of weld in submerged arc welding process. Materials Today: Proceedings. 2020; 26: 1931-1935. doi: 10.1016/j.matpr.2020.02.422
17. Sailender M, Reddy GCM, Venkatesh S. Parametric Design for Purged Submerged Arc Welding on Strength of Low Carbon Steel. European Journal of Engineering and Technology Research. 2018; 1(3): 1-6. doi: 10.24018/ejeng.2016.1.3.132
18. Ankush C, Kumar M, Unune DR. Parametric modeling and optimization of novel water-cooled advanced submerged arc welding process. The International Journal of Advanced Manufacturing Technology. 2018; 97(1-4): 927-938. doi: 10.1007/s00170-018-1944-7
19. Vedrtnam A, Singh G, Kumar A. Optimizing submerged arc welding using response surface methodology, regression analysis, and genetic algorithm. Defence Technology. 2018; 14(3): 204-212. doi: 10.1016/j.dt.2018.01.008
20. da Silva MM, Batista VR, Maciel TM, et al. Optimization of submerged arc welding process parameters for overlay welding. Welding International. 2017; 32(2): 122-129. doi: 10.1080/09507116.2017.1347325
21. Choudhary S, Shandley R, Kumar A. Optimization of agglomerated fluxes in submerged arc welding. Materials Today: Proceedings. 2018; 5(2): 5049-5057. doi: 10.1016/j.matpr.2017.12.083
22. Aleshin NP, Grigor'ev MV, Kobernik NV, et al. Modification of Weld Metal with Tungsten Carbide and Titanium Nitride Nanoparticles in Twin Submerged Arc Welding. High Energy Chemistry. 2018; 52(5): 440-445. doi: 10.1134/s0018143918050028
23. Naderian P, Aghakhani M, Khoshboo S. Modelling the hardness of weld metal in the submerged arc welding of low carbon steel plates: addition of CR2O3 nanoparticles. Advances in Materials and Processing Technologies. 2022; 9(1): 221-236. doi: 10.1080/2374068x.2022.2091186
24. Vatanpour V, Madaeni SS, Rajabi L, et al. Boehmite nanoparticles as a new nanofiller for preparation of antifouling mixed matrix membranes. Journal of Membrane Science. 2012; 401-402: 132-143. doi: 10.1016/j.memsci.2012.01.040
25. Jabbari A, Tahmasbi B, Nikoorazm M, et al. A new Pd-Schiff-base complex on boehmite nanoparticles: Its application in Suzuki reaction and synthesis of tetrazoles. Applied Organometallic Chemistry. 2018; 32(6). doi: 10.1002/aoc.4295

26. Ghorbani-Choghamarani A, Seydyosefi Z, Tahmasbi B. Zirconium oxide complex anchored on boehmite nanoparticles as highly reusable organometallic catalyst for C–S and C–O coupling reactions. Applied Organometallic Chemistry. 2018; 32(8). doi: 10.1002/aoc.4396
27. Rajabi L, Derakhshan AA. Room Temperature Synthesis of Boehmite and Crystallization of Nanoparticles: Effect of Concentration and Ultrasound. Science of Advanced Materials. 2010; 2(2): 163-172. doi: 10.1166/sam.2010.1063
28. Ghorbani-Choghamarani A, Seydyosefi Z, Tahmasbi B. Tribromide ion supported on boehmite nanoparticles as a reusable catalyst for organic reactions. Comptes Rendus Chimie. 2018; 21(11): 1011-1022. doi: 10.1016/j.crci.2018.09.001
29. Chen W, Yang T, Dong L, et al. Advances in graphene reinforced metal matrix nanocomposites: Mechanisms, processing, modelling, properties and applications. Nanotechnology and Precision Engineering. 2020; 3(4): 189-210. doi: 10.1016/j.npe.2020.12.003
30. Schrimpf M, Kubilius J, Hong H, et al. Brain-Score: Which Artificial Neural Network for Object Recognition is most Brain-Like?. BioRxiv; 2018. doi: 10.1101/407007
31. Anitescu C, Atroshchenko E, Alajlan N, et al. Artificial Neural Network Methods for the Solution of Second Order Boundary Value Problems. Computers, Materials & Continua. 2019; 59(1): 345-359. doi: 10.32604/cmc.2019.06641
32. Zhao D, Wang Y, Liang D, et al. Performances of regression model and artificial neural network in monitoring welding quality based on power signal. Journal of Materials Research and Technology. 2020; 9(2): 1231-1240. doi: 10.1016/j.jmrt.2019.11.050
33. Sekban DM, Yaylacı EU, Özdemir ME, et al. Investigating Formability Behavior of Friction Stir-Welded High-Strength Shipbuilding Steel using Experimental, Finite Element, and Artificial Neural Network Methods. Journal of Materials Engineering and Performance. 2024. doi: 10.1007/s11665-024-09501-8
34. Karadeniz E, Ozsarac U, Yildiz C. The effect of process parameters on penetration in gas metal arc welding processes. Materials & Design. 2007; 28(2): 649-656. doi: 10.1016/j.matdes.2005.07.014
35. Karaoğlu S, Seçgin A. Sensitivity analysis of submerged arc welding process parameters. Journal of Materials Processing Technology. 2008; 202(1-3): 500-507. doi: 10.1016/j.jmatprotec.2007.10.035

Mechanical Engineering Advances 2025, 3(1), 2150.
https://doi.org/10.59400/mea2150

Article

Design and implementation of a cleaning robot

Yung-Hsiang Chen*, Sheng-Yan Pan

Department of Mechanical Engineering, National Pingtung University of Science and Technology, Pingtung 912301, Taiwan
*** Corresponding author:** Yung-Hsiang Chen, yhchen@mail.npust.edu.tw

CITATION

Chen YH, Pan SY. Design and implementation of a cleaning robot. Mechanical Engineering Advances. 2025; 3(1): 2150. https://doi.org/10.59400/mea2150

ARTICLE INFO

Received: 27 November 2024
Accepted: 24 January 2025
Available online: 27 February 2025

Abstract: This study focuses on the development of a cleaning robot, covering the three main aspects of mechanical design, circuit design, and software design. First, in the area of mechanical design, we created a structure capable of agile movement and efficient cleaning to ensure the robot can operate smoothly in various environments. Second, for circuit design, we developed a microcontroller-based control system to coordinate the operation of various components, including drive motors, sensors, and image recognition modules. Furthermore, in the software design aspect, we utilized YOLO (You Only Look Once) and OpenCV technologies to enable the robot to accurately identify and classify waste during the automatic cleaning process. Finally, we conducted practical cleaning experiments to verify the robot's ability to recognize waste and the accuracy of waste classification. The experimental results show that the cleaning robot not only possesses the ability to recognize waste but also accurately classify it, demonstrating its potential for practical applications.

Keywords: cleaning robot; mechanical design; circuit design; software design; image recognition; waste classification; YOLO

1. Introduction

With the rapid advancement of artificial intelligence technology and the widespread adoption of smart environment concepts, cleaning robots have become essential tools in modern environments as technology evolves quickly, the demand for efficient and intelligent cleaning solutions continues to grow. Traditional cleaning methods are increasingly unable to meet the high-intensity and complex cleaning requirements of various environments. In recent years, cleaning robots that incorporate machine learning and computer vision have become essential solutions to modern cleaning challenges, as they not only perform cleaning tasks efficiently but also adapt to diverse application scenarios [1–5].

Advancements in robot navigation and sensing technologies have driven the evolution of cleaning robots. Today's cleaning robots must possess accurate environmental perception and motion planning capabilities to cope with the diverse and dynamic indoor and outdoor environments. From a design perspective, enhancing the flexibility and stability of the motion mechanism is critical for improving the robot's cleaning efficiency [6]. Additionally, the application of multi-sensor fusion technology, integrating various data to achieve more accurate environmental modeling and localization, has become a key challenge in modern cleaning robot technology. This study focuses on optimizing the mobile mechanism to improve its stability and work efficiency in different operational environments [7–9].

In terms of hardware design, microcontroller-based circuit architecture can effectively reduce costs and improve control precision. A microcontroller is a small computing system that integrates a processor, memory, and input/output interfaces,

typically used to control electronic devices or systems. Research shows that coordinating drive motors, sensors, and image processing modules using microcontrollers is a major approach in implementing the control systems of cleaning robots [10,11]. Regarding the technical demands of garbage identification and classification, image processing has gradually been integrated into the design of cleaning robots. For example, the integration of technologies such as YOLO and OpenCV enables cleaning robots to more accurately identify garbage features, thereby improving classification accuracy [12,13].

Although current cleaning robots can achieve a certain level of automation, there is still room for improvement in the accuracy of garbage recognition and classification. Studies show that image processing using deep learning models can significantly improve classification accuracy, but it also increases the demand for computational resources. Therefore, this study optimizes the image recognition algorithms in the software design to balance recognition accuracy with system computational load, enhancing response efficiency [14–17].

The development of this cleaning robot covers three main aspects: motion mechanism design, electronic circuit design, and software development. In terms of motion mechanism design, our goal is to create a stable mobility system that meets the demands of diverse scenarios, while optimizing the garbage collection system to enhance cleaning efficiency. In electronic circuit design, we employ a microcontroller-based architecture that integrates various sensors and control modules to precisely coordinate the robot's movements. The software development section uses YOLO and OpenCV for image recognition and garbage classification, which not only improves classification accuracy but also reduces the risk of misclassification. Finally, a series of application scenario experiments are conducted to verify the garbage identification and classification performance of the robot. See the end of the document for further details on references [18–20].

2. Design of a cleaning robot

This section focuses on the design of the cleaning robot from three perspectives [21,22]: mechanical, circuit, and software design. The mechanical design section covers material selection and structural engineering for building the robot. The circuit design section explains the control and drive mechanisms. Lastly, the software design section details the use of deep learning models and programming to enable garbage classification, image detection, and recognition.

2.1. Mechanical design

This section focuses on the material selection and structural design of the cleaning robot's power module. The primary structural material is 6061 aluminum alloy. Initial design sketches are created in SOLIDWORKS, followed by computer numerical control (CNC) machining to fabricate the individual components. CNC machining is the use of computer numerical control technology to precisely control machine tools to shape and size materials with high accuracy. The cleaning robot's mechanism is divided into four main parts: chassis, transmission, cleaning, and conveying. The chassis support plate is secured with high-strength bolts for enhanced

stability, while precision components support the transmission, cleaning, and conveying systems to ensure operational accuracy and reliability.

2.1.1. Material selection

In this study, aluminum alloy 6061, as shown in **Figure 1**, is chosen as the primary structural material for the power module chassis, with the parts processed through CNC machining. The advantages of using 6061 aluminum alloy are as follows:

- Higher Strength and Hardness: After heat treatment (T6), 6061 aluminum alloy offers enhanced strength and hardness, making it more durable than aluminum extrusions and suitable for bearing heavy loads.
- Suitability for Complex Structures and Non-Standard Shapes: 6061 can be processed using CNC machining to create parts with complex shapes, allowing for customization according to specific requirements.
- Better Precision: CNC machining of 6061 aluminum alloy ensures high precision and smooth surface finishes.
- Good Fatigue Resistance: 6061 exhibits excellent fatigue resistance, especially after heat treatment, making it ideal for long-term loading applications.
- Corrosion Resistance: With its strong corrosion resistance, 6061 is well-suited for use in the humid environment of Taiwan.

Figure 1. Cleaning robot materials of aluminum alloy plate.

2.1.2. Structural design

In designing the chassis structure, we used SOLIDWORKS for modeling and analysis. SOLIDWORKS is a powerful 3D design software that provides precise drawing and modeling tools, effectively supporting the design of complex chassis structures. First, we created an initial design model based on requirements, considering chassis strength, rigidity, and weight to meet application needs. At the same time, we ensured that manufacturability and ease of assembly were considered, resulting in a simple and efficient structure that is easy to produce.

During the chassis manufacturing phase, a CNC milling machine was used to produce the chassis parts, ensuring machining accuracy and stability. The CNC milling machine offers high precision and cutting capability, making it ideal for producing parts to the exact dimensions and shapes designed in SOLIDWORKS. This not only

ensures structural consistency but also eliminates errors that may arise from manual processes.

To guarantee assembly accuracy and structural stability, precision-matched connections were used between the plates, and high-strength bolts secured the components. This design and manufacturing process enhance the chassis durability and load resistance, ensuring stable performance under various loading conditions.

The cleaning robot's mechanism is planned as a comprehensive system divided into four main parts: the chassis structure, transmission structure, garbage cleaning structure, and conveyor belt structure. Based on this, we created the cleaning robot assembly diagram and parts list, as shown in **Figure 2**, with detailed descriptions provided below.

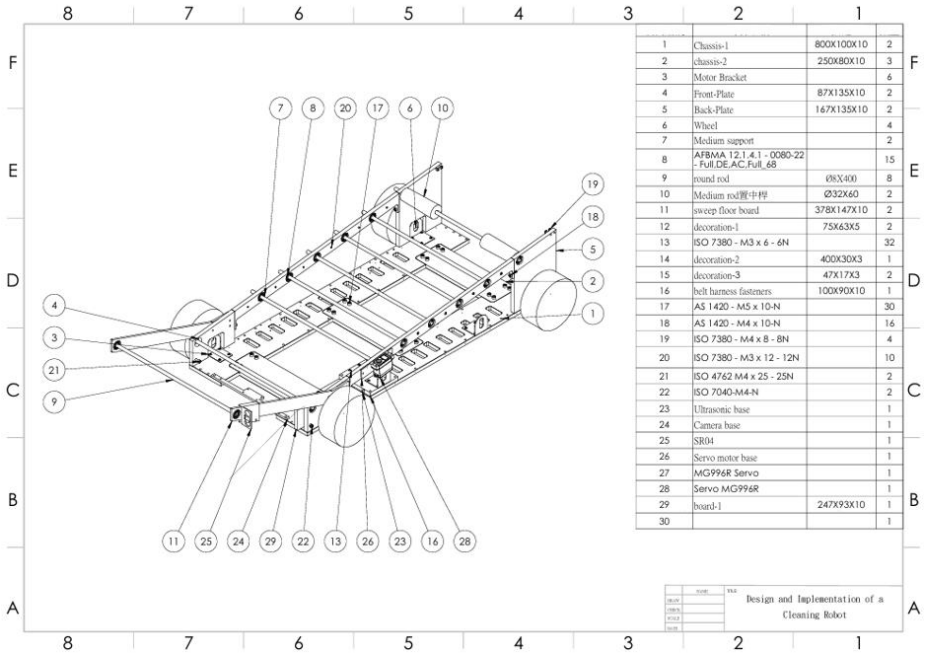

1	Chassis-1	800X100X10	2
2	chassis-2	250X80X10	3
3	Motor Bracket		6
4	Front-Plate	87X135X10	2
5	Back-Plate	167X135X10	2
6	Wheel		4
7	Medium support		2
8	AFBMA 12.1.4.1 - 0080-22 - Full,DE,AC,Full_68		15
9	round rod	Ø8X400	8
10	Medium rod两中焊	Ø32X60	2
11	sweep floor board	378X147X10	2
12	decoration-1	75X63X5	2
13	ISO 7380 - M3 x 6 - 6N		32
14	decoration-2	40DX30X3	1
15	decoration-3	47X17X3	2
16	belt harness fasteners	100X90X10	1
17	AS 1420 - M5 x 10-N		30
18	AS 1420 - M4 x 10-N		16
19	ISO 7380 - M4 x 8 - 8N		4
20	ISO 7380 - M3 x 12 - 12N		10
21	ISO 4762 M4 x 25 - 25N		2
22	ISO 7040-M4-N		2
23	Ultrasonic base		1
24	Camera base		1
25	SR04		1
26	Servo motor base		1
27	MG996R Servo		1
28	Servo MG996R		1
29	board-1	247X93X10	1
30			1

Figure 2. Cleaning robot structural parts diagram.

a) Chassis structure:

- Chassis-1 and Chassis-2: Chassis-1 serves as the two main support plates of the overall chassis structure, providing the foundation for the robot's main body. Chassis-2 acts as the connecting piece between the two main support plates, ensuring the stability and strength of the entire structure. The specific shapes and designs of Chassis-1 and Chassis-2 are shown in **Figure 3**.

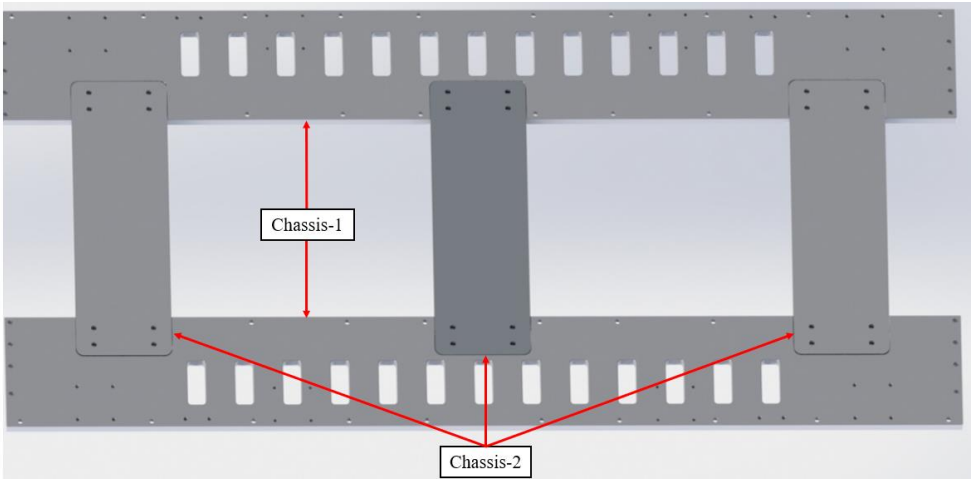

Figure 3. Chassis structure of cleaning robot.

- Front Side Plate and Rear: Side Plate: The front side plate primarily supports the conveyor belt's transmission structure by providing bearing support for the front roller, while also serving as the lower support for the garbage cleaning structure. The rear side plate serves as the rear bearing support for the conveyor belt's roller, ensuring the stability of the conveyor belt. The structures of the front and rear side plates are shown in **Figure 4**.

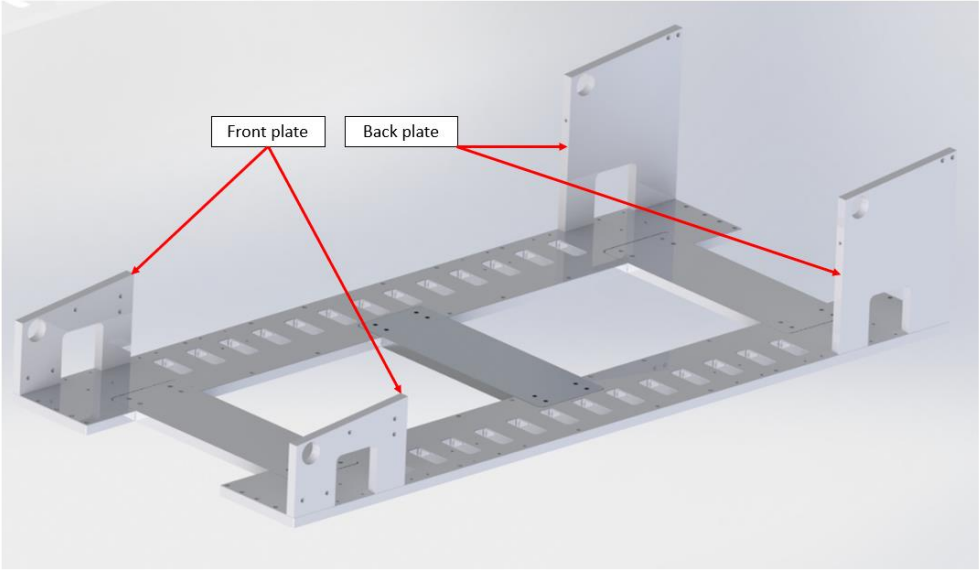

Figure 4. Chassis side panel structure of cleaning robot structure.

b) Garbage removal structure:

As shown in **Figure 5**, this component serves as the upper support frame of the cleaning structure. It has the dual functions of structural support and bearing positioning to ensure the stability and accuracy of the cleaning action.

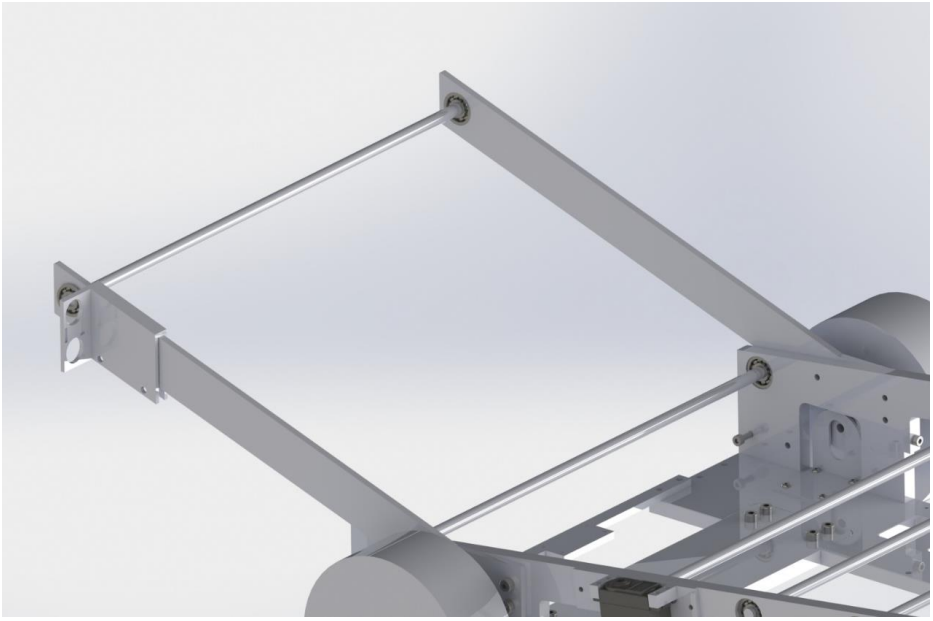

Figure 5. Garbage removal agency of cleaning robot.

c) Garbage conveying structure:

The core objective of the garbage conveyor structure design is to ensure that the cleaning robot can stably and efficiently transport collected waste to the storage area. This structure comprises bearings, rollers, support frames, and the conveyor belt's transmission system, with all components working cohesively to achieve optimal performance. Below is a detailed explanation of each component and the method for calculating the belt length.

Key Components and Design Features:

- Bearings and Rollers as Main Transmission Components:

The bearings and rollers are critical for stable and efficient garbage transport. Custom bearings tailored for the rollers were produced using 3D printing technology, ensuring precise fitting. This approach minimizes errors associated with traditional machining, resulting in a stable and reliable transmission system after assembly. The precision integration prevents looseness or misalignment during operation, maintaining high efficiency in waste transport.

- Middle Support for Structural Stability:

The middle support, which anchors the bearings, serves as a robust structural frame. Designed through rigorous mechanical calculations and careful material selection, the middle support possesses sufficient strength to bear the system's load and withstand the pressures of prolonged operation. This design prevents wobbling or deformation during transmission, ensuring smooth conveyor belt operation. The structural layout of the middle support is illustrated in **Figure 6**. This meticulous design not only extends the system's lifespan but also enhances overall operational efficiency.

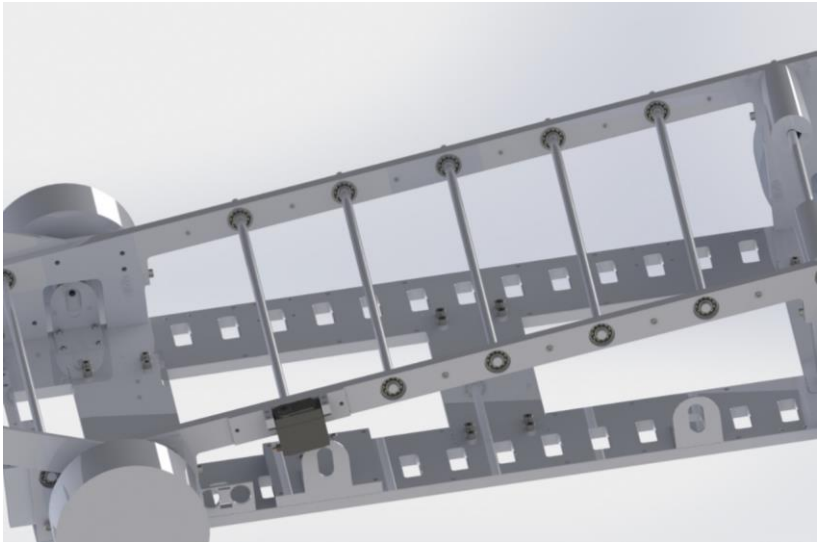

Figure 6. Waste hauling agency of cleaning robot.

To ensure smooth operation of the transmission structure, accurately calculating the belt length is crucial. Based on the geometric parameters of the pulleys and the structural requirements, the belt length can be calculated using the following equation:

$$\mathrm{L} = \frac{\pi}{2}(D + d) + 2C + \frac{(D - d)^2}{4C} \tag{1}$$

The total belt length (L) is a critical parameter in belt drive systems, influenced by several geometric factors. It is determined by three key variables: the center distance (C) between the two pulleys, the diameter of the larger pulley (D), and the diameter of the smaller pulley (d). These geometric variables collectively define the configuration and operational performance of the belt system, ensuring adequate tension and optimal power transmission efficiency. Accurate calculation and optimization of these parameters are crucial for achieving the desired mechanical efficiency and ensuring the longevity of the belt system.

2.2. Circuit design

Figure 7 illustrates the basic circuit design concept of the cleaning robot, while **Figure 8** depicts the wiring layout. To ensure stable motor control during operation, the L298N motor driver module is utilized. This module not only regulates current output but also stabilizes motor operation, enabling the cleaning robot to move reliably across various terrains and under changing loads. The system incorporates three L298N driver modules: two control the front and rear pairs of motors for smooth forward, backward, and turning motions, while the third manages peripheral devices.

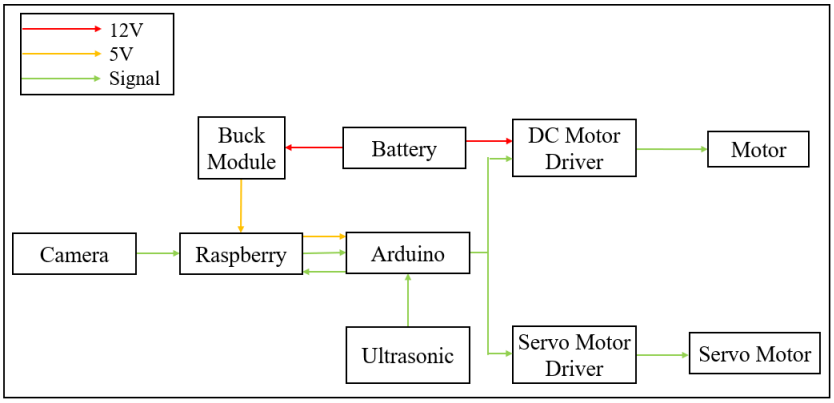

Figure 7. Electronic components integration diagram.

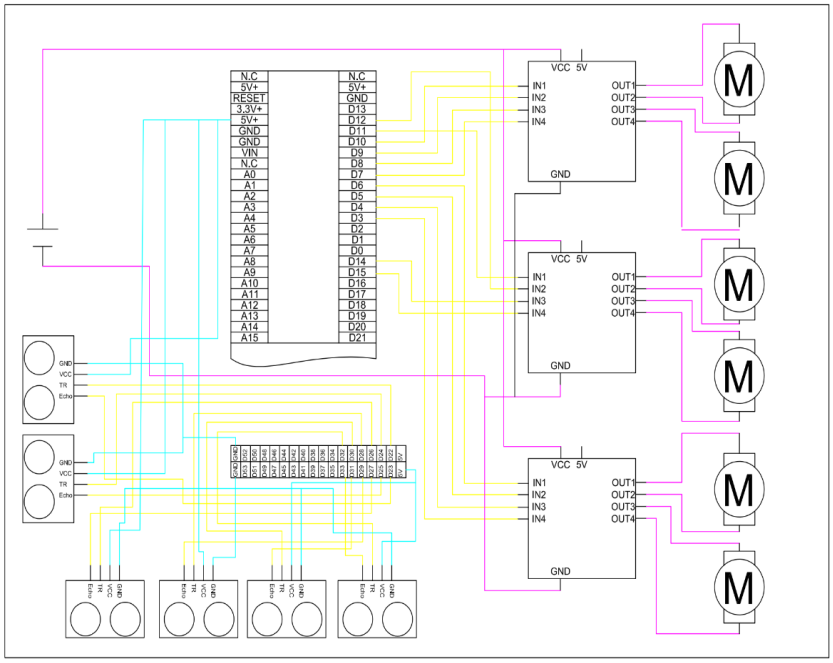

Figure 8. Wiring diagram of clean robot.

The trash sorting function is achieved using two servo motors, which transport waste into designated bins for recyclable and non-recyclable materials. The control system is centered around an Arduino Mega, which receives high-level commands from a Raspberry Pi. These commands regulate the L298N modules to drive the motors, ensuring precise control of movement direction and speed. This coordination enables the cleaning robot to navigate accurately to desired locations.

To support environmental sensing, the robot is equipped with multiple ultrasonic sensors, such as the SR04, for real-time monitoring of the surroundings. These sensors are strategically installed to measure distances between the robot and nearby obstacles, providing spatial data essential for collision avoidance during cleaning operations. The collected data is transmitted from the Arduino Mega to the Raspberry Pi via serial communication for further processing.

2.3. Software design

This section will explain in detail the software architecture design of the deep learning model training and garbage classification image detection and recognition used in YOLOv5 in the cleaning robot.

Deep learning model training

To enhance the accuracy of the waste classification system, a deep learning model was trained. A large dataset of waste images was first collected and annotated using the LabelImg tool, as shown in **Figure 9**. Features of waste objects in each image were precisely labeled. Following the annotation process, the labeled data was used to train the YOLOv5 model. Through iterative backpropagation, the model parameters were continuously adjusted during the training and validation phases to improve classification accuracy.

Figure 9. LabelImg tool feature circle selection.

Once the training process was completed, the optimized model was integrated into the system for real-time waste classification. This implementation ensures that the autonomous vehicle achieves reliable classification and tracking capabilities. The detailed workflow of the image training process is illustrated in **Figure 10**.

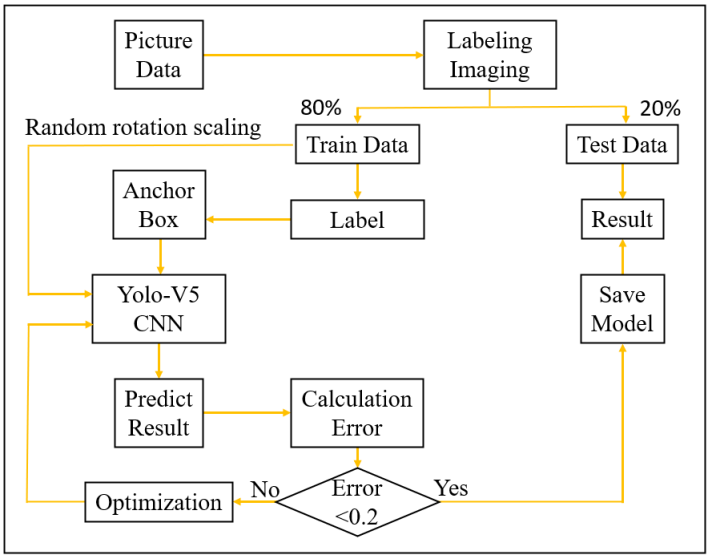

Figure 10. Garbage classification model training flow chart.

3. Implementation

This section discusses the development and experimental process of the cleaning robot, emphasizing the integration of autonomous vehicle control with image recognition for waste classification. The widely adopted YOLO algorithm is employed to ensure the efficient and precise detection and classification of objects, as illustrated in **Figure 11**.

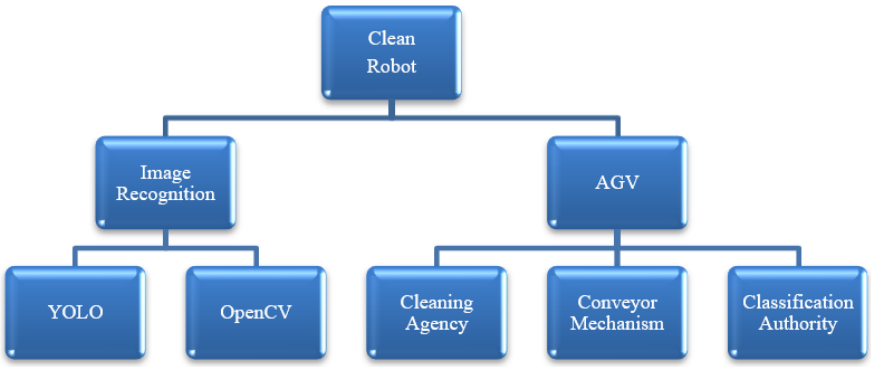

Figure 11. Cleaning robot research architecture diagram.

3.1. The autonomous vehicle system of a cleaning robot

The autonomous vehicle system of the cleaning robot is divided into three main mechanisms: the cleaning mechanism, the conveyor mechanism, and the sorting mechanism. Upon receiving commands from the Raspberry Pi, the instructions are parsed by the Arduino and sent to the respective mechanisms to execute the required actions and complete the task.

In the Raspberry Pi, Python is used to output control commands and collect distance data from the ultrasonic sensors, enhancing the robot's waste classification capabilities. The Raspberry Pi is also connected to a camera module, which captures image data of the cleaning area. Using image processing and deep learning algorithms, the robot identifies object features, determines whether the object is waste, and classifies it (e.g., aluminum foil, plastic bags, PET bottles, etc.). Based on the classification result, the Raspberry Pi sends control signals back to the Arduino to manage the subsequent actions.

This cleaning robot employs mecanum wheels, enabling six different movement modes: forward, backward, left and right translation, and left and right rotation. These movement modes facilitate the efficient navigation of the cleaning area, ensuring the effective removal of waste, as shown in **Figure 12**.

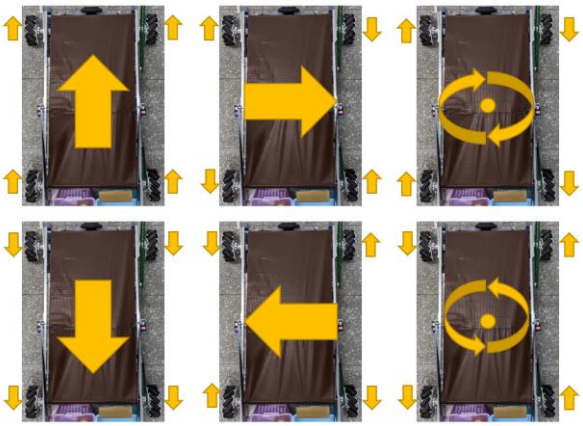

Figure 12. Sport mode of clean robot.

In the cleaning mechanism, in order to prevent the mechanism from blocking the camera's line of sight, this study uses a set of limit switches to position the cleaning mechanism so that it does not block the line of sight, as shown in **Figure 13**. When image recognition and tracking of objects are in progress, the cleaning mechanism will be positioned at a higher position without affecting the camera's recognition of the object to be tracked.

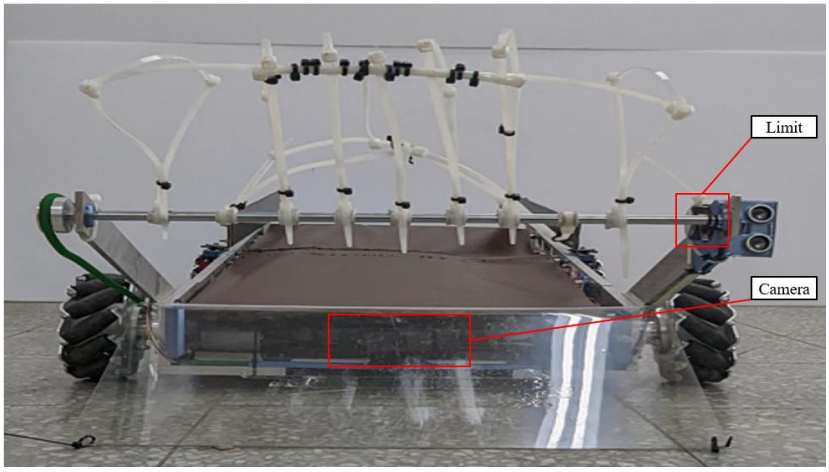

Figure 13. Use limit of clean robot.

In the cleaning robot, the conveyor belt and cleaning mechanism transmit power through the belt. As shown in **Figure 14**, the driving wheel is used to drive the belt and the driven wheel is rotated to drive the conveyor belt or cleaning mechanism to rotate, and the combination of the driving wheel and the driven wheel has a deceleration effect. This combination can optimize the speed of the conveyor belt and cleaning mechanism.

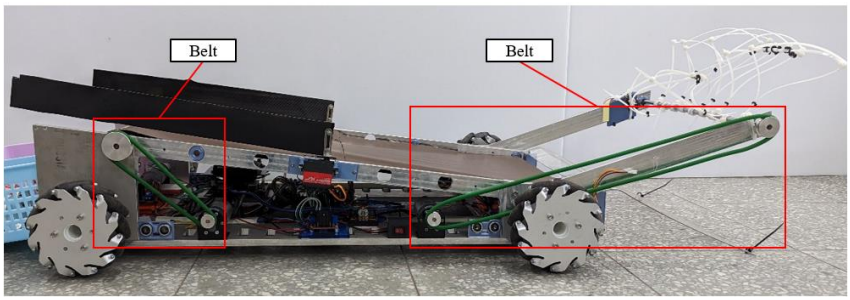

Figure 14. Cleaning robot belt drive mechanism.

After detecting the waste, this study designs two panels for sorting purposes. Upon identifying recyclable and non-recyclable waste, the system receives commands from the Arduino to activate two sets of servos, which perform the corresponding sorting actions. The waste is then directed by the panels into the appropriate collection bins, as shown in **Figure 15**.

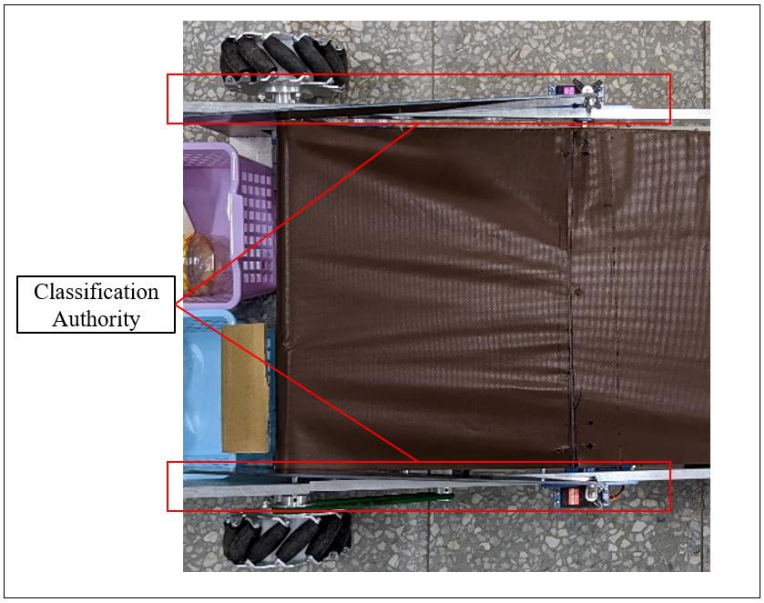

Figure 15. Cleaning robot classification mechanism.

3.2. Image recognition of cleaning robots

In the image recognition system, we use technologies such as YOLOv5 and Channel and Spatial Reliability Tracking (CSRT). With limited hardware resources, we use the advantages of software technology to achieve high efficiency and high-precision recognition purposes.

Among these two technologies, YOLOv5 combined with CSRT has the following advantages when applied to embedded equipment:

a) Efficient object detection and tracking:
- YOLOv5 is responsible for object detection with high accuracy.
- CSRT is responsible for target tracking, which has certain stability and reliability even if the target is blocked.

b) Resource optimization:
- Combined with the CSRT function, computing requirements are reduced.

- Since CSRT does not rely on the GPU during tracking, it effectively reduces resource requirements and improves recognition speed.

c) Good ability to adapt to scenes:
- YOLOv5 can quickly identify objects in the first scene and is suitable for a variety of scenes.
- CSRT has been tested on YOLOv5 and can provide stable single object tracking.

d) Open source and ease of use:
- YOLOv5 has quite a lot of open-source materials that can be used for reference.
- CSRT does not rely on additional special equipment and is easy to use on limited equipment.

The garbage classification image detection module plays a core role in the self-cleaning vehicle system, identifying and locating garbage objects through real-time image analysis and tracking. The overall system process is shown in **Figure 16**.

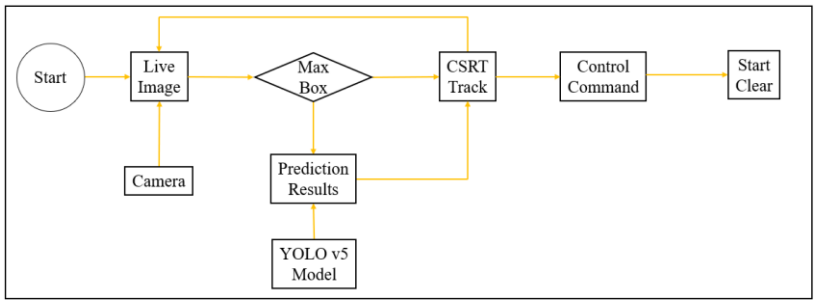

Figure 16. Garbage classification image detection and recognition.

a) Capture real-time images: When the system is turned on, the camera starts first and continues to capture real-time images of the scene for subsequent image identification and tracking. The real-time image capture function ensures that the system can update the image in real time, allowing subsequent model calculations to perform garbage detection based on the latest visual information.

b) Import YOLOv5 for prediction: Each captured image frame is imported into the YOLOv5 deep learning model for object prediction. YOLOv5 has high-performance real-time object detection capabilities, which can quickly locate various objects in images and predict their classification. This model has been trained on a large number of garbage images, so it can accurately identify the type of garbage.

c) Confidence level screening: In the prediction results of YOLOv5, the system gives a confidence level for the prediction of each object. If the confidence level is higher than 0.8, the system determines that the object is garbage. Setting this confidence level threshold is intended to improve the reliability of detection and reduce the occurrence of misjudgments, thereby preventing self-propelled vehicles from tracking irrelevant objects and improving classification accuracy.

d) Switch to CSRT tracking: For objects judged to be garbage, the system will enable the CSRT tracking method. CSRT is an efficient and accurate object tracking algorithm that can stably track objects in captured images. CSRT is

particularly good at tracking fast-moving or partially obscured objects, and has good anti-noise capabilities, making it suitable for garbage tracking in dynamic scenes when autonomous vehicles are running. CSRT's tracking framework uses spatial and channel reliability to ensure that the target object is continuously positioned accurately, even if the target is slightly deformed or occluded. Therefore, when YOLO detects the maximum confidence level w, h of an object, the parameters are imported into CSRT to track the position of the object in the image.

e) Control the Arduino self-propelled vehicle module: The system determines the relative position of the garbage based on the CSRT tracking results, and generates corresponding control signals to send to the Arduino self-propelled vehicle module. The self-propelled vehicle module then automatically adjusts the direction, steering angle and moving speed based on the image position of the target object in order to accurately approach and locate the area where the garbage is located. When the self-propelled vehicle completes its positioning, it starts the cleaning function and transfers the garbage to the garbage collection module.

In the test samples, as shown in **Figure 17**, YOLOv5 successfully identified multiple types of objects, accurately drawing bounding boxes around each one, while also labeling each object with its class name and predicted confidence score. The model effectively handles objects of different shapes, sizes, and colors. Even in cases of partial occlusion or complex backgrounds, it maintained a high level of recognition accuracy.

Figure 17. YOLOv5 target detection results display.

4. Experiment

This section presents the hardware configuration and experimental results of the cleaning robot. The experiment utilized a camera, ultrasonic sensors, motors, Arduino Mega 2560, and Raspberry Pi 4. The results demonstrate that the robot successfully employed YOLOv5 for waste detection and integrated CSRT for object tracking and classification.

4.1. Hardware configuration

The specifications of the hardware equipment used in this experiment are shown in **Table 1**, and the cleaning robot result is shown in **Figure 18**.

Table 1. cleaning robot hardware specifications.

Material Component	Specification	Quantity
Camera	Logitech C922 pro	1
Ultrasound	HC-SR04	2
Motor	DC12 V 110 rpm	6
Battery	12 V LiPo	1
Buck Module	DC to DC 75 W (12 V to 5 V)	1
Arduino Mega 2560	Microcontroller: ATmega2560 Working voltage: 5 V Input voltage: 6–20 V	1
Raspberry Pi 4	CPU: Broadcom BCM2711 Cortex-A72 1.5 GHz RAM: 4G GPU: VideoCore VI	1
L298N	Driving voltage: 5 V~35 V Drive current: 2 A Max power: 25 W	3

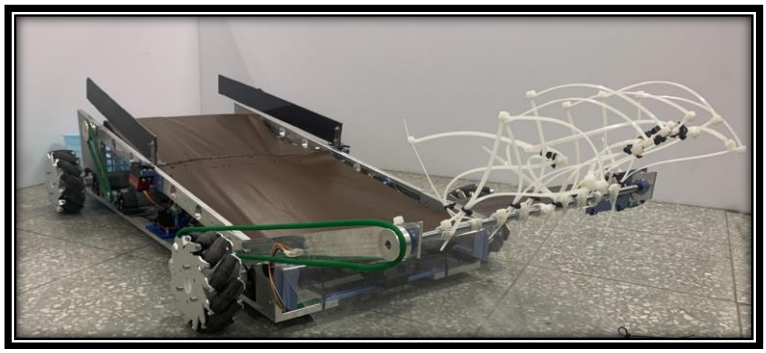

Figure 18. Cleaning robot results.

4.2. Experimental results

The experimental results of the cleaning robot are primarily analyzed from three aspects: waste detection, waste classification, and cleaning efficiency. First, in waste detection, the cleaning robot uses the YOLOv5 model to identify waste objects. In the tests, the detection showed high accuracy for objects with clear shapes and distinct features (such as plastic bottles and metal cans). However, for irregularly shaped or deformed waste (such as crumpled packaging paper), the detection accuracy slightly decreased. **Figure 19** presents the results of the waste detection, with green boxes clearly indicating the successfully detected and identified waste objects.

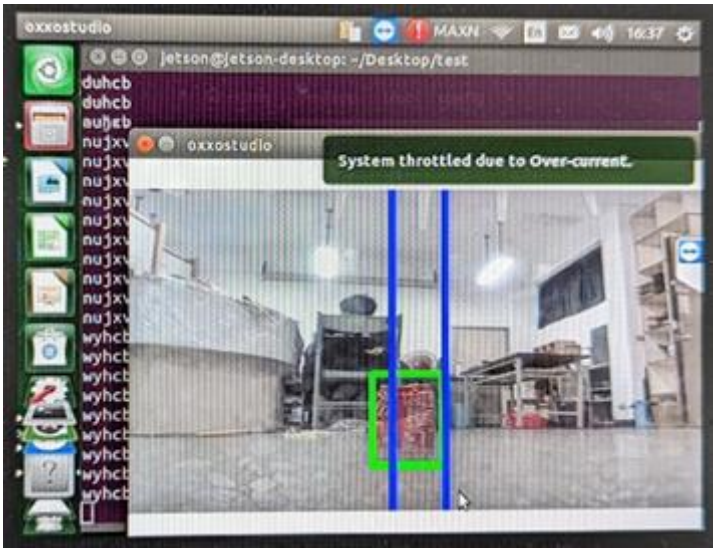

Figure 19. The cleaning robot uses YOLOv5 for object detection (green box).

To enhance cleaning efficiency, the system employs the CSRT function for efficient object tracking after waste detection. Once the YOLOv5 model completes the detection, the detection box data is fed into the CSRT algorithm for real-time tracking. **Figure 20** shows the tracking results, with yellow boxes representing stable tracking of the target objects using CSRT, demonstrating the system's ability to handle dynamic scenarios effectively.

Figure 20. Schematic diagram of cleaning robot tracking using CSRT (yellow box).

In terms of waste classification and handling, the cleaning robot accurately classifies the waste and places it into the corresponding recycling bins based on the recognition results from the YOLOv5 model, as shown in **Figure 21**. The entire cleaning and classification process not only verifies the accuracy and efficiency of the robot system but also highlights its potential for practical applications.

Figure 21. Schematic diagram of a cleaning robot recycling garbage.

The following summarizes the accuracy and efficiency of the experiment in practical applications based on waste detection accuracy, cleaning efficiency, and waste classification and handling results.

Waste detection accuracy:

- For objects with clear shapes and distinct features, the detection accuracy was 95%.
- For irregularly shaped or deformed waste, the detection accuracy was 85%.

Cleaning efficiency:

- The number of waste objects that can be detected and tracked per hour is 50.
- The real-time tracking success rate of the CSRT algorithm was 92%.

Waste classification and handling:

- Based on the recognition results from the YOLOv5 model, the waste classification accuracy reached 90%.
- The accuracy of placing the classified waste into the corresponding recycling bins was 88%.

Although the detection accuracy for irregular or deformed waste is 85%, possible solutions include integrating additional sensors, such as depth cameras, to improve the detection of irregularly shaped waste. Additionally, enhancing the image recognition model by using more diverse training data can increase the system's ability to identify non-standard items. In terms of adaptability to various environments, besides the robot's mechanical design allowing agile movement in different settings, robust control can be introduced to the robot's control system to enhance its adaptability in various environments. Finally, for the robot's energy usage, the future consideration of using both batteries and solar power can improve the use of sustainable energy.

5. Conclusion

This study successfully designed and implemented a cleaning robot that integrates mechanical, electronic, and AI software systems, achieving automated waste detection and classification. The mechanical structure is constructed from CNC machined 6061 aluminum alloy, providing the necessary strength, precision, and durability for stable operation in diverse environments. The circuit system, centered

around the Arduino Mega microcontroller and the L298N motor driver module, ensures reliable coordination between the drive motors, sensors, and actuators.

The AI software system utilizes YOLOv5 for object detection, combined with CSRT for real-time tracking, demonstrating excellent performance in waste recognition and classification. Experimental results show that the robot achieves high accuracy in detecting various types of waste and exhibits stable classification capabilities. Additionally, the use of mecanum wheels enables multiple movement modes, further enhancing the robot's operational flexibility.

In conclusion, the cleaning robot developed in this study holds significant potential for waste management applications, offering a scalable and efficient automated solution for both cleaning and sorting. Future research will focus on optimizing the system's computational efficiency, expanding its application to more complex environments, and integrating sustainable energy sources to maximize its environmental benefits.

Author contributions: Conceptualization, YHC and SYP; methodology, YHC and SYP; software, SYP; validation, YHC and SYP; formal analysis, YHC and SYP; investigation, YHC and SYP; resources, YHC; data curation, YHC and SYP; writing—original draft preparation, YHC and SYP; writing—review and editing, YHC; visualization, YHC and SYP; supervision, YHC; project administration, YHC and SYP; funding acquisition, YHC. All authors have read and agreed to the published version of the manuscript.

Conflict of interest: The authors declare no conflict of interest.

References

1. Canedo D, Fonseca P, Georgieva P, et al. A Deep Learning-Based Dirt Detection Computer Vision System for Floor-Cleaning Robots with Improved Data Collection. Technologies. 2021; 9(4): 94. doi: 10.3390/technologies9040094
2. Malik M, Sharma S, Uddin M, et al. Waste Classification for Sustainable Development Using Image Recognition with Deep Learning Neural Network Models. Sustainability. 2022; 14(12): 7222. doi: 10.3390/su14127222
3. Feng H, Mu G, Zhong S, et al. Benchmark Analysis of YOLO Performance on Edge Intelligence Devices. Cryptography. 2022; 6(2): 16. doi: 10.3390/cryptography6020016
4. Shin DJ, Kim JJ. A Deep Learning Framework Performance Evaluation to Use YOLO in Nvidia Jetson Platform. Applied Sciences. 2022; 12(8): 3734. doi: 10.3390/app12083734
5. Wu W, Liu H, Li L, et al. Application of local fully Convolutional Neural Network combined with YOLO v5 algorithm in small target detection of remote sensing image. Lv H, ed. PLOS ONE. 2021; 16(10): e0259283. doi: 10.1371/journal.pone.0259283
6. Dang C, Wang Z, He Y, et al. The Accelerated Inference of a Novel Optimized YOLOv5-LITE on Low-Power Devices for Railway Track Damage Detection. IEEE Access. 2023; 11: 134846-134865. doi: 10.1109/access.2023.3334973
7. Gams M, Gu IYH, Härmä A, et al. Artificial intelligence and ambient intelligence. Journal of Ambient Intelligence and Smart Environments. 2019; 11(1): 71-86. doi: 10.3233/ais-180508
8. Huang Q. Towards Indoor Suctionable Object Classification and Recycling: Developing a Lightweight AI Model for Robot Vacuum Cleaners. Applied Sciences. 2023; 13(18): 10031. doi: 10.3390/app131810031
9. Miao X, Lee HS, Kang BY. Multi-Cleaning Robots Using Cleaning Distribution Method Based on Map Decomposition in Large Environments. IEEE Access. 2020; 8: 97873-97889. doi: 10.1109/access.2020.2997095
10. Kopytko V, Shevchuk L, et al. Smart Home and Artificial Intelligence as Environment for the Implementation of New Technologies. Path of Science. 2018; 4(9): 2007-2012. doi: 10.22178/pos.38-2

11. Yin J, Apuroop KGS, Tamilselvam YK, et al. Table Cleaning Task by Human Support Robot Using Deep Learning Technique. Sensors. 2020; 20(6): 1698. doi: 10.3390/s20061698
12. Narkhede P, Walambe R, Mandaokar S, et al. Gas Detection and Identification Using Multimodal Artificial Intelligence Based Sensor Fusion. Applied System Innovation. 2021; 4(1): 3. doi: 10.3390/asi4010003
13. Mistry SK, Chatterjee S, Verma AK, et al. Drone-vs-Bird: Drone Detection Using YOLOv7 with CSRT Tracker. IEEE; 2023.
14. Kwon KR, Lee SH, Farkhodov K. Object Tracking using CSRT Tracker and RCNN. In: Proceedings of the 13th International Joint Conference on Biomedical Engineering Systems and Technologies; 2020.
15. Lin YW, Chiu CF, Chen LH, et al. Real-Time Dynamic Intelligent Image Recognition and Tracking System for Rockfall Disasters. Journal of Imaging. 2024; 10(4): 78. doi: 10.3390/jimaging10040078
16. Vega J, Cañas JM. PyBoKids: An Innovative Python-Based Educational Framework Using Real and Simulated Arduino Robots. Electronics. 2019; 8(8): 899. doi: 10.3390/electronics8080899
17. Spector L. Evolution of artificial intelligence. Artificial Intelligence. 2006; 170(18): 1251-1253. doi: 10.1016/j.artint.2006.10.009
18. Strautiņa S, Kalniņa I, Kaufmane E, et al. RaspberrySet: Dataset of Annotated Raspberry Images for Object Detection. Data. 2023; 8(5): 86. doi: 10.3390/data8050086
19. Hirakawa S, Mori S, Kaneda M. A Navigation and Object Detection Method Using Multisensory Fusion for a Cleaning Robot. IEEE Robotics and Automation Letters. 2020; 5(4): 6609-6616.
20. Vasquez D, Lopez J. Detecting Different Objects in an Industrial Scenario Using Deep Learning with YOLOv4. Procedia CIRP. 2021; 99: 207-212. doi: 10.1016/j.procir.2021.01.064
21. Liu D, Chen X, Guo Z, et al. Research on the Online Parameter Identification Method of Train Driving Dynamic Model. International Journal of Computational Vision and Robotics. 2022; 1(1): 497-509.
22. Jiang Y, Yin S. Heterogenous-view occluded expression data recognition based on cycle-consistent adversarial network and K-SVD dictionary learning under intelligent cooperative robot environment. Computer Science and Information Systems. 2023; 20(4): 1869-1883. doi: 10.2298/csis221228034j

Mechanical Engineering Advances 2025, 3(1), 2098.
https://doi.org/10.59400/mea2098

Review

Research progress on thermal comfort evaluation in vehicle cab

Yuanyuan Fu, Bin Zhao*

School of Mechanical Engineering, Liaoning petrochemical University, Fushun 113001, China
*** Corresponding author:** Bin Zhao, zbzbz0203288@163.com

CITATION

Fu Y, Zhao B. Research progress on thermal comfort evaluation in vehicle cab. Mechanical Engineering Advances. 2025; 3(1): 2098. https://doi.org/10.59400/mea2098

ARTICLE INFO

Received: 20 November 2024
Accepted: 6 January 2025
Available online: 22 January 2025

Abstract: In order to improve thermal comfort of vehicle cab, reduce driver fatigue and further improve work efficiency, researches on thermal comfort of vehicle cab are summarized. Research background of thermal comfort for vehicle cab is analyzed. And then related research progress on thermal environment in vehicle cab is studied from aspect of time and space, and thermal environment inside and outside vehicle are compared. Affecting factors of thermal comfort in vehicle cab are discussed in depth, which conclude thermophysical parameters, human physiological factors, clothing thermal resistance and other secondary factors. And thermal comfort evaluation indexes are analyzed in depth. Evaluation methods of thermal comfort in uniform environment are analyzed, related experimental research and theoretical analysis are summarized, and it also points out some problems in thermal comfort of vehicle at this stage, and also gives corresponding solutions. The future trend of thermal comfort of vehicle cab is predicted. Analysis results can provide theoretical guidance for optimization design of air conditioning supply parameters and structural parameters, and has significant meaning of improving thermal comfort of vehicle cab.

Keywords: thermal environment; thermal comfort; thermal model

1. Research background

With the development of the economy, the number of cars has increased rapidly, according to relevant data, as of the end of 2022, the China's car ownership was about 131 million units. By the end of 2023, China's car ownership had reached 280 million. But in addition to the convenience that people enjoy the car brings, it also causes a lot of problems. For example, (1) due to excessive heating in summer or too cold in winter, excessive use of air conditioning consumes huge energy, so the method of district heating in the car and personalized heating method can be used to solve the problem of huge energy consumption; (2) at the same time, because traditional cars use gasoline as the power raw material, the increase in car ownership is bound to lead to an increase in demand for oil resources, and at the same time, car travel will emit a large number of pollutants, and will also bring huge pollution to the environment. Therefore, research on thermal environment and comfort in the automobile cabin is also an important key topic for energy conservation and emission reduction. Therefore, the emergence of new energy vehicles can effectively solve this problem [1].

Development prospects of new energy vehicles are also very impressive. According to the 2019 Electric Vehicle Outlook Report released by Bloomberg New Energy Finance, it is estimated that by 2040, there will be 548 million electric vehicles worldwide, accounting for about 32% of the global passenger car number by then; (3) there is also no meeting thermal comfort of the driver in the car, for

example, due to the cold temperature in the car in winter, the human hands and feet are cold, which affects the speed of hitting the steering wheel and the speed of pressing the brake, thereby increasing the traffic accident rate. In the car interior, people are in an environment with light, sound and heat, so the comfort of heat, light and sound will affect the comprehensive comfort of the human body. Among them, in the single factor of human comfort research, the earliest and most concerned is thermal environment, thermal environment to provide people with thermal comfort, but also to the greatest extent to affect the energy consumption of the entire system, so this article focuses on the impact of thermal comfort on the human body, but does not mean that sound, light, and pressure have no effect on the human body in the car [2,3]. A good thermal comfort environment can also relieve driver fatigue, improve their irritability, and thus better concentrate and ensure driving safety [4,5]; (4) finally, because the car body material is thin-walled steel, the specific heat capacity of the material is very small, so that the heat insulation and heat storage capacity of the car is poor, so thermal environment inside the car is greatly affected by the external environment, in real life due to the owner's negligence, the pet left in the car resulting in summer high temperature death is common. At the same time, the high temperature in the car after receiving sun exposure in the static state will not only bring strong thermal shock to the occupants, but also the excessive temperature in the car is easy to bring about the aging of internal items, spontaneous combustion of the interior items, explosion and other hazards [6]. This further demonstrates the importance of studying interior temperature regulation controllers, which are currently poorly studied. (5) thermal environment inside the car will also affect the defrosting and defogging effect of the window surface, which greatly affects the driver's driving vision, resulting in unnecessary traffic accidents. Therefore, research on thermal comfort of automobiles based on the above five points is necessary and extremely important, which has also attracted the attention of international scholars.

Main contribution is to study research progress on analysis and evaluation of thermal environment of vehicle cabins. By analyzing existing research results, the main research directions for thermal comfort of vehicle cabins are proposed to improve the reliability of research on thermal comfort of vehicle cabins. This is conducive to proposing more effective measures for thermal comfort of vehicle cabins, thereby improving thermal comfort of drivers.

2. Progress on thermal environment analysis in vehicle cab

From the first chapter, it can be seen that based on the popularity of vehicles in people's lives, research on thermal environment of cockpit has received more and more attention. During the driving of the car, especially in summer, cockpit is often uncomfortable for people to ride for a long time in a complex thermal environment [7]. Therefore, research on thermal environment of the car cabin has also attracted the attention of international scholars. Since the 70s of the last century, developed countries in Europe and America have begun to concern problem of thermal smoothness and thermal comfort of passenger compartment [8]. A good thermal environment in the car is of great significance to the driver's driving experience and driving safety, the cockpit is overheated, and the driver is easy to feel sleepy; Over

cooling of cockpit can also reduce the agility of driver. thermal environment in cabin is not only important for the driver's driving safety, but also for the driving experience of the passengers. Poor thermal environment in the car can also cause nausea, vomiting and other adverse physical health conditions of passengers. Airflow organization in the cockpit of a passenger car is one of the factors that affect thermal environment in the cabin, which in turn affects thermal comfort level in the cabin [9]. Therefore, improving the airflow organization in the car has also effectively improved human comfort, which is beneficial to human health and can also achieve energy-saving effects. Many well-known car companies are also studying ways to enhance thermal comfort of human body by adjusting airflow organization in the cabin (adjusting parameters air outlet temperature, outlet speed and relative humidity, changing airflow distribution in the space) [10]. Airflow organization is used in field of thermal comfort, and poor airflow organization in cabin causing problems such as uneven temperature distribution, which reduces thermal comfort level of passenger car cockpits [11]. Relevant literature knows that there are relevant requirements for thermal comfort of the cockpit: during cooling process of the cockpit of a passenger car in summer, the airflow velocity around the occupants is not easy to exceed 0.5 m/s, and the airflow velocity in this range can make the occupants have a slight feeling of blowing wind, and will not make the occupants feel uncomfortable [12]. Mean temperature in cabin is 22 ℃–28 ℃, and occupants will be satisfied with thermal environment in the cabin in this temperature range [13]. When the average cabin temperature is below 22 ℃, the occupants will feel cold; when the temperature is greater than 28 ℃, the crew will feel that thermal environment in cabin is muggy [14]. Temperature difference between cabin inside and outside cabin in China is generally 8 ℃–10 ℃, when ambient temperature is high, temperature difference can be appropriately amplified to 10 ℃–12 ℃, and the appropriate temperature difference inside and outside cabin will make the occupants have a good riding experience [15]. All these fully illustrate the important role of studying thermal environment in the car interior on human comfort. This section addresses two aspects. The first section explains thermal environment in the car from the perspective of time and space. The second section compares thermal environment inside and outside car. Vehicle thermal environment analysis is complex and multiple dimensional, which relating to temperature, humidity, velocity and other factors, two aspects of this section conclude thermal analysis from aspect of time and space, and comparative analysis of thermal environment inside and outside car.

2.1. Analysis from perspective of space

Thermal environment includes the steady-state thermal environment and transient thermal environment from perspective of time, and analysis includes uniform thermal environment and non-uniform thermal environment from the spatial perspective. In summer heat, the cockpit turns on the air conditioning, and the physical activity most closely related to cockpit thermal environment is heat transfer. There are five ways of heat transfer: heat conduction, heat convection, heat radiation sweating and heat loss, and it is precisely because of the use of car air conditioning and the dynamic influence of weather that thermal environment inside the car is

uneven and transient [16]. Therefore, unlike indoor buildings that use a steady-state and uniform thermal environment, interior of a car is an unsteady state and a non-uniform thermal environment based on the above characteristics. When the early researchers did not have perfect research methods, scholars from various countries analyzed thermal environment of the car cabin through numerical simulation and modeling [17].

Chien et al. [18] used numerical simulation to analyze and simulate the temperature field and flow conditions in the cabin of the automobile, and also analyzed the cooling cycle and coupling heat transfer on top, bottom and two sides of cabin, and studied the direct effect of the heat flux of the automobile air conditioning system, body maintenance structure, and the heat dissipation factors of human body on the "heat-flow" field. Influence of multiple factors on the flow field inside the cabin was analyzed. However, it did not study external climatic conditions as influencing factors. Zhang [19] conducted an internal flow field analysis on the three-dimensional model of the carriage under manned and unmanned conditions, and compared with experimental results, it was found that maximum error of numerical simulation was concentrated in the head area of the human body. Based on simulation of flow field in car, Che [20] analyzed the influence of the gap between the seat and the door on the flow field characteristics in passenger compartment.

Lu et al. [21] used computational fluid dynamics to simulate and analyze flow field in the passenger compartment of a heavy goods vehicle, and adopted the equivalent temperature evaluation standard for thermal comfort of the personnel in the vehicle, and results showed that uneven distribution of air volume in each air duct will make the airflow organization of the internal flow field of the car unreasonable, thereby reducing thermal comfort of the personnel in the vehicle. Kilic et al. [22] studied temperature and humidity features of various positions under the two working conditions of air conditioning heating and cooling in car cabin, and preliminarily discussed influence of thermal environment on the skin temperature and thermal sensation of occupants. Alahmer et al. [23] studied the overall and local thermal sensation and thermal comfort of human body under different humidity through experiment and numerical simulation, and experimental and simulation results showed that relative humidity controlled by air conditioning system in the heating and cooling process (winter and summer conditions respectively) reached human comfort zone faster than when relative humidity was not controlled, but the humidity had less influence on thermal comfort of human body in steady-state stage, and the measured temperature and the simulated temperature were compared. Results show that most significant influence of humidity on temperature and occupant thermal sensation is at the beginning of refrigeration, and when the humidity value tends to be stable, the effect is not obvious.

Myoung et al. [24] studied the quantitative energy-saving effect of local air conditioning system, and analyzed thermal comfort in cabin from different angles by adjusting the front and top air supply ratio, air supply temperature, air supply speed, etc. Lai et al. [25] studied the influence of uniformity of airflow at air outlet of automobile air conditioning on thermal environment of the cockpit, and found that when the air flow of the air outlet is uniform, cooling effect of cockpit is relatively good, flow field and temperature distribution in cabin are also relatively uniform,

and thermal comfort level of the occupants is relatively good. Zhang et al. [26] carried out numerical simulation of the three-dimensional flow field and thermal environment in a certain car, obtained the distribution of speed field, temperature field, PMV and PPD, however PMV and PPD cannot suit for cars, and calculated the distribution of air age in the passenger compartment. Moon et al. [27] compared and analyzed the two thermal comfort evaluation indicators of PMV-PPD and equivalent temperature under multi-band and single-spectrum radiation models, and the results showed that considering effect of multi-band solar radiation, temperature near driver and passenger increased by 1 ℃–2 ℃, and equivalent temperature can predict the local change of thermal comfort level in passenger compartment.

Wang et al. [28] carried out climate experiments in Turpan to analyze climatic characteristics and study the changing characteristics of thermal environment of local automobiles under different climatic conditions, so as to provide experimental basis for research and development of automotive products in the dry heat environment of Turpan. Danca et al. [29] measured temperature and speed at various locations in the passenger compartment and calculated PMV-PPD thermal comfort evaluation indicators. However, PMV-PDD can only be used as evaluation index for building, which is not suit for cars. Giri et al. [30] applied CFD software to study two-dimensional ventilation of the cockpit in the parking stage, and studied thermal comfort of cockpit through analysis of the two-dimensional temperature field and speed field of the cockpit, and found that the air circulation in the cabin was improved with increase of air outlet speed, and temperature field distribution of cockpit tended to be uniform with increase of air outlet velocity, and heat accumulation and ventilation problems in the cabin were also greatly improved. He [31] studied influence of various crowd densities on thermal environment of cabin, evaluated thermal environment of cabin based on PMV, compared airflow velocity and occupant thermal comfort in the cabin with different crowd density, and the results showed that the different crowd density had a greater impact on thermal comfort of the cabin, which changed with the change of crowd density.

Mohammad et al. [32] conducted on-site measurements of three cars with different front windshield insulation rates, monitored the changes of thermal environment in car and dynamic thermal response of occupants, and studied effect of changes in characteristics of front windshield on thermal comfort inside the car under solar radiation. Experimental results show that improving heat insulation rate of front windshield can better improve thermal environment in car and reduce intensity of thermal shock when the occupants enter the car during the heating stage. However, in the cooling stage, due to air conditioning and cooling, improvement of heat insulation rate of the front windshield has less effect on improvement of thermal environment and thermal comfort in the car. Lü et al. [33] studied influence of the angle of the air outlet grille on thermal comfort of cockpit in extreme thermal environment, and analyzed the temperature field and speed field of the cockpit by optimizing and analyzing parameters of the air duct grille, and found that adjusting the parameters of the style grille can avoid the phenomenon of poor heat dissipation caused by the speed dead zone.

Zhong et al. [34] carried out modal behaviors and stochastic dynamics analysis of a composite cabin-like combined structure, and studied effect of aero-thermal

factor on dynamic characteristics of combined structure. Riaz et al. [35] designed and installed an air-conditioned cabin on a tractor, and carried out experiment to valuate installed cabin performance under two scenarios concluding, conventional (S–I) and enhanced (S-II) air distribution. Meshing of air-conditioned cabin is illustrated in **Figure 1**, simulation results are illustrated in **Figure 2**.

Figure 1. Diagram of meshing of the air-conditioned cabin.

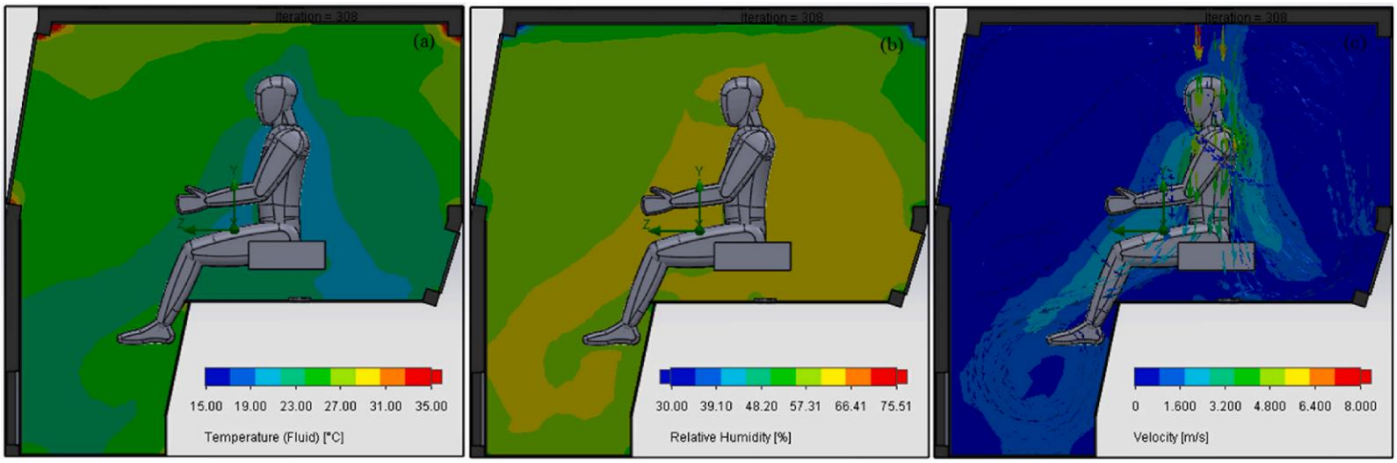

(a) **(b)** **(c)**

Figure 2. CFD simulation results of cross sectional view of the tractor cabin: **(a)** Temperature; **(b)** relative humidity; **(c)** velocity. 10^4[K]

Hadi et al. [36] studied effect of solar intensity at different angles on air temperature inside a parking car based on CFD simulation. Temperature distributions at car center plane for various solar angles were shown in **Figure 3**. Due to thermal boundary layer, air temperature near heated inner surface is higher than that far away. Velocity distribution at car center plane for various solar angles is shown in **Figure 4**.

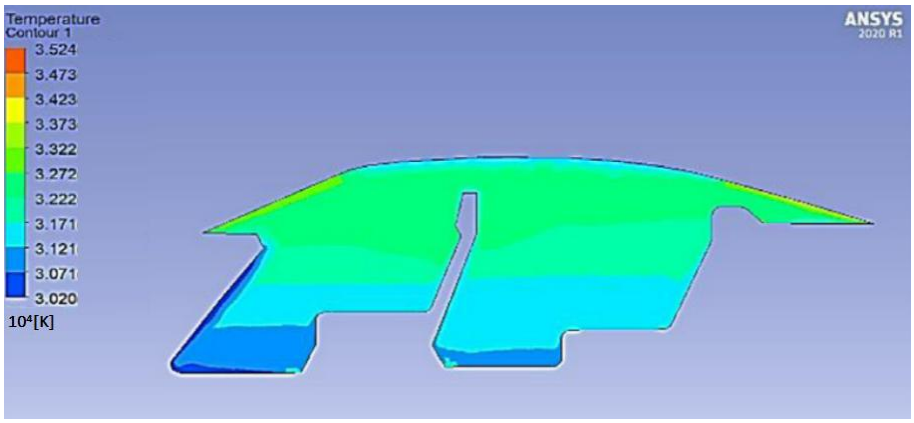

(a) 54°

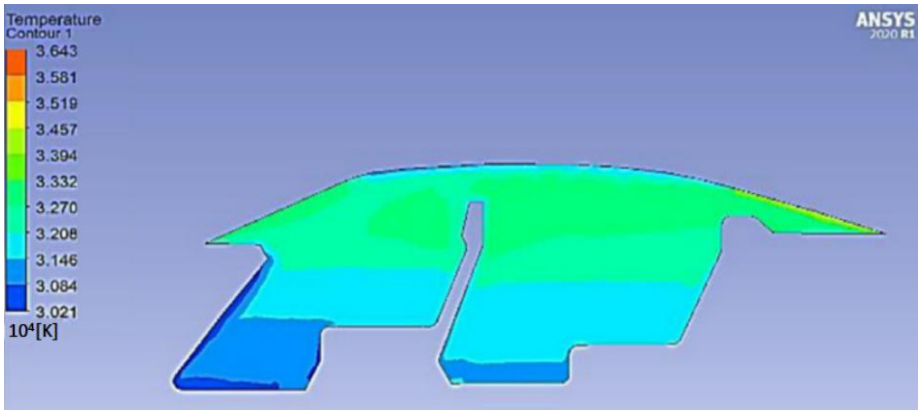

(b) −54°

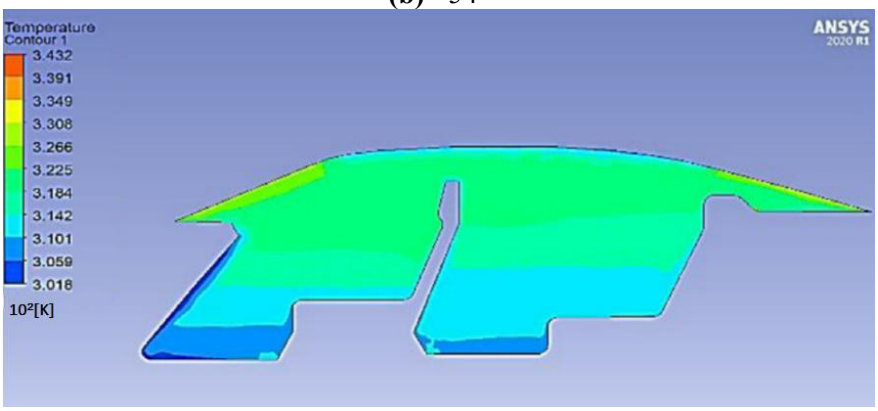

(c) 63°

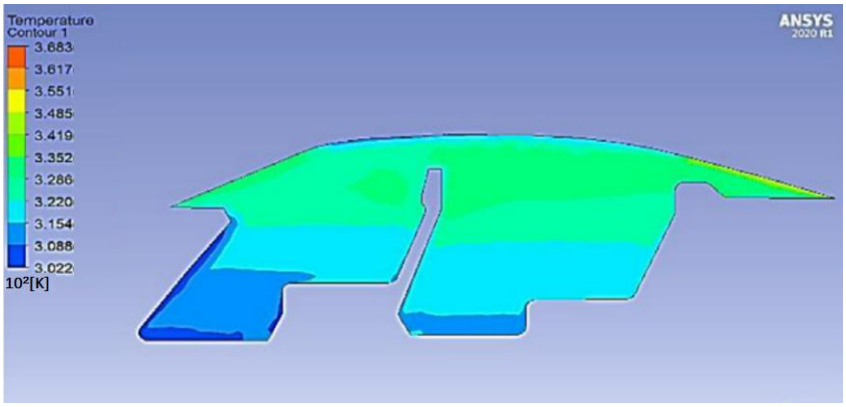

(d) −63°

Figure 3. Temperature contours at car center plane for different solar angles.

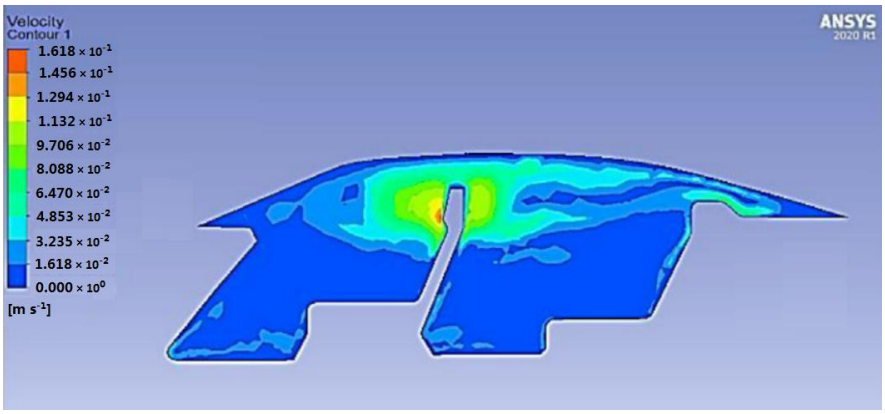

(a) 54°

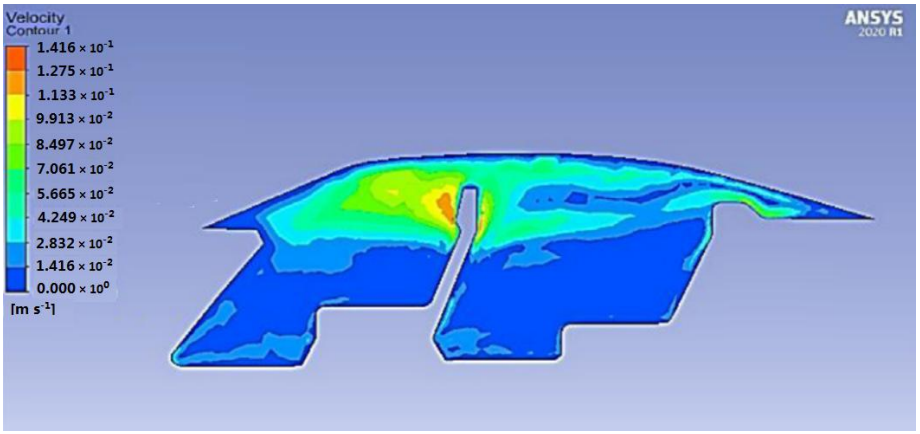

(b) −54°

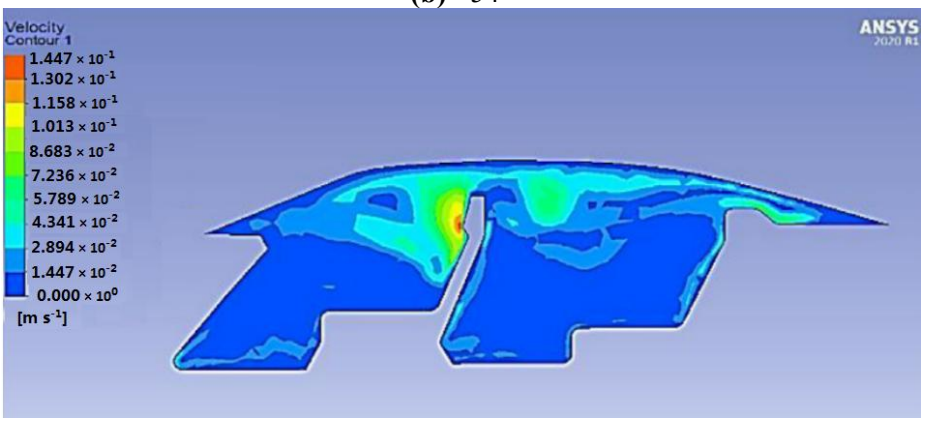

(c) 72°

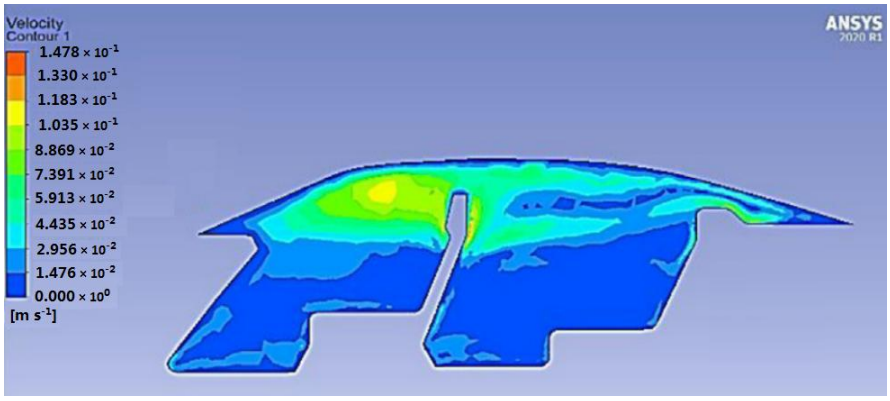

(d) −72°

Figure 4. Velocity distribution at car center plane for various solar angles.

Wang et al. [37] carried out numerical analysis for a partitioned heat transfer wall setting of high-speed train cabin, and obtained average deviation of the airflow velocity and temperature respectively. Analysis results showed vortices in seating area, a significant longitudinal airflow and an increasing temperature near the carriage ends. Compartment's thermal environment and the acceptance of airflow were further analyzed. Longitudinal section airflow temperature fields of high-speed train cabin were shown in **Figure 5**. there is a significant temperature heterogeneity along the longitudinal direction of the cabin, with an overall low temperature in the middle and a high temperature at ends. Longitudinal section airflow velocity fields of high-speed train cabin were shown in **Figure 6**. The exhaust air influences the end airflow, so the longitudinal airflow is quite noticeable, and this longitudinal airflow may bring about the diffusion of pollutants.

As seen from existing research achievements, thermal comfort analysis of vehicle cab from aspect of time and space has been studied by many scientists, main research focuses on influence of season, weather, time (such as morning and evening, daytime), and vehicle driving status (such as stationary, driving) on the thermal comfort of drivers in terms of cabin air temperature and humidity. Following limitations are summarized:

(1) Numerical computing method is main means of analyzing thermal environment of vehicle, current numerical methods ignore natural convection heat transfer of airflow, which cause big analysis error.

(2) Experimental verification is an important means of ensuring correctness and reliability of thermal environmental analysis, however limitation of experimental conditions can cause incorrectness of analysis results.

(3) Thermal environmental analysis of vehicle is affected by many outer factors, such as temperature, wind velocity, these factors often change randomly, which are difficult to be controlled. Further exploration is needed to investigate the impact of the coupled effects of multiple factors in the driver's cabin on their thermal comfort.

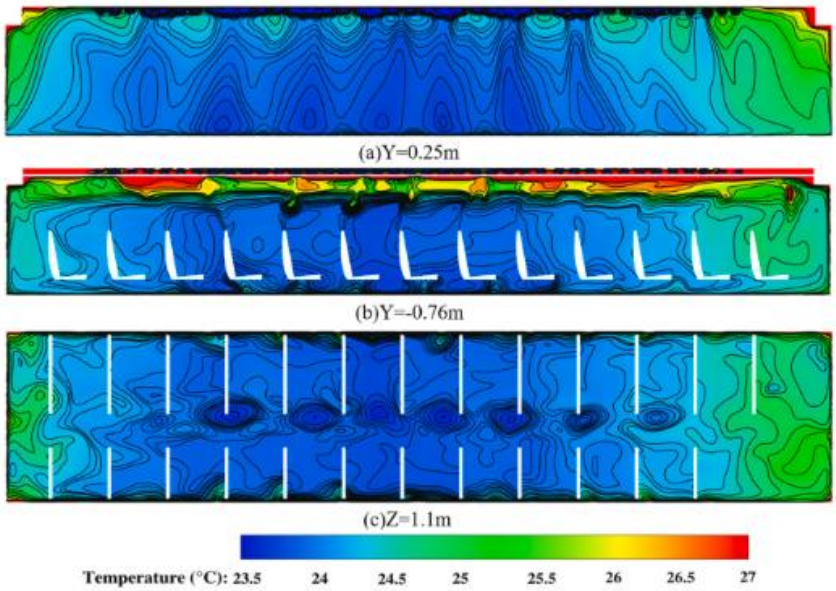

Figure 5. Longitudinal section airflow temperature fields of high-speed train cabin.

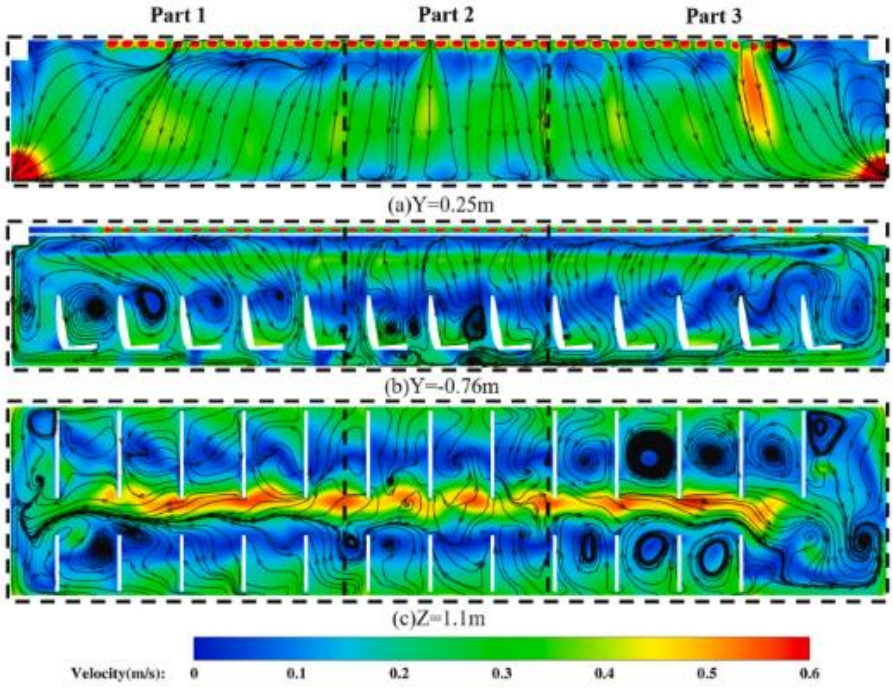

Figure 6. Longitudinal section airflow velocity fields of high-speed train cabin.

2.2. Comparative analysis of thermal environment inside and outside the vehicle focusing on solar radiation

Thermal environments inside and outside vehicles are two completely different systems, which have unique characteristics and influencing factors. Changes in temperature outside vehicle should be concerned for better regulating temperature inside and improve driving comfort. Comparative analysis of thermal environment inside and outside the vehicle is summarized.

Early studies are all about thermal environment inside the car, mainly studying thermophysical parameters that affect human thermal comfort, such as air temperature, relative humidity, average radiation temperature, relative air speed, etc. As well as two separate but related parameters, on the one hand, the level of activity provided by metabolism. On the other hand, it is thermal resistance of clothing. Zhou et al. [38] conducted a test of human thermal comfort under bus driving conditions, and conducted tests under indoor and outdoor parking conditions for convenience comparison. The study concluded that automotive thermal comfort studies should be conducted under transient conditions, with a good correlation between average skin temperature and average thermal sensation.

Yi et al. [39] applied a cooling film in solar spectra and high emissivity in atmospheric window, and measured inside air temperatures. Solar irradiation and heat transfer through two boxes were illustrated in **Figure 7**.

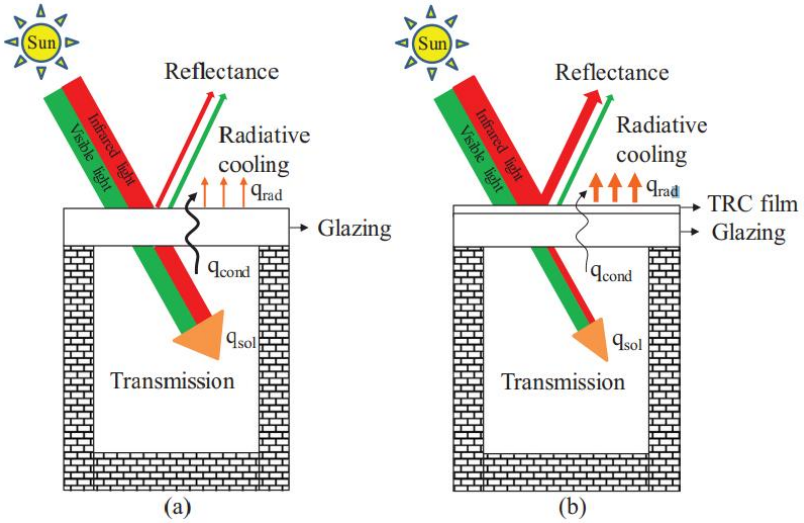

Figure 7. Solar irradiation and heat transfer through the two boxes: **(a)** silica glazing; **(b)** transparent cooling film covered glazing.

Chaiyapinunt et al. [40] studied influence of solar radiation on thermal comfort for a person near a glass window. Thermal comfort of a person is evaluated. Setiyo et al. [41] studied features of solar cells-based cabin cooler system, results showed that car cabin cooler can decrease cabin temperature by 9.8 ℃. Vehicle cab is considered to be contaminated with high condition of compounds [42]. Especially in the high temperature environments of summer, it is observed that internal parts of vehicle cause more air pollutants and influence people's health [43].

Levinson et al. [44] measured the immersion temperature of two housing vehicles with high and low solar reflectance and found that solar radiation caused increased load on vehicles with low solar reflectance. Bhavsar et al. [45] grasped temperature changes in cabin of a closed vehicle under sunlight for 150 min. This environment is uncomfortable for passengers and can lead to suffocation until vehicle is completely ventilated. Some scientists analyzed thermal environment of cockpit under solar radiation and no solar radiation, and used PMV-PPD to evaluate thermal environment. PMV is not suitable for cars.

Yang et al. [46] studied human thermal comfort needs with standing and treadmill workstations based on experiment, results showed that temperature changing from 20 to 26 ℃ could meet most occupants. Zhang et al. [47] established CPMV* index based on CPMV model, considering solar diffusion coefficient, which further improved the accuracy of thermal environment evaluation model under solar radiation conditions. Huang et al. [48] sorted out and compared 8 thermal sensory evaluation indicators and models under effect of solar radiation effects, and proposed a SC-PMV model, which is analogous to outdoor comprehensive air temperature, which regards solar radiation as a component of air temperature, and calculates and analyzes the measured data in Lhasa in winter, and finds that the SC-PMV model has good predictability. Yang et al. [49] of Tongji University used a combination of experiment and numerical simulation to study thermal comfort of the cockpit, and studied that the solar altitude angle and solar radiation intensity have a great influence on thermal comfort level of the cockpit, and found that the temperature in the cabin increased with the increase of solar radiation, indicating that solar radiation

intensity has an important effect on thermal comfort.

Hirn et al. [50] studied effect of radiation intensity and wavelength on cockpit thermal comfort, results shows that solar radiation has a great effect on thermal comfort. The above is a comparative analysis of thermal environment inside and outside the car, but there is little research on the interior wall of the car, but in fact, multiple walls in the cabin have an important effect on thermal comfort. Second, although thermal environment in the car cabin has been extensively studied, there are still some problems. If there is no comparative analysis of thermal environment in the car when parking and driving. Failed to relate wall temperature to space temperature field. Considering the quantitative effect of automotive window glass materials on the ability to absorb sunlight, it has little quantitative effect on thermal environment inside the car. Regarding the latest progress of windshields, Kong [51] and others of Chongqing University studied the influence of thermal insulation rate of the front windshield on thermal comfort level of the cockpit, and carried out the test of three different thermal insulation coefficients of glass on thermal environment of the cockpit and the dynamic thermal response of the occupants, and found that improving thermal insulation coefficient of the front windshield can improve thermal environment of the cabin in the warming stage and improve thermal comfort level of the cockpit. Zhang et al. [52] studied the influence of characteristics of the window on thermal environment of cockpit, and analyzed effect of various heat conduction methods on temperature in the cockpit, and the results showed that influence of solar radiation on thermal environment in cockpit was relatively large, different types of glass had different transmittance, the transmittance had a greater impact on thermal comfort of cockpit, and the absorption rate of the glass surface had little effect on the cockpit.

There is no reference to the measurement techniques used to evaluate microclimate conditions in cars compared to buildings. Cars are heterogeneous environments where no single microclimatic parameter can be deemed homogeneous. This is particularly true for mean radiant temperature, which necessitates specialized instruments for accurate evaluation.

According to existing achievements, research trend of thermal environment inside and outside vehicle cab mainly reflects in equal emphasis on health and comfort, application of intelligent technology, integration of thermal management systems, and adaptability to extreme weather conditions. These trends will drive continuous development and innovation of automotive industry, providing drivers with safer, more comfortable, and environmentally friendly travel experiences. Vehicle climate measurement technology uses a series of sensors and control systems to measure and adjust real-time parameters such as temperature, humidity, and air quality inside the car, creating a comfortable and healthy riding environment. With the continuous development of technology, future car climate measurement systems will become more intelligent, integrated, and environmentally friendly, providing passengers with a more comfortable and healthy riding environment.

3. Factors influencing thermal comfort in car

Factors effecting thermal comfort can be divided into thermophysical

parameters and human physiology, psychological factors and clothing thermal resistance. Among them, human physiology, psychology and clothing thermal resistance are independent but interrelated. The thermophysical parameters contain four aspects: air temperature, humidity, air velocity, and mean radiation temperature.

3.1. Thermophysical parameters

(1) Air temperature

Temperature inside the car is the main indicator of thermal environment and main factor affecting thermal comfort, which directly affects the heat exchange between human body and air through convection and radiation, air temperature is affected by the heat transfer by radiation (transparent and opaque walls), not vice versa [53]. When ambient temperature rises, perspiration increases, and subjective thermal sensation will be biased towards the direction of heat.

(2) Relative humidity

Past studies have shown that relative humidity of the air has little influence on human thermal comfort at 30%–70% [54]. Therefore, the influence of air humidity has often been overlooked in previous studies of passenger compartment thermal comfort. But in fact, air humidity directly or indirectly affects thermal comfort. Zhang et al. [55] studied effect of different driving states on thermal comfort of occupants, and results showed that different driving states influence temperature distribution in cabin, and relative humidity of the cockpit also changes relative. Air humidity also affects the moisture diffusion of the skin and the balance of the body's energy metabolism. MO et al. [56] study influence of relative humidity in passenger compartment on human thermal comfort based on PMV-PPD. Results illustrate that when cabin air temperature is fixed, the relative humidity change will cause the change of human heat, and the higher cabin temperature, the more obvious influence of relative humidity on thermal comfort.

(3) Air velocity

Air velocity affects thermal comfort of human body by affecting convective heat transfer and air evaporation. Experimental studies that different wind speeds have significant differences in human body temperature, and under low temperature conditions, wind speed increases, human body temperature decreases, and the greater wind velocity, the lower body temperature [57].

(4) Average radiation temperature

Ambient radiation temperature inside the car includes solar radiation and heat exchange between human body and interior surface of car in form of radiation. Zhang [58] of Jilin University pointed out in study of thermal environment of automobile space that the temperature of the part of the car exposed to direct sunlight can be as high as 90 ℃ or more in summer under solar radiation heat transfer, Wang Weijian also verified through experiments that the air temperature in the car can quickly rise to 60 ℃–70 ℃ when exposed to the sun for 30 min.

3.2. Human physiological factors

Human body has a self-regulating function and can cope with various thermal conditions. When people move from a warm environment to a cold environment,

body will be suit for new environment through a series of complex physiological processes, including vasoconstriction, shivering. At the same time, heat transfer between human body and thermal environment is also a complex. The human thermoregulatory system dynamically responds to its environment, keeping body's main temperature.

The physiological model of the human body concludes two parts: passive system and active system. Passive systems describe heat transfer to human body and its surfaces. The rate of thermoregulation reaction depends on the actual deviation of the core temperature and skin temperature from the set temperature. The classification of human thermoregulation models takes into account single-node, two-node, multi-node, 3D models with up to thousands of nodes [59,60]. At the present only these models can be considered suitable for cars: 3D models like: JOS-3 model, but it has been validated on naked subjects, but it has been validated on naked subjects, open source is developed [61]. Fiala Ergonsim model, but it is not a free software. THERMODE 2023, specifically designed to account for microclimatic inhomogeneities (potentially suitable for cars), provided with a thermal sensation model [62] and UCB model [63].

3.3. Clothing thermal resistance

Clothing also plays a very important role in human heat comfort by keeping warm and slowing down the evaporation and diffusion of sweat on the body surface in the heat exchange of the human body. Zhang et al. [64] studied the influence of clothing resistance and activity level on thermal comfort level of the cabin based on PMV evaluation indicators, and the results showed that clothing resistance and thermal comfort of clothing had a related effect, resulting in different perceptions of thermal environment of the occupants. Common winter clothing thermal resistance is shown in **Table 1**.

Table 1. Common winter clothing thermal resistance.

Clothing	Thermal resistance/clo
sweater	0.28
Regular long sleeve	0.25
Down jacket	0.55
Regular pants	0.10

Regular pants 0.10 The current calculation of clothing thermal resistance is often a warm body dummy as a test tool, and there are generally three models: parallel model, serial model and global model. These three types of calculation methods use different calculation methods due to different modes of application. Both the parallel model and the serial model are related to the local thermal resistance of the garment. The total thermal resistance of the garment is the weighted average of the local thermal resistance of each region. Among them, the parallel model is the reciprocal of the sum of the reciprocal thermal resistance weights of each segment, and the serial model first finds the local thermal resistance of each segment of the dummy, and then weights thermal resistance value of the clothing.

Table 2 selects several typical dummies for analysis from the development process of various warm body dummies, and summarizes whether they can test the local thermal resistance of clothing.

Table 2. Various types of warm body dummys and their characteristics.

Year	Name	Dummy type	Country	Key character	Whether thermal resistance of clothing can be tested
1942	SAM	Cell segment dummy	United States	It does not reflect the temperature distribution characteristics of the human body.	No
1969	The first generation of warm body dummy improvement	Non-sweating manikin	United States	Simulated sweating is realized by spraying water heating of the fabric covered by the surface of the dummy, but it is limited by the experimenter's different experience of spraying water and heating time, which is not very accurate and has poor repeatability, but it provides ideas for the future development of dummy simulation sweating.	No
2002	Walter	Sweating manikin	China	Improved two-part test method, using one-step test, the world's first simultaneous test of thermal resistance and wet resistance [61].	Yes
2011	Newton	Sweating manikin	United States	Separately control heating and sweating in the first interval, which is more commercial [62].	Yes

Effect of body movements and air action on the clothing's thermophysical properties as described in ISO 9920 should be considered. When human body is in motion, thermal resistance of clothing decreases due to an increase in convective heat dissipation. Air action during human movement on thermal properties of clothing is multifaceted, including increased convective heat dissipation, changes in the air layer under clothing, sweat evaporation and humidity regulation, as well as the influence of clothing materials and structure. These factors work together to determine the insulation and breathability of clothing during human movement.

3.4. Other secondary factors

There are also factors that are widely believed to affect a person's thermal comfort, including age, gender, race, region, etc. [65,66]. The basic metabolic rate of people body will gradually decrease with age, but evaporation rate of sweat on skin also decreases with age, which is reflected in the heat balance equation for the human body's heat production and heat dissipation to reduce simultaneously, so the part affected by age cancels each other. The relationship between gender and human comfort has been studied and analyzed by many scholars.

Fabbri et al. [67] analyzed thermal comfort in kindergarten environment of 4- and 5-year-olds. Experiments have shown that children can clearly distinguish thermal comfort and can express their thermal sensation in terms of thermal comfort, and under same conditions, children have higher PMV than adults.

Li et al. [68] conducted experimental studies on more than 28,000 subjects from different climatic regions in China, and more than 500 subjects conducted simulated climatic conditions in the laboratory. The experimental results show that the same thermal comfort value means different things to people in different climatic regions, so thermal comfort standard needs to be divided by region.

4. Thermal comfort evaluation index

At present, most of thermal comfort evaluation models are suitable for the construction field, that is, suitable for steady-state, uniform indoor thermal environment. Li et al. [69] will conduct detailed research on the authoritative standards currently applied to thermal comfort evaluation in buildings, clarify the scope of application and evaluation accuracy of each standard, and clearly classify and organize the standards and performance evaluation. The study concludes the future development trend of human thermal comfort and advantages and disadvantages of thermal comfort evaluation standards, which provides a theoretical basis for the use of thermal comfort evaluation in China's building environment [70].

However, for automobile unsteady state, the evaluation index research of non-uniform thermal environment is relatively late compared with the development of the construction field. In this paper, different thermal comfort evaluation methods will be explained from two aspects: uniform thermal environment and non-uniform thermal environment. Among them, there are 4 uniform thermal environment evaluation indicators. They are PMV-PPD evaluation method, effective temperature ET evaluation index, and standard effective temperature SET evaluation index. There are three evaluation indicators for the comfort of non-uniform thermal environment. They are weighted PMV index, equivalent temperature EQT evaluation method and equivalent temperature EHT evaluation method. Common evaluation indicators are illustrated in **Table 3**.

Table 3. Thermal environment comfort evaluation indicators.

Evaluation index	Founder	Limitations
PMV-PPD	Fanger	Non-uniform thermal environments cannot be evaluated
Weighting PMV	Matsunagc Ingcrsoll	Weights do not accurately reflect the impact of this factor on overall comfort
EQT	SAE J2234-2001	Overall thermal comfort cannot be evaluated, AEQT metrics are required
EHT	Wyon	Overall thermal comfort cannot be evaluated
TSV	UC-Bcrkclcy	It is necessary to use warm body dummy experiments, which are costly

4.1. Evaluation method of thermal comfort in uniform thermal environment

(1) ASHRAE seven-point scale subjective evaluation method ASHRAE seven-point scale evaluation method is a subjective thermal comfort evaluation model, which divides the body's thermal sensation of thermal environment into 7 levels of heat (+3), warm (+2), slightly warm (+1), neutral (0), slightly cool (−1), cool (−2) and cold (−3), as shown in **Table 4**, by organizing a certain number of evaluators to make 7 according to their own thermal sensation of the evaluation target is evaluated in one of the grades, and finally thermal comfort of target under different operating conditions is obtained.

At the same time, Santos Silva et al. evaluated and analyzed the low-speed and high-speed models according to ASHRAE Standard 55 to obtain different long-term

indices [71]. Simulation experiments are used to show that different indicators can lead to different results, but the trend is not much different. The subjective evaluation method is suitable for both steady and transient conditions, which is applied for both overall thermal comfort evaluation and local thermal comfort evaluation of the human body, but the method has greater subjectivity, and its evaluation results will be largely affected by the evaluators' own reasonable judgment of thermal comfort, and must face the real thermal environment, so it is difficult to apply to thermal comfort research work in the automobile development stage.

Table 4. Subjective evaluation index of human thermal sensation.

	Bedford	**ASHRAE**	**Gagge & Hardy**
1	cold	cold	comfortable
2	cool	cool	Slight comfort
3	Comfortable and cool	slight	uncomfortable
4	Neutral comfort	neutral	Very uncomfortable
5	Cozy and warm	Mild warmth	
6	warm	warm	
7	hot	hot	

(2) PMV-PPD evaluation method

Human thermal comfort equation and the ASHRAE seven-point scale as the starting point were taken, and curved and analyzed thermal sensory data under the four metabolic rates were obtained by the subjective sensory test conducted, and PMV-PPD thermal comfort evaluation system was obtained. PPD indicator is defined as percentage of people who are dissatisfied with thermal environment. Therefore, its value ranges between 0 and 1, and the lower the value, the more people are satisfied with thermal environment. This method comprehensively considers six factors: human activity, clothing thermal resistance, air temperature, average radiation temperature, air flow rate and relative air temperature. Corresponding to the ASHRAE temperature sensing range, the indexing of PMV, as illustrated in **Table 5**, PMV indicates feeling of heat and cold in vast majority of people in same hot environment, using a total of 7 stages of comfort evaluation from −3 (cold feeling) ~ 0 (intermediate feeling) ~ +3 (heat feeling). The correlation between PMV and PPD populations and predicted average turnout is shown in **Figure 8** [72].

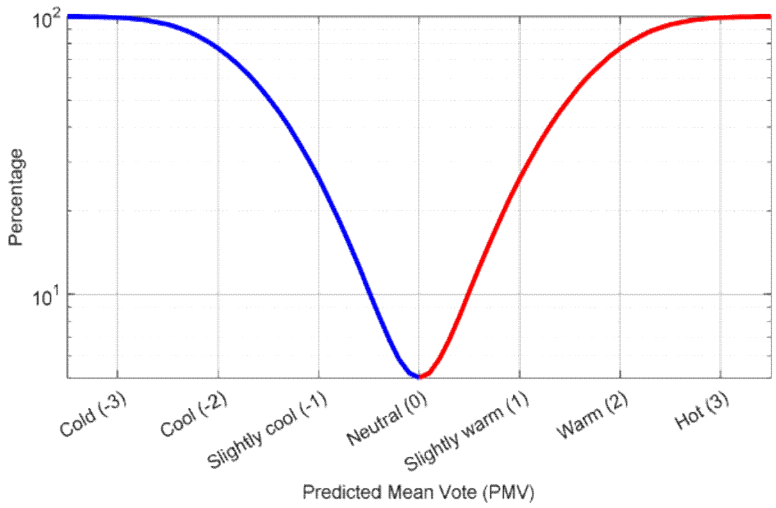

Figure 8. Correlation between PVD prediction average turnout.

Table 5. PMV thermal comfort index.

Thermal sensation	Hot	Warm	Slightly warm	Neural	Slightly cool	Cool	Cold
PMV	+3	+2	+1	0	−1	−2	−3

Human thermal comfort equation and PMV-PPD evaluation index have always been the theoretical basis of international research on human thermal comfort, and have been widely used by ISO 7730 as indoor thermal environment comfort evaluation index. Zhang [73] found that PMV can be used correctly to predict thermal comfort of car. Thermal environment in a mobile car is uneven due to rapid changes in solar radiation and an uneven air temperature. Therefore, there are four shortcomings in the PMV-PPD evaluation method: Because theory is based on test results in thermal environment close to human comfort zone, and the non-test area is predicted by formula, the use of this index in environment far from the comfort zone will obtain inaccurate conclusions; The method does not consider the influence of regional, age and sex differences, but many scholars believe that differences in metabolism due to differences in sex and age, and different regional climates will also cause people's adaptability to thermal environment and different psychological expectations, which all lead to the limitations of the method. The method is an overall evaluation method of thermal environment, the parameters used in the PMV index are some average quantities, such as treating people as a whole, taking the average of the temperature and pressure around the human body, M and W are also averaged, this simplification is suitable for a uniform thermal environment with a large space, and local thermal comfort problem of occupants that is common in non-uniform thermal environment of car seating space is not applicable; This method is a steady-state thermal comfort evaluation method, which is not applicable to transient environments in the car, such as air conditioning refrigeration and heating processes.

Although PMV indicators have been widely used in building thermal comfort assessment, their application in vehicle environments is limited. Main reason is that internal environment of a vehicle is a highly uneven and non-stationary environment and interior space of the vehicle is relatively small. Therefore, in the assessment of

vehicle thermal comfort, multiple factors such as passenger expectations, individual differences, environmental parameters, etc. need to be comprehensively considered to provide more accurate and reliable evaluation results.

(3) Effective temperature (ET) evaluation index Effective temperature (ET) human body thermal comfort evaluation index comprehensively considers the influence of dry bulb temperature, humidity and air flow rate on human thermal comfort, it is numerically equal to the temperature of static saturated air that produces the same feeling, this index has been used by HVAC engineers in the field of building environment for nearly 50 years, but because this indicator overemphasizes the influence of humidity at low temperatures, and the influence of humidity at high temperatures is not emphasized enough. It caused the inherent defects of the effective temperature index and was gradually replaced by a new effective temperature index [74].

(4) Standard effective temperature (SET) evaluation index

SET is defined as the subject's wearing standard clothing (clothing thermal resistance of 0.6clo) in a thermal environment, and subject's average skin temperature and skin temperature are same as thermal resistance of a certain real thermal environment and clothing of the actual clothing. It is believed that human body has same amount of heat dissipation in standard thermal environment and the actual thermal environment.

(5) Thermoregulation model JOS-3

Thermoregulation models that accurately consider factors such as clothing, sweating, and microclimatic variations should be concerned. Some scientists developed a thermoregulation model JOS-3 based on JOS-2. Human physiological responses and body temperatures are calculated using the backward difference method. JOS-3 has a higher accuracy for heat production in young and older subjects and mean skin temperature in older subjects than JOS-2 under cold environmental conditions.

4.2. Evaluation of comfort in non-uniform thermal environment

(1) Weighted PMV index Weighting

There are two weighting methods for PMV indicators. Including equivalent temperature weighting and body segment area weighting, it is an evaluation method for weighted average of environmental parameters in non-uniform environment in PMV indexes and then referring to PMV, but the weight of thermal comfort in local parts of human body to the overall thermal comfort of human body cannot be accurately obtained, and Han et al. [75] used weighted PMV for main evaluation parameters of human thermal comfort in non-uniform thermal environment. The index and the weight value of the local heat sensitivity of the human body to overall heat sensitivity studied by Crawshaw et al. [76] analyzed the influence of different distribution of air return outlets in the car on human thermal comfort.

(2) Equivalent temperature (EQT) evaluation method

Equivalent temperature EQT index refers to an ideal space environment with a relative humidity of 50%, when real ambient temperature and heat dissipation of a certain part of the dummy's body are equal, air temperature is defined as equivalent

temperature of the part [77]. Equivalent temperature considers air temperature, air velocity and radiation influence, divides the human body into 15 segments. Human effective radiation area coefficient is listed in **Table 6**.

Table 6. Human effective radiation area coefficient.

	Fanger	**Guibert&Taylor**
Sitting position	0.70	0.70
Standing posture	0.72	0.78
Semi-vertical posture	-	0.72

(3) Equivalent uniform temperature (EHT) evaluation method

Huang et al. [78] proposed equivalent uniform temperature (EHT). First set an ideal uniform environment, air temperature is equal to mean radiation temperature, no temperature gradient and air flow, in the case of the same amount of clothing and metabolic intensity, if a part of body in a non-uniform environment is equal to its heat dissipation in uniform environment, the air temperature in uniform environment is called EHT in a non-uniform environment.

4.3. Thermal comfort research methods

Currently, there are three main models of thermal comfort. One is experimental research, the second is theoretical analysis, and the third is numerical simulation methods. This section will elaborate on the above three aspects.

(1) Experimental research

Experimental research is guided by scientific principles, establishing an experimental platform that matches research topic, and finally obtaining experimental results by changing the set parameters [79]. Experimental methods can often test the comfort of human body in a real environment or a specific space in a thermal environment, and offer a factual basis for theoretical research. Experimental methods include the climate simulation room experimental method and the field test record analysis method, both of which require a statistical analysis of the subjective thermal comfort of the person being tested. Although the experimental method is convincing, it often requires repeated experiments many times, and generally has high requirements for experimental conditions. And when measuring experimental data, there will be experimental errors. If the measurement results are affected by human factors, such as when measuring the surface temperature of human skin with a thermocouple, the thermocouple is not well bonded to the skin and affects the measurement results, or the assembly of personalized heating equipment and heat insulation devices does not ensure sufficient airtightness, which will have a certain impact on the temperature measurement value and the time for the human body to achieve thermal comfort.

Since the experiment is a subjective questionnaire survey of local and overall thermal sensation and thermal comfort of experimenter, the survey results will be affected by the gender, psychological factors, cold tolerance and other factors of the experimenter. Therefore, the development of a psychological scale on thermal comfort to estimate the reliability and validity of questionnaires will minimize errors.

Currently, there are generally three experimental data collection techniques—invasive, semi-invasive, and non-invasive measurements [80]. Traditionally, invasive measurements are performed directly on the human body with lab equipment. Although the data obtained from invasive measurements is fairly accurate, current predictive models based on invasive measurements generally perform well. For example, Kong et al. [81] provide a new method for assessing personal thermal comfort. This method computes inspection index to infer subtle changes in blood flow on facial skin.

In recent years, experimental research methods have mainly studied thermal comfort of vehicles during actual driving through measurement and electroencephalogram (EEG), skin temperature, heart rate variability.

Electroencephalogram (EEG) is a physiological and neuroscientific method that quickly reflects electrophysiological activity throughout cortex and scalp surface [82]. EEG can record brain's central nervous system [83]. EEG can be applied to judge various neurological disorders [84]. EEG signal is weak [85]. Related studies are experiments in which electroencephalograms (EEGs) are collected by placing specialized electrodes. EEG data is used to develop models that classify thermal comfort state of subjects. Wang [86] studied the effect of vehicle temperature on cognitive ability and EEG on the basis of evaluating EEG characteristics. Results illustrated that cognitive ability of driver decreased with increase of temperature.

Park et al. [87] proposed a method to predict individual thermal status by measuring different human body indexes. Liu et al. [88] proposed a method that could identify 12 human poses to predict thermal discomfort. Luo et al. [89] presented a thermal image-based means to evaluate thermal comfort by measuring facial skin temperature. Qavidel et al. [90] used wearable sensor to obtain skin temperature data. Čulić et al. [91] studied differences between heat map pairs and introduced a personal thermal comfort prediction method. Mehnatkesh et al. [92] proposed a personal thermosensory index by measuring physiological parameters. Bode [93] proposes a new electric vehicle seat heating strategy based on the heat sensitivity of human skin. A new method using deep neural networks to extract gray information of face thermal images and predict individual thermal comfort states. A deep learning-based ResNet34embedded spatial attention mechanism is established for extracting features from facial thermal images. **Figure 9** shows a preliminary frame design for predicting personal thermal comfort [94].

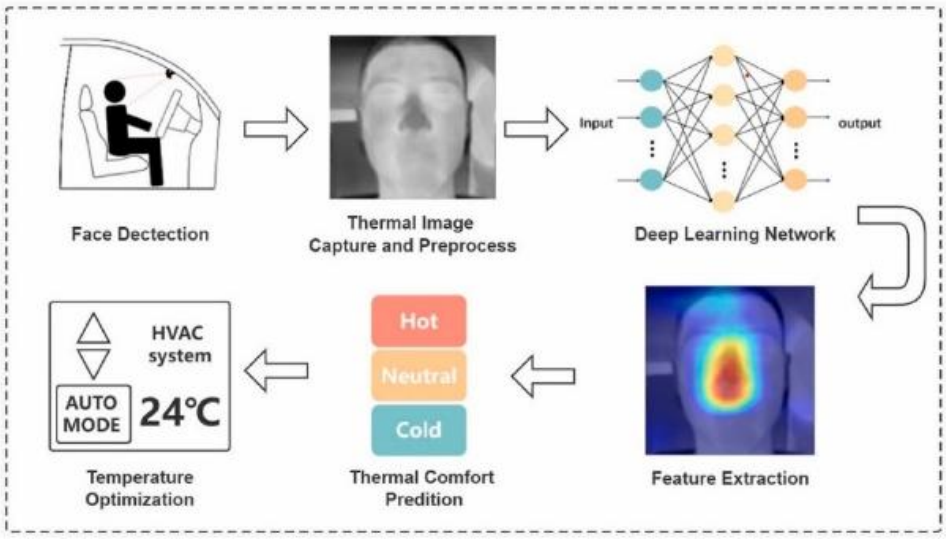

Figure 9. Preliminary framework for thermal comfort prediction and temperature optimization.

Zhang et al. [95] used six models to predict the driver's facial temperature of a specific series of vehicles, namely support vector regression (SVR), artificial neural network (ANN), and gated recurrent unit (GRU). The results of MAE show that when tested using both trained and untrained test datasets, the performance of ANN is the best among the 6 models. In addition, the accuracy of these models is lower when test data sets are collected under new operating conditions. Based on the above results, ANN may be the preferred method for predicting facial air temperature for vehicle drivers. **Figure 10** shows the flowchart for optimizing and evaluating the SVR, ANN, GRU models.

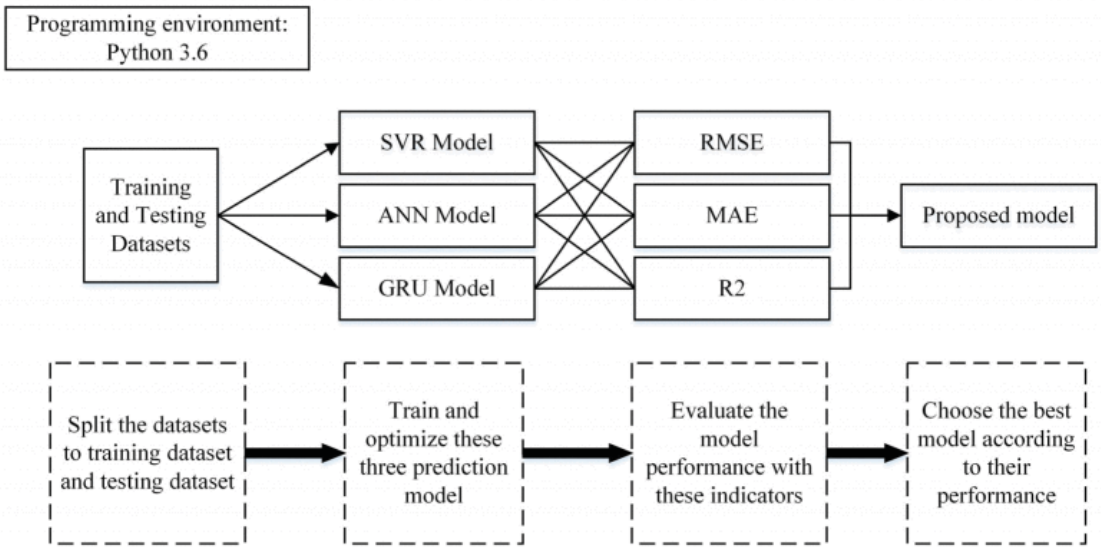

Figure 10. Flow chart for optimizing and evaluating SVR, ANN, GRU models.

(2) Theoretical analysis

Theoretical analysis is to establish a mathematical model related to practical problems, use relevant theories to analyze and study the problem, summarize the law, this method not only requires the established mathematical model to be very accurate,

but also requires the theoretical knowledge of researchers to be very deep, so that the results obtained have reference value. There are 4 commonly used thermal sensing models, including the Predictive Average Voting (PMV) model, the Dynamic Thermal Sensing (DTS) model, the UCB model developed by the University of California, Berkeley, and the Outdoor Thermal Comfort (Lai's) model. At present, there are 3 kinds of virtual cockpit models, virtual mannequins and dummy models. The details are as follows:

1) Virtual cockpit model

The human microenvironment is highly influenced by convection and radiant heat transfer between the body surface and the surrounding environment, and correct turbulence modeling is one of the keys to obtaining repeatable and reliable results [96]. Due to the limitation of computer level, it is difficult to solve the complex turbulence problems encountered in engineering by direct numerical simulation (DNS) of turbulence from the N-S equation, and in this case, the N-S equation (RANS) method for solving the Reynolds mean has become a more effective and feasible means to solve engineering problems. For cockpit modeling, K-ε models and K-ε models with low Reynolds numbers are commonly used. But the drawback of the RANS model is that sometimes the accuracy is insufficient. Compared to the RANS model, large eddy simulation (LES) provides more dynamic details of heat and mass transfer, but relies on computational resources that make this method still unsuitable for human-scale research. Some researchers also use the Separation Vortex Simulation (DES) method. Comparative studies of DES, LES and RANS models show that DES has the potential to be an accurate turbulence model. However, this method needs further research before it can be widely used to simulate the indoor environment of automobiles [97].

2) Virtual mannequin

The establishment of virtual mannequins is the key to thermal comfort simulation research. The virtual mannequin started with an early simplified 2D model and gradually transitioned to a 3D model that was closer to the real world. Shape-based virtual mannequins do not have the same thermoregulation function as the human body can respond to the microenvironment, so researchers have developed more complex thermophysiological models of the human body [98]. The human thermophysiological model is a mathematical representation of the human body and includes: 1) passive systems, which simulate the physical and dynamic heat transfer of the human body and its surroundings (through heat equilibrium equations or biothermal equations); 2) Active system, simulating the physiological regulatory response of the human body to vasoconstriction, vasodilation, and trembling to maintain the stability of core temperature. The human thermos-physiological model can not only represent the heat exchange parameters between the human body and the environment, but also extract some thermal comfort indices such as equivalent temperatures. Thermophy-siological models can be further divided into single-node models, two-node models, and multi-node models according to complexity. Both the single-node model and the two-node model are limited to a unified environment, while the multi-node model considers the composition structure and thermophysiological characteristics of the human body, simulating the heat transfer process inside and on the surface of the human body. The

more complex the model, the more suitable it is to simulate thermal response of the human body in complex environments.

Toader et al. [99] present the details of a recently designed and created thermal model consisting of 79 surface areas with independent neurofuzzy thermoregulation. The components of the model and the acceptance strategy are described. A flexible heating element is used to control the temperature, on which five digital sensors are located. To determine the relationship between heat loss and ambient temperature, thermal model was calibrated in a climate chamber. Thermal models are able to predict local sensations through the so-called equivalent temperature concept of predicting average voting.

3) Dummy models

Human trials are demanding due to high costs and ethical limitations, and differences within and within subjects are often difficult to explain. In comfort studies, a large number of participants are needed to achieve sufficient statistical significance. To reduce this burden, dummies have been used to conduct standardized studies of human thermal comfort [100]. Use of thermal mannequins compared to actual human experimental subjects and tests different scenarios were discussed [101]. The results show that dummy models can provide accurate invasive measurements of human thermal sensory predictions, including questionnaires, monitoring of environmental parameters and human physiological parameters, which have been widely used and integrated with technologies such as IoT, artificial intelligence, and machine learning. At present, there are some new sensors, such as glasses, watches, etc., these wearable devices avoid potential foreign body sensation to a certain extent, but still have a certain degree of invasiveness. Studies have begun to attempt to use infrared thermography to achieve non-contact measurement [102]. Thermal imaging measurement of infrared thermal imaging cameras is a non-contact and relatively cutting-edge imaging method, using infrared thermal imaging detectors to measure the temperature of interior surface of cockpit, the surface of clothing and visible body parts of human body in real time. This experimental method overcomes the shortcomings of traditional single-point temperature measurement technology and visual observation methods, and this new measurement method is expected to gain large-area applications in the future automobile cockpit.

Evaluation results show that none of models can correctly predict thermal sensation in driving condition in the car, because they do not take into account influence of changing solar radiation on thermal sensation. A study of existing international standards that can be used for thermal comfort methods in automotive interiors shows that there are currently no international standards that can accurately assess thermal comfort specific to a vehicle’s ambient space.

(3) Numerical simulation

Numerical simulation is to combine the concepts related to finite elements, simulate and calculate the finite element model through electronic computers, and study the problems encountered [103]. The characteristics of the flow field in the cockpit are studied by computational fluid dynamics CFD (CFD) technology, which can analyze air flow, temperature distribution and air velocity in cockpit, and obtain their distribution patterns. Most of the modeling analysis studies focus on how to generate thermal comfort and mechanism of thermal comfort, and at the same time

carry out the prediction and analysis of thermal comfort under different working conditions [104]. Numerical simulation provides an effective basis for engineers to study cockpit thermal comfort, and can also reduce number of experiments, thereby improving efficiency of practical problem research.

Zhou et al. [105] of Donghua University studied the numerical simulation of cockpit thermal comfort, compared the influence of the setting of the second and third boundary conditions on the human surface temperature distribution in the numerical simulation, analyzed the speed field, temperature field and PMV index evaluation of cockpit, and found that different boundary conditions had a certain impact on simulation results of the cockpit, and selection of appropriate boundary conditions in the process of cockpit thermal comfort research had an important impact on the simulation results [106]. Li et al. [107] established a model that integrates human body thermal regulation mechanism and dynamic environmental features. Kim and Jung [108] validated influence of steering wheel heating system on enhancing hand heat.

Croitoru et al. [109] evaluated effect of turbulence intensity at inlet of the air distribution system on local airflow sensation and thermal discomfort under different ventilation conditions. Jamin et al. [110,111] proposed a complex experimental and numerical study to better understand air distribution in carriage.

5. Conclusion and outlook

The first chapter of this paper introduces research background on thermal comfort in the interior of the car. The second chapter discusses thermal environment in the interior, the influencing factors of thermal comfort in the interior, the evaluation index of thermal comfort, and research methods of thermal comfort.

At the same time, it is also pointed out that the current research on thermal comfort of the interior wall facing the human body is insufficient. At the same time, the wall temperature is not closely related to the temperature field in the space, and the optical characteristics of automobile window glass have insufficient influence on thermal comfort of automobile personnel. Regarding the experimental data, since the experiment uses a subjective questionnaire, it is bound to be due to differences in age, gender, cold tolerance, etc. At present, there is no psychological scale on thermal comfort to support the reliability and validity of the questionnaire. This is also one of the problems that currently exists.

Thirdly, for the automotive field, thermal comfort of the cab in a non-uniform, high-transient environment is still far from fully understood, and there is no universally accepted theory. There is no established industry specification, including test methods, evaluation indicators, etc., and there is currently no international standard that can accurately assess thermal comfort specific to the vehicle's environmental space. The current state of the art is methodologically inconsistent.

Lastly, from aspect of energy saving in car air conditioning, future development prospects of electric vehicles will be very good. To improve energy economy of electric vehicles and reduce the attenuation of low-temperature heating performance, three heat pump air conditioning system solutions for low temperature environments are proposed and analyzed:

(1) Waste heat recovery: Waste heat from batteries, motors and electronic control systems is recycled, and the energy consumption of whole vehicle is optimized while improving performance of heat pump air conditioning system.

(2) Steam jet heat pump air conditioning system: steam jet heat pump air conditioning system of R1234yf refrigerant was tested and studied. Results show that heating COP of heat pump system with steam injection is about 10%–30% higher than that of the heat pump system without steam injection, and the lower the ambient temperature, the more obvious the improvement of heating COP.

(3) CO_2 refrigerant heat pump air conditioning system: Studies have shown that due to the characteristics of CO_2 refrigerant, heat pump system can heat stably and effectively at ambient temperature −20 °C. It is concluded that the current use of steam jet heat pump air conditioning system is an effective means to solve the low-temperature heating of new energy electric vehicles, and in the future, the use of natural refrigerant CO_2 is an inevitable trend. For electric vehicles, targeting specific small body areas with high temperature sensitivity and direct contact heating solutions (resistance heating) can improve thermal comfort and reduce energy consumption at the same time. Therefore, research of new electric vehicle seat heating strategies and development and use of thermal sensitivity test devices are one of the future development trends.

Conflict of interest: The authors declare no conflict of interest.

References

1. Liu B, Zhang Q, Liu J, et al. The impacts of critical metal shortage on China's electric vehicle industry development and countermeasure policies. Energy. 2022; 248: 123646. doi: 10.1016/j.energy.2022.123646
2. Sunagawa M, Shikii S, Beck A, et al. Analysis of the effect of thermal comfort on driver drowsiness progress with Predicted Mean Vote: An experiment using real highway driving conditions. Transportation Research Part F: Traffic Psychology and Behaviour. 2023; 94: 517-527. doi: 10.1016/j.trf.2023.03.009
3. Shin M, Shin Y, Kim Y, et al. Investigation of drivers' thermal comfort based on selective cooling seats with air conditioner in summer using biosignals and subjective survey. Building and Environment. 2024; 250: 111199. doi: 10.1016/j.buildenv.2024.111199
4. Su CQ, Wang ZZ, Liu X, et al. Research on thermal comfort of commercial vehicle and economy of localized air conditioning system with thermoelectric coolers. Energy Reports. 2022; 8: 795-803. doi: 10.1016/j.egyr.2022.10.153
5. He X, Zhang X, Zhang R, et al. More intelligent and efficient thermal environment management: A hybrid model for occupant-centric thermal comfort monitoring in vehicle cabins. Building and Environment. 2023; 228: 109866. doi: 10.1016/j.buildenv.2022.109866
6. Kim Y, Lee M, Shin Y, et al. Investigation of changes in Driver's biosignals and thermal comfort according to the heating method in winter. Case Studies in Thermal Engineering. 2023; 42: 102749. doi: 10.1016/j.csite.2023.102749
7. Su C, Iang Y, Wang Y, et al. Analysis of cockpit thermal comfort and air conditioning economy. Mechanical Design and Manufacturing; 2022.
8. Gagge AP, Stolwjk JAJ, Nishi Y. An effective temperature scale based on a simple model of human physiological regulatory response. ASHRAE Trans; 1971.
9. Huang W, Hu G. Simulation analysis of airflow organization of vehicle room based on different working conditions. Computer Simulation; 2018.
10. Chen B, Lian Y, Xu L, et al. State-of-the-art thermal comfort models for car cabin Environment. Building and Environment. 2024; 262: 111825. doi: 10.1016/j.buildenv.2024.111825
11. Xue C, Li Y, Zhang T. Research on cockpit thermal comfort based on PMV index. Refrigeration and Air Conditioning (Sichuan); 2020.

12. Marcos D, Pino FJ, Bordons C, et al. The development and validation of a thermal model for the cabin of a vehicle. Applied Thermal Engineering. 2014; 66(1-2): 646-656. doi: 10.1016/j.applthermaleng.2014.02.054
13. Alahmer A, Mayyas A, Mayyas AA, et al. Vehicular thermal comfort models; a comprehensive review. Applied Thermal Engineering. 2011; 31(6-7): 995-1002. doi: 10.1016/j.applthermaleng.2010.12.004
14. Khayyam H, Kouzani AZ, Hu EJ, et al. Coordinated energy management of vehicle air conditioning system. Applied Thermal Engineering. 2011; 31(5): 750-764. doi: 10.1016/j.applthermaleng.2010.10.022
15. Alahmer A, Omar M, Mayyas AR, et al. Analysis of vehicular cabins' thermal sensation and comfort state, under relative humidity and temperature control, using Berkeley and Fanger models. Building and Environment. 2012; 48: 146-163. doi: 10.1016/j.buildenv.2011.08.013
16. Schminder J, Gårdhagen R. A generic simulation model for prediction of thermal conditions and human performance in cockpits. Building and Environment. 2018; 143: 120-129. doi: 10.1016/j.buildenv.2018.06.055
17. Fujita A, Kanemaru J, Nakagawa H, et al. Numerical simulation method to predict the thermal environment inside a car cabin. JSAE Review; 2001.
18. Chien CH, Jang JY, Chen YH, et al. 3-D numerical and experimental analysis for airflow within a passenger compartment. International Journal of Automotive Technology. 2008; 9(4): 437-445. doi: 10.1007/s12239-008-0053-2
19. Zhang H, Dai L, Xu G, et al. Studies of air-flow and temperature fields inside a passenger compartment for improving thermal comfort and saving energy. Part I: Test/numerical model and validation. Applied Thermal Engineering. 2009; 29(10): 2022-2027. doi: 10.1016/j.applthermaleng.2008.10.005
20. Che Y. Numerical analysis of air flow field and temperature field in car interior. Dalian: Dalian University of Technology; 2010.
21. Lu K, Gu Z, Jia X, et al. Analysis and improvement of the influence of air conditioning system on thermal comfort of passenger compartment of a heavy goods vehicle. Automotive Engineering; 2011.
22. Kilic M, Kaynakli O. An experimental investigation on interior thermal conditions and human body temperatures during cooling period in automobile. Heat and Mass Transfer. 2010; 47(4): 407-418. doi: 10.1007/s00231-010-0737-9
23. Alahmer A, Abdelhamid M, Omar M. Design for thermal sensation and comfort states in vehicles cabins. Applied Thermal Engineering. 2012; 36: 126-140. doi: 10.1016/j.applthermaleng.2011.11.056
24. Oh MS, Ahn JH, Kim DW, et al. Thermal comfort and energy saving in a vehicle compartment using a localized air-conditioning system. Applied Energy. 2014; 133: 14-21. doi: 10.1016/j.apenergy.2014.07.089
25. Lai C, Wen K, Man C. Effect of airflow uniformity on cooling performance of automobile air conditioning outlet. Machine Tool and Hydraulic Pressure; 2014.
26. Zhang B, Xue T, Hu Z. Analysis and improvement of thermal comfort in the passenger compartment of a car based on PMV/PPD and air age. Automotive Engineering; 2015.
27. Moon JH, Lee JW, Jeong CH, et al. Thermal comfort analysis in a passenger compartment considering the solar radiation effect. International Journal of Thermal Sciences. 2016; 107: 77-88. doi: 10.1016/j.ijthermalsci.2016.03.013
28. Wang J, Zhang X, Jie DX. Experimental study on natural exposure of automobile products in typical dry heat environment in China. Environmental Technology; 2017.
29. Danca P, Bode F, Nastase I, et al. On the Possibility of CFD Modeling of the Indoor Environment in a Vehicle. Energy Procedia. 2017; 112: 656-663. doi: 10.1016/j.egypro.2017.03.1133
30. Giri A, Tripathi B, Thakur HC. 2-D CFD analysis of passenger compartment for thermal comfort and ventilation. International Journal of Engineering Manufacture Science. 2017.
31. He Z, Chen C, Yang G, et al. Modelling of the predicted thermal comfort of the metro passengers under different crowd densities. International Journal of Environmental Engineering. 2019; 10(1): 70. doi: 10.1504/ijee.2019.100019
32. Suhaimi MFB, Kim WG, Cho CW, Lee H. Impact of solar radiation on human comfort in a vehicle cabin: An analysis of body segment mean radiant temperature, Building and Environment, 2023; 245:110849. doi: 10.1016/j.buildenv.2023.110849
33. Lü H, Chen B, Gao T, et al. Analysis of thermal comfort of car cockpit based on flow field and temperature field. Automotive Engineering; 2020.
34. Zhong R, Wang Q, Shi X, et al. Free vibration and random dynamic analyses for the composite cabin-like combined structure in aero-thermal environment. Engineering Analysis with Boundary Elements. 2023; 150: 435-456. doi: 10.1016/j.enganabound.2023.02.014

35. Riaz M, Mahmood MH, Ashraf MN, et al. Experiments and CFD simulation of an air-conditioned tractor cabin for thermal comfort of tractor operators in Pakistan. Heliyon. 2023; 9(12): e23038. doi: 10.1016/j.heliyon.2023.e23038
36. Hadi JM, Alturaihi MH, Jasim NY, et al. Numerical study of airflow and temperature variations inside car at different solar intensity angles. Materials Today: Proceedings. 2022; 60: 1689-1695. doi: 10.1016/j.matpr.2021.12.225
37. Wang T, Zhao K, Lu Y, et al. The airflow characteristics and thermal comfort evaluation in high-speed train cabin with mixing ventilation: An experimental and numerical study. Building and Environment. 2024; 250: 111187. doi: 10.1016/j.buildenv.2024.111187
38. Zhou X, Lai D, Chen Q. Experimental investigation of thermal comfort in a passenger car under driving conditions. Building and Environment. 2019; 149: 109-119. doi: 10.1016/j.buildenv.2018.12.022
39. Yi Z, lv Y, Xu D, et al. Energy saving analysis of a transparent radiative cooling film for buildings with roof glazing. Energy and Built Environment. 2021; 2(2): 214-222. doi: 10.1016/j.enbenv.2020.07.003
40. Chaiyapinunt S, Khamporn N. Effect of solar radiation on human thermal comfort in a tropical climate. Indoor and Built Environment. 2020; 30(3): 391-410. doi: 10.1177/1420326x19891761
41. Setiyo M, Waluyo B, Widodo N, et al. Cooling effect and heat index (HI) assessment on car cabin cooler powered by solar panel in parked car. Case Studies in Thermal Engineering. 2021; 28: 101386. doi: 10.1016/j.csite.2021.101386
42. Wei N, Zheng M. Influence of Environmental Factors and Vehicle Factors on VOC Volatilization Characteristics in Automobiles. Chemical. Engineering Transactions; 2018.
43. Xu B, Chen X, Xiong J. Air quality inside motor vehicles' cabins: A review. Indoor and Built Environment. 2016; 27(4): 452-465. doi: 10.1177/1420326x16679217
44. Levinson R, Pan H, Ban-Weiss G, et al. Potential benefits of solar reflective car shells: Cooler cabins, fuel savings and emission reductions. Applied Energy. 2011; 88(12): 4343-4357. doi: 10.1016/j.apenergy.2011.05.006
45. Bhavsar SC, Solanki PDC, Bhatt, PSM, et al. Analysis of Temperature Variations in an Automobile Cabin Parked Under Sunlight. International Journal of Science and Research Development. 2016.
46. Yang L, Gao S, Zhao S, et al. Thermal comfort and physiological responses with standing and treadmill workstations in summer. Building and Environment. 2020; 185: 107238. doi: 10.1016/j.buildenv.2020.107238
47. Zhang H, Yang X, Zheng W, et al. The CPMV* for assessing indoor thermal comfort and thermal acceptability under global solar radiation in transparent envelope buildings. Energy and Buildings. 2020; 225: 110306. doi: 10.1016/j.enbuild.2020.110306
48. Huang L, Zhai Z. Critical review and quantitative evaluation of indoor thermal comfort indices and models incorporating solar radiation effects. Energy and Buildings. 2020; 224: 110204. doi: 10.1016/j.enbuild.2020.110204
49. Yang Z, Xu X, Zhao L, et al. Analysis of cockpit driver position microenvironment and human thermal comfort. Journal of Tongji University (Natural Science Edition). 2020.
50. Hirn T, Kirmas A, Backes D, et al. The influence of radiation intensity and wavelength on thermal perception. Building and Environment. 2021; 196: 107763. doi: 10.1016/j.buildenv.2021.107763
51. Kong S, Zhang X, Chen J. Effect of front windshield characteristics on thermal comfort in vehicle under solar radiation. Building Thermal Energy Ventilation and Air Conditioning; 2020.
52. Zhang Q, Ding L, Xu R, et al. Human thermoregulatory model for simulating thermal response in high-temperature and hypobaric environments. Case Studies in Thermal Engineering; 52:103682.
53. He M, Liu H, Fang Z, et al. High-temperature and thermal radiation affecting human thermal comfort and physiological responses: An experimental study. Journal of Building Engineering. 2024; 86: 108815. doi: 10.1016/j.jobe.2024.108815
54. Haghighat F. Air infiltration and indoor air quality models—a review. International Journal of Ambient Energy. 1989; 10(3): 115-122. doi: 10.1080/01430750.1989.9675130
55. Zhang L, Qi L, Liu J, et al. Experimental study on dynamic thermal environment of passenger compartment based on thermal evaluation indexes. Science Progress. 2020; 103(3). doi: 10.1177/0036850420942991
56. Mo Z, Tang J, Gu Z, et al. A Study on Numerical Simulation of Cabin Thermal Comfort Based on Visual PMV-PPD Index. Computer Simulation; 2016.
57. Mishra SS, Gaba VK, Netam N. Effect of air velocity and relative humidity on passengers' thermal comfort in naturally ventilated railway coach in hot-dry indian climate. Building and Environment. 2024; 254: 111421. doi: 10.1016/j.buildenv.2024.111421
58. Zhang W. Research on Windshield Glazing Property Effect on Vehicle Cabin Temperature under Solar Radiation. Journal of

Mechanical Engineering. 2011; 47(22): 119. doi: 10.3901/jme.2011.22.119
59. Cheng Y, Niu J, Gao N. Thermal comfort models: A review and numerical investigation. Building and Environment. 2012; 47: 13-22. doi: 10.1016/j.buildenv.2011.05.011
60. Kobayashi Y, Tanabe S ichi. Development of JOS-2 human thermoregulation model with detailed vascular system. Building and Environment. 2013; 66: 1-10. doi: 10.1016/j.buildenv.2013.04.013
61. Takahashi Y, Nomoto A, Yoda S, et al. Thermoregulation model JOS-3 with new open source code. Energy and Buildings. 2021; 231: 110575. doi: 10.1016/j.enbuild.2020.110575
62. D'Ambrosio Alfano FR, Palella BI, Riccio G. THERMODE 2023: Formulation and Validation of a new Thermo-physiological Model for Moderate Environments. Building and Environment. 2024; 252: 111272. doi: 10.1016/j.buildenv.2024.111272
63. Huizenga C, Zhang H, Arens E. A model of human physiology and comfort for assessing complex thermal environments. Building and Environment; 2001.
64. Zhang S, He W, Chen D, et al. Thermal comfort analysis based on PMV/PPD in cabins of manned submersibles. Building and Environment. 2019; 148: 668-676. doi: 10.1016/j.buildenv.2018.10.033
65. Feng C, Ma F, Wang R, et al. A thermal comfort evaluation on vehicular environments based on local human body thermal sensations. Results in Engineering; 2017.
66. Griefahn B, Kü Nemund C. The effects of gender, age, and fatigue on susceptibility to draftdiscomfort. Journal of Thermal Biology. 2001.
67. Fabbri K. Thermal comfort evaluation in kindergarten: PMV and PPD measurement through datalogger and questionnaire. Building and Environment. 2013; 68: 202-214. doi: 10.1016/j.buildenv.2013.07.002
68. Li B, Yao R, Wang Q, et al. An introduction to the Chinese Evaluation Standard for the indoor thermal environment. Energy and Buildings. 2014; 82: 27-36. doi: 10.1016/j.enbuild.2014.06.032
69. Li Y, Liu H, Liu T, et al. Analysis and comparison of general indoor environment thermal comfort evaluation standards at home and abroad. Refrigeration and Air Conditioning; 2017.
70. Silva AS, Ghisi E, Lamberts R. Performance evaluation of long-term thermal comfort indices in building simulation according to ASHRAE Standard 55. Building and Environment. 2016; 102: 95-115. doi: 10.1016/j.buildenv.2016.03.004
71. Wei S, Li M, Lin W, et al. Parametric studies and evaluations of indoor thermal environment in wet season using a field survey and PMV–PPD method. Energy and Buildings. 2010; 42(6): 799-806. doi: 10.1016/j.enbuild.2009.11.017
72. Zhou X, Lai D, Chen Q. Thermal sensation model for driver in a passenger car with changing solar radiation. Building and Environment. 2020; 183: 107219. doi: 10.1016/j.buildenv.2020.107219
73. Zhang Y, Huang J, He L, et al. A study of a thermal management system for passenger compartment comfort and battery heating in hybrid vehicles considering drive mode switching. Thermal Science and Engineering Progress, 2024, 53:102735.
74. Wang M, Wang Y, Geng M, et al. Effect of cold storage backfill on thermal comfort of mine stope based on standard effective temperature. Energy and Buildings. 2023; 300: 113632. doi: 10.1016/j.enbuild.2023.113632
75. Han J, Zhang G, Zhang Q, et al. Field study on occupants' thermal comfort and residential thermal environment in a hot-humid climate of China. Building and Environment. 2007; 42(12): 4043-4050. doi: 10.1016/j.buildenv.2006.06.028
76. Crawshaw LI, Nadel ER, Stolwijk JAJ, et al. Effect of local cooling on sweating rate and cold sensation. Pflügers Archiv. 1975; 354(1): 19-27. doi: 10.1007/bf00584500
77. Liu Q, Li N, He Y, et al. Quantifying the effects of indoor non-uniform solar radiation on human thermal comfort and work performance in warm season. Energy and Buildings. 2024; 306: 113962. doi: 10.1016/j.enbuild.2024.113962
78. Huang L. Effects on Comfort Properties of Knitted Fabric in Hot Environment. Journal of China Textile University. 1998.
79. Dibek B, Ağra Ö. Modelling of human thermal comfort in armored military vehicles: An experimental study of removing heat with spot cooling. Thermal Science and Engineering Progress. 2024; 49: 102493. doi: 10.1016/j.tsep.2024.102493
80. Satheesan L, Kittur PM, Alhussien MN, et al. Reliability of udder infrared thermography as a non-invasive technology for early detection of sub-clinical mastitis in Sahiwal (Bos indicus) cows under semi-intensive production system. Journal of Thermal Biology. 2024; 121: 103838. doi: 10.1016/j.jtherbio.2024.103838
81. Kong M, Dong B, Zhang R, et al. HVAC energy savings, thermal comfort and air quality for occupant-centric control through a side-by-side experimental study. Applied Energy. 2022; 306: 117987. doi: 10.1016/j.apenergy.2021.117987
82. Li J, Wu W, Jin Y, et al. Research on environmental comfort and cognitive performance based on EEG+VR+LEC evaluation method in underground space. Building and Environment. 2021; 198: 107886. doi: 10.1016/j.buildenv.2021.107886

83. Phadikar S, Sinha N, Ghosh R, et al. Automatic Muscle Artifacts Identification and Removal from Single-Channel EEG Using Wavelet Transform with Meta-Heuristically Optimized Non-Local Means Filter. Sensors. 2022; 22(8): 2948. doi: 10.3390/s22082948
84. Dgambaram A, Badruddin N, Asirvadam VS, et al. Online detection and removal of eye blink artifacts from electroencephalogram. Biomed. Signal Process; 2021.
85. Ahmed MdZI, Sinha N, Phadikar S, et al. Automated Feature Extraction on AsMap for Emotion Classification Using EEG. Sensors. 2022; 22(6): 2346. doi: 10.3390/s22062346
86. Wang X, Yang Q, Zhai Y, et al. Effects of Vehicle Air Temperature on Drivers' Cognitive Abilities Based on EEG. Sustainability. 2023; 15(2): 1673. doi: 10.3390/su15021673
87. Park H, Park DY. Prediction of individual thermal comfort based on ensemble transfer learning method using wearable and environmental sensors. Building and Environment. 2022; 207: 108492. doi: 10.1016/j.buildenv.2021.108492
88. Liu R, Dai W, Wu T, et al. AIMIC: Deep Learning for Microscopic Image Classification. Computer Methods and Programs in Biomedicine. 2022; 226: 107162. doi: 10.1016/j.cmpb.2022.107162
89. Luo W, Zhang C, Li Y, et al. Deeply-supervised pseudo learning with small class-imbalanced samples for hyperspectral image classification. International Journal of Applied Earth Observation and Geoinformation. 2022; 112: 102949. doi: 10.1016/j.jag.2022.102949
90. Qavidel Fard Z, Zomorodian ZS, Korsavi SS. Application of machine learning in thermal comfort studies: A review of methods, performance and challenges. Energy and Buildings. 2022; 256: 111771. doi: 10.1016/j.enbuild.2021.111771
91. Čulić A, Nižetić S, Šolić P, et al. Smart monitoring technologies for personal thermal comfort: A review. Journal of Cleaner Production. 2021; 312: 127685. doi: 10.1016/j.jclepro.2021.127685
92. Mehnatkesh H, Jalali SMJ, Khosravi A, et al. An intelligent driven deep residual learning framework for brain tumor classification using MRI images. Expert Systems with Applications. 2023; 213: 119087. doi: 10.1016/j.eswa.2022.119087
93. Bode F, Burnete NV, Fechete Tutunaru L, et al. Improving Electric Vehicle Range and Thermal Comfort through an Innovative Seat Heating System. Sustainability. 2023; 15(6): 5534. doi: 10.3390/su15065534
94. Miao Z, Tu R, Kai Y, et al. A novel method based on thermal image to predict the personal thermal comfort in the vehicle. Case Studies in Thermal Engineering. 2023; 45: 102952. doi: 10.1016/j.csite.2023.102952
95. Zhang X, Wang Y, He X, et al. Prediction of Vehicle Driver's Facial Air Temperature With SVR, ANN, and GRU. IEEE Access. 2022; 10: 20212-20222. doi: 10.1109/access.2022.3149523
96. Li P, Liu X, Wu Y. Analysis of the influence of air supply parameters on occupant's thermal sensation based on FLOEFD. Military Medicine; 2020.
97. Hadžiabdić M, Hafizović M, Ničeno B, et al. A rational hybrid RANS-LES model for CFD predictions of microclimate and environmental quality in real urban structures. Building and Environment. 2022; 217: 109042. doi: 10.1016/j.buildenv.2022.109042
98. Zhou X, Lai D, Chen Q. Evaluation of thermal sensation models for predicting thermal comfort in dynamic outdoor and indoor environments. Energy and Buildings. 2021; 238: 110847. doi: 10.1016/j.enbuild.2021.110847
99. Toader A, Ursu L. Advanced Thermal Manikin for Thermal Comfort Assessment in Vehicles and Buildings. Applied Sciences. 2022; 12(4): 1826. doi: 10.3390/app12041826
100. Zhang Y, Mou L, Yi H. Experimental study on temperature correction of air conditioning dummy. Equipment Environmental Engineering; 2019.
101. Psikuta A, Allegrini J, Koelblen B, et al. Thermal manikins controlled by human thermoregulation models for energy efficiency and thermal comfort research—A review. Renewable and Sustainable Energy Reviews. 2017; 78: 1315-1330. doi: 10.1016/j.rser.2017.04.115
102. Yang B, Li X, Hou Y, et al. Non-invasive (non-contact) measurements of human thermal physiology signals and thermal comfort/discomfort poses -A review. Energy and Buildings. 2020; 224: 110261. doi: 10.1016/j.enbuild.2020.110261
103. Huo W, Cheng Y, Jia Y, et al. Research on the thermal comfort of passenger compartment based on the PMV/PPD. International Journal of Thermal Sciences. 2023; 184: 107876. doi: 10.1016/j.ijthermalsci.2022.107876
104. Brusey J, Hintea D, Gaura E, et al. Reinforcement learning-based thermal comfort control for vehicle cabins. Mechatronics. 2018; 50: 413-421. doi: 10.1016/j.mechatronics.2017.04.010
105. Zhou S, Fu H. Simulation of occupant surface temperature distribution and cockpit thermal comfort. Automotive Engineering; 2018.

106. Russi L, Guidorzi P, Pulvirenti B, et al. Air Quality and Comfort Characterisation within an Electric Vehicle Cabin in Heating and Cooling Operations. Sensors. 2022; 22(2): 543. doi: 10.3390/s22020543
107. Jianong Li, Siqi Zhou, Yichen Yu, et al. Effects of dynamic airflows on convective cooling of human bodies − Advances in thermal comfort assessment and engineering design, Energy and Buildings, 2024, 324:114924.
108. Kim GT, Jung JY. Effect of steering wheel heating system on hand thermal sensation. Journal of Mechanical Science and Technology. 2022; 36(7): 3717-3725. doi: 10.1007/s12206-022-0645-1
109. Croitoru C, Nastase I, Bode F, et al. Assessment of virtual thermal manikins for thermal comfort numerical studies. Verification and validation. Science and Technology for the Built Environment. 2021; 28(1): 21-41. doi: 10.1080/23744731.2021.1916379
110. Jamin A. Experimental and numerical study of the flow dynamics and thermal behavior inside a car cabin: Innovative air diffusers and human body plumes interactions. Energy Reports. 2022; 8: 992-1002. doi: 10.1016/j.egyr.2022.07.133
111. Huang Y, Wu X, Jing J. Research on the electric vehicle heat pump air conditioning system based on R290 refrigerant. Energy Reports. 2022; 8: 447-455. doi: 10.1016/j.egyr.2022.05.112

Mechanical Engineering Advances 2025, 3(1), 1950.
https://doi.org/10.59400/mea1950

Perspective

Parametric optimization and determination in machining processes by means of probabilistic multi-objective optimization

Maosheng Zheng[1,*], Jie Yu[2]

[1] School of Chem. Eng., Northwest University, Xi'an 710069, China
[2] College of Life Sci., Northwest University, Xi'an 710069, China
*** Corresponding author:** Maosheng Zheng, mszhengok@aliyun.com

CITATION

Zhang M, Yu J. Parametric optimization and determination in machining processes by means of probabilistic multi-objective optimization. Mechanical Engineering Advances. 2025; 3(1): 1950. https://doi.org/10.59400/mea1950

ARTICLE INFO

Received: 28 October 2024
Accepted: 25 November 2024
Available online: 28 November 2024

Abstract: In the present article, it attempts to present the determination of optimal parameters of machining processes by means of probabilistic multi-objective optimization (PMOO), in which the optimal objectives (attributes) are fundamentally divided into beneficial type and unbeneficial type, moreover all attributes of both beneficial type and unbeneficial type are evaluated separately with equivalent manner to get their partial preferable probability. Finally, the total preferable probability of each alternative is obtained by the product of all partial preferable probabilities, which is the unique and decisive representative of the alternative to join the competitive optimization, the optimum alternative is with the highest total preferable probability. An example of parametric optimization and determination of aerospace component with Electro Chemical Machining (ECM) is taken to illuminate the procedure. In the case of ECM, the current, voltage, and feed rate are as the optimal parameters to be investigated, while Material Removal Rate (MRR), and Surface Roughness (SR) are the optimal objective responses to be measured. The experimental runs were designed using an L_{27} Taguchi orthogonal array. In the assessment of PMOO for ECM, the objective MRR belongs to the beneficial attribute, and the objective SR is as the unbeneficial attribute. The novelty of this work is to reflect the simultaneity and the irreplacement of optimization of objectives MRR and SR in the optimal system. The evaluated results reveal that the optimized experimental scheme is the alternative 8, which is with the optimal responses of MRR of 280.112 g/min and SR of 0.45 μm, the corresponding optimum experimental parameters are voltage of 12 V, electrolyte flow rate of 12 m/s and tool feed rate of 0.4 mm/min, respectively. The achievement of the present article indicates the validity of the corresponding approach and algorithm.

Keywords: optimal parameters; machining processes; probabilistic multi-objective optimization; simultaneity; systems theory

1. Introduction

Parametric optimization and determination in machining processes could improve the productivity of the aerospace industry. In general, the machining performance could be measured in terms of Material Removal Rate (MRR), Surface Roughness (SR) and Tool Wear Rate (TWR) [1]. Producing components with high accuracy increases the performance of the mechanical parts [2].

In order to meet the requirements for aero-components, there appears some significant and essentially Unconventional Machining Process for production technologies, such as Electro Chemical Machining (ECM), Plasma Arc Machining (PAM), Electric Beam Machining (EBM), Electric Discharge Machining (EDM) and Ultra Sonic Machining (USM), which avoids the direct contact of metal to tool [3–5].

Electrochemical machining (ECM) is one of the most appropriate approaches for machining of aero-components since it has distinctive benefits, including negligible tool wear, excellent machining efficiency, autonomy, and low cost in accordance with the exact physical properties of the corresponding material [6,7].

However, the optimization of a machining system with many objective responses simultaneously is still a problem, though some so called "multi criteria decision making methods" were frequently used to deal with the relevant problems [8], such as Grey Rational Analysis (GRA), Technique for Order Performance by Similarity to Ideal Solution (TOPSIS), Vlse Kriterijumska Optimizacija I Kompromisno Resenje (VIKOR), Multi- Objective Optimization on the Basis of Ratio Analysis (MOORA), ELimination and Choice Expressing Reality (ELECTRE), Preference Ranking for Organization Method for Enrichment Evaluation (PROMETHEE), etc. The intrinsic drawback of above methods is the lack of revealing the simultaneity and the irreplacement of many optimal objectives in the system. The fatal shortcoming of these methods is not aware.

Recently, probabilistic multi-objective optimization (PMOO) was proposed [8], which could reveal the simultaneity and the irreplacement of many optimal objective responses in the system properly, in which the optimal objectives (attributes) are basically divided into both beneficial type and unbeneficial type, furthermore all attributes of above two types are evaluated separately with equivalent manner to obtain their partial preferable probability. Finally, the total preferable probability of each alternative is gained by the product of all partial preferable probabilities, which is the unique and decisive representative of the alternative to join the optimization competitively. The optimum alternative with the highest total preferable probability wins the competition at last [8].

In the present article, the parametric optimization and determination of aerospace component with Electro Chemical Machining (ECM) is taken as an example to illuminate the successful utility of probabilistic multi-objective optimization (PMOO) in machining processes.

2. Brief introduction of methodology of probabilistic multi-objective optimization

The probabilistic multi-objective optimization (PMOO) is concisely demonstrated here [8].

Generally, in a multi-objective optimization (MOO) problem some attribute utility indexes are with the characteristics of "the higher the better" [8], i.e., the attribute with higher value is inevitably more welcomed and could get more preference, this type of attribute is called beneficial index. In this case, a term "preferable probability" could be introduced to reflect the "preference degree" of the attribute in the optimization process reasonably [8]. Furthermore, for the simplicity, it assumes that the partial preferable probability of such kind of attribute responses is proportional to the specific value of its attribute utility index positively, i.e.,

$$P_{ij} = A_j U_{ij},\ i = 1, 2, ..., n, j = 1, 2, ..., m. \quad (1)$$

In Equation (1), n is the total number of alternatives in the relevant candidate system; m represents the total number of objective response indicators of each alternative; U_{ij} is the utility value of the j-th objective indicator of the i-th alternative; P_{ij} represents the partial preferable probability of the beneficial attribute index U_{ij}; A_j represents the normalization factor of the j-th beneficial attribute (objective) indicator.

In the light of general principle of probability theory [9], for the j-th material objective response index, it derives following expression for the normalization factor [8],

$$A_j = 1/(n\overline{U_j}) \tag{2}$$

In Equation (2), $\overline{U_j}$ is the average utility value of the j-th attribute index in the attribute group involved.

On the other hand, in a MOO problem some attribute utility indexes are with the characteristics of "the lower the better" [8], i.e., the attribute with lower value is more welcomed and could get more preference, this type of objective responses is called unbeneficial index. In this case, the partial preferable probability of the unbeneficial attribute is assumed to be linearly related to its attribute utility index value negatively in the optimization process equivalently,

$$P_{ij} = B_j(U_{jmax}+U_{jmin}-U_{ij}),\ i = 1, 2, ..., n, j = 1, 2, ..., m. \tag{3}$$

In Equation (3), both U_{jmin} and U_{jmax} represent the minimum and maximum utility values of the attribute indicators in the j-th objective (attribute) group, respectively; B_j is the normalization factor of the j-th unbeneficial attribute index, which can be expressed as [8],

$$B_j = 1/[n(U_{j\max} + U_{j\min}) - n\overline{U_j}] \tag{4}$$

In Equation (4), the symbols $\overline{U_j}$, U_{jmin} and U_{jmax} are with the same meanings as in the previous paragraphs.

Furthermore, according to the fundamentals of probability theory [9], the total preferable probability of the i-th alternative can be written as the product of all partial preferable probabilities,

$$P_i = P_{i1} \cdot P_{i2} \cdot \ldots \cdot P_{ij} \cdot \ldots = \prod_{j=1}^{m} P_{ij}. \tag{5}$$

Obviously, in this assessment, the total preferable probability of each alternative is the unique and decisive index in the optimization process. This is the probabilistic multi-objective optimization (PMOO). Besides, through above procedures with Equations (1)–(5), the multi-objective optimization problem is now transformed into a single-objective optimization one in term of total preferable probability naturally. At last, the optimum alternative corresponds to the specific candidate that is with the highest total preferable probability, which is the optimal result of this overall optimization.

Moreover, if there is a weighting factor w_j for j-th objective response, the total preferable probability of the i-th alternative can be expressed in following form [8],

$$P_i = {P_{i1}}^{w_1} \cdot {P_{i2}}^{w_2} \cdot \ldots \cdot {P_{ij}}^{w_j} \cdot \ldots = \prod_{j=1}^{m} {P_{ij}}^{w_j}. \tag{6}$$

Many applications of above approach are performed [8], which gave acceptable consequences and are consistent with known. This indicates the reasonability of the approach.

In next section, the parametric optimization and determination of aerospace component with Electro Chemical Machining (ECM) is taken as an example to illuminate the utility of probabilistic multi-objective optimization in machining processes.

3. Application example and results

Parametric optimization and determination of aerospace component with Electro Chemical Machining (ECM) is illuminated as an example here [7]. In the case of ECM, the current, voltage, and feed rate are used as the optimal parameters to be investigated, while the Material Removal Rate (MRR), and Surface Roughness (SR) are the optimal objective responses to be measured and assessed. The experimental runs were designed using an L_{27} Taguchi orthogonal array.

In the experiment, 27 trial runs completed [7], which is cited in **Table 1**. In the assessment of PMOO for this issue, the objective MRR is as the beneficial attribute, and the objective SR is as the unbeneficial attribute.

The assessment result of this issue is presented in **Table 2**. In **Table 2**, the columns 4, 5, and 6 give the assessed results of partial preferable probability P_{MRR} for Material Removal Rate (MRR), partial preferable probability P_{SR} for Surface Roughness (SR), and total preferable probability $P_t \times 10^3$ for each alternative, respectively. The column 7 gives the ranking value according to the total preferable probability of each alternative.

From **Table 2**, it can be seen that the experimental scheme 8 is with the highest total preferable probability and at rank 1 position in the assessment by means of probabilistic multi-objective optimization, thus the optimized experimental scheme is alternative 8 with the optimum responses of MRR of 280.112 g/min and SR of 0.45 μm, which is with the optimum experimental parameters of voltage of 12 V, electrolyte flow rate of 12 m/s and tool feed rate of 0.4 mm/min. However, Animesh Kumar Sharma et al got the alternative 3 as their optimized the experimental scheme by means of using VIKOR and TOPSIS [7], the latter is with the responses of MRR of 117.824 g/min and SR of 0.89 μm. Obviously the responses of MRR and SR of alternative 8 are much superior to those of alternative 3.

Table 1. Experimental results of the aerospace component with ECM.

No.	Voltage (V)	Electrolyte flow rate (m/s)	Tool feed rate (mm/min)	MRR (g/min)	SR (μm)
1	12	8	0.2	288.176	1.23
2	12	8	0.4	208.656	0.91
3	12	8	0.6	117.824	0.89
4	12	10	0.2	235.424	0.57
5	12	10	0.4	330.512	1.22
6	12	10	0.6	311.472	1.87
7	12	12	0.2	235.424	1.12

Table 1. (*Continued*).

No.	Voltage (V)	Electrolyte flow rate (m/s)	Tool feed rate (mm/min)	MRR (g/min)	SR (μm)
8	12	12	0.4	280.112	0.45
9	12	12	0.6	140.896	1.46
10	15	8	0.2	344.960	1.21
11	15	8	0.4	205.744	1.32
12	15	8	0.6	328.608	0.78
13	15	10	0.2	160.720	1.93
14	15	10	0.4	228.032	0.81
15	15	10	0.6	114.016	0.90
16	15	12	0.2	205.520	1.36
17	15	12	0.4	219.072	1.72
18	15	12	0.6	177.744	1.78
19	18	8	0.2	202.272	0.85
20	18	8	0.4	339.472	1.97
21	18	8	0.6	271.264	1.58
22	18	10	0.2	308.112	1.49
23	18	10	0.4	302.848	1.18
24	18	10	0.6	314.048	1.27
25	18	12	0.2	268.912	1.48
26	18	12	0.4	132.384	1.61
27	18	12	0.6	134.848	2.01

Table 2. Assessment result of the aerospace component with ECM.

No.	MRR (g/min)	SR (μm)	Partial preferable probability for MRR, P_{MRR}	Partial preferable probability for SR, P_{SR}	Total preferable probability, $P_t \times 10^3$	Rank
1	288.176	1.23	0.0450	0.0391	1.7591	9
2	208.656	0.91	0.0326	0.0493	1.6050	11
3	117.824	0.89	0.0184	0.0499	0.9180	18
4	235.424	0.57	0.0367	0.0601	2.2082	3
5	330.512	1.22	0.0516	0.0394	2.0339	5
6	311.472	1.87	0.0486	0.0188	0.9120	19
7	235.424	1.12	0.0367	0.0426	1.5656	12
8	280.112	0.45	0.0437	0.0639	2.7941	1
9	140.896	1.46	0.0220	0.0318	0.6992	23
10	344.960	1.21	0.0538	0.0397	2.1399	4
11	205.744	1.32	0.0321	0.0362	1.1640	16
12	328.608	0.78	0.0513	0.0534	2.7397	2
13	160.720	1.93	0.0251	0.0169	0.4227	26
14	228.032	0.81	0.0356	0.0525	1.8672	7
15	114.016	0.90	0.0178	0.0496	0.8827	20
16	205.520	1.36	0.0321	0.0350	1.1219	17
17	219.072	1.72	0.0342	0.0235	0.8045	22

Table 2. (*Continued*).

No.	MRR (g/min)	SR (μm)	Partial preferable probability for MRR, P_{MRR}	Partial preferable probability for SR, P_{SR}	Total preferable probability, $P_t \times 10^3$	Rank
18	177.744	1.78	0.0277	0.0216	0.5998	24
19	202.272	0.85	0.0316	0.0512	1.6161	10
20	339.472	1.97	0.0530	0.0156	0.8255	21
21	271.264	1.58	0.0423	0.0280	1.1847	15
22	308.112	1.49	0.0481	0.0308	1.4832	13
23	302.848	1.18	0.0473	0.0407	1.9238	6
24	314.048	1.27	0.0490	0.0378	1.8547	8
25	268.912	1.48	0.0420	0.0312	1.3078	14
26	132.384	1.61	0.0207	0.0270	0.5584	25
27	134.848	2.01	0.0210	0.0143	0.3011	27

4. Conclusion

The probabilistic multi-objective optimization is an effective methodology to deal with the parametric optimization and determination in machining processes. In the PMOO assessment, the optimal objectives (attributes) are basically divided into both beneficial type and unbeneficial type; all objective responses of either beneficial type or unbeneficial type are evaluated separately with equivalent manner simultaneously. The achievement of the present article reflects the validity of the corresponding approach and algorithm for the utilization of multi-objective optimization in machining processes.

Author contributions: Conceptualization, MZ; methodology, MZ; validation, JY; formal analysis, JY; investigation, JY; data curation, JY; writing—original draft preparation, MZ; writing—review and editing, JY. All authors have read and agreed to the published version of the manuscript.

Conflict of interest: The authors declare no conflict of interest.

References

1. Wickramasinghe KC, Sasahara H, Rahim EA, et al. Recent advances on high performance machining of aerospace materials and composites using vegetable oil-based metal working fluids. Journal of Cleaner Production. 2021; 310: 127459. doi: 10.1016/j.jclepro.2021.127459
2. Manikandan N, Balasubramanian K, Palanisamy D, et al. Machinability Analysis and ANFIS modelling on Advanced Machining of Hybrid Metal Matrix Composites for Aerospace Applications. Materials and Manufacturing Processes. 2019; 34(16): 1866-1881. doi: 10.1080/10426914.2019.1689264
3. Zheng J, Zheng W, Chen A, et al. Sustainability of unconventional machining industry considering impact factors and reduction methods of energy consumption: A review and analysis. Science of The Total Environment. 2020; 722: 137897. doi: 10.1016/j.scitotenv.2020.137897
4. Sivakandhan C, Babu Loganathan G, Murali G, et al. Material characterization and unconventional machining on synthesized Niobium metal matrix. Materials Research Express. 2020; 7(1): 015018. doi: 10.1088/2053-1591/ab624d
5. Rajmohan T, Vinayagamoorthy R, Mohan K. Review on effect machining parameters on performance of natural fibre–reinforced composites (NFRCs). Journal of Thermoplastic Composite Materials. 2018; 32(9): 1282-1302. doi: 10.1177/0892705718796541

6. Zhu D, Xu HY. Improvement of electrochemical machining accuracy by using dual pole tool. Journal of Materials Processing Technology. 2002; 129(1-3): 15-18. doi: 10.1016/S0924-0136(02)00567-8
7. Sharma AK, Aravindan N, Ignatia KMJ, et al. Hybrid multi criteria decision making methodology for improving sustainability of the manufacturing sector. International Journal on Interactive Design and Manufacturing (IJIDeM). Published online June 10, 2024. doi: 10.1007/s12008-024-01846-7
8. Zheng M, Teng H, Yu J, et al. Probability-Based Multi-Objective Optimization for Material Selection. Springer Nature Singapore; 2023. doi: 10.1007/978-981-19-3351-6
9. Wang D. Probability Theory and Mathematical Statistics. Beijing Institute of Technology Press, Beijing; 2020.

Academic Publishing Pte. Ltd.

Add: 73 Upper Paya Lebar Road, #07-02B-01, Centro Bianco, Singapore 534818
Tel: +65 83184869
E-mail: editorial_office@acad-pub.com
Web: http://ojs.acad-pub.com/